Romeo Susan-Resiga
Professor
Hydraulic Machinery Department,
"Politehnica" University of Timişoara,
Bvd. Mihai Viteazu 1,
RO-300222, Timişoara, Romania
e-mail: resiga@mh.mec.utt.ro

Gabriel Dan Ciocan
Ecole Polytechnique Fédérale de Lausanne,
Laboratory for Hydraulic Machines,
Av. de Cour 33Bis, CH-1007,
Lausanne, Switzerland
e-mail: GabrielDan.Ciocan@epfl.ch

Ioan Anton
Professor
Member of the Romanian Academy
"Politehnica" University of Timişoara,
Hydraulic Machinery Department,
Bvd. Mihai Viteazu 1,
RO-300222, Timişoara, Romania

François Avellan
Professor
École Polytechnique Fédérale de Lausanne,
Laboratory for Hydraulic Machines,
Av. de Cour 33Bis, CH-1007,
Lausanne, Switzerland
e-mail: francois.avellan@epfl.ch

Analysis of the Swirling Flow Downstream a Francis Turbine Runner

An experimental and theoretical investigation of the flow at the outlet of a Francis turbine runner is carried out in order to elucidate the causes of a sudden drop in the draft tube pressure recovery coefficient at a discharge near the best efficiency operating point. Laser Doppler anemometry velocity measurements were performed for both axial and circumferential velocity components at the runner outlet. A suitable analytical representation of the swirling flow has been developed taking the discharge coefficient as independent variable. It is found that the investigated mean swirling flow can be accurately represented as a superposition of three distinct vortices. An eigenvalue analysis of the linearized equation for steady, axisymmetric, and inviscid swirling flow reveals that the swirl reaches a critical state precisely (within 1.3%) at the discharge where the sudden variation in draft tube pressure recovery is observed. This is very useful for turbine design and optimization, where a suitable runner geometry should avoid such critical swirl configuration within the normal operating range. [DOI: 10.1115/1.2137341]

1 Introduction

Swirling flow behavior in various technical applications has long been an intensive subject of research. Usually swirl effects are seen as either the desired result of design or unavoidable, possibly unforseen, side effects [1]. However, the hydraulic turbine draft tube on one hand benefits from the swirl at the runner outlet in order to mitigate flow detachment in the cone, but on the other hand suffers from the flow instabilities leading to pressure fluctuations and ultimately to the draft tube surge.

The draft tube of a hydraulic turbine is the machine component where the flow exiting the runner is decelerated, thereby converting the excess of kinetic energy into static pressure. In the case of machine rehabilitation of an existing power plant, mostly only the runner and the guide vanes are currently modified. For economical and safety reasons, the spiral casing and the draft tube are seldom redesigned, even if these components present some undesirable behavior. However, the installation of an upgraded runner requires a reliable prediction of the flow in a compact draft tube in order to avoid the peculiar and undesirable efficiency curve from Fig. 1. The efficiency drop as the discharge is increased above the best efficiency point value is found to be related to a corresponding sudden variation in the draft tube pressure recovery coefficient at the same discharge. It is this phenomenon we address in this paper.

The obvious practical importance of predicting the complex flow downstream the turbine runner, in the draft tube, led to the FLINDT research project of Flow Investigation in Draft Tubes [2]. The main objective of this project was to investigate the flow in hydraulic turbines draft tubes, for a better understanding of the

physics of these flows and to build up an extensive experimental data base describing a wide range of operating points which can provide a firm basis for the assessment of the CFD engineering practice in this component. The extensive experimental investigation of the draft tube flow has been complemented with three-dimensional numerical flow simulations [3,4] aimed at elucidating the swirling flow evolution up to the turbine outlet as well as the phenomena that led to the peculiar sudden drop in the turbine efficiency.

Other investigations have been mainly focused on the ability of the CFD tools to accurately reproduce the complex three-dimensional velocity and pressure field in draft tubes for Kaplan turbines [5,6]. One important issue addressed in these studies was the sensitivity of numerical results to the boundary conditions, particularly the inlet ones.

The present paper focuses on the structure of the swirl produced by the constant pitch turbine runner and further ingested by the draft tube. The corresponding hydrodynamic field is a direct outcome of the runner design and the operating point. Since changing the runner design, while keeping the same draft tube, may lead to an unexpected sudden efficiency drop for a certain discharge, it would be preferable that some design criteria be put forward as far as the runner outlet swirl is concerned. The present analysis shapes such criteria by using relative simple mathematical and numerical tools. Of course, the complex three-dimensional and unsteady flow in the draft tube cannot be quantitatively predicted only by analyzing the draft tube inlet swirl. However, if the runner outlet swirl structure displays a sudden change with respect to appropriate criteria, and this change occurs at a discharge close to the experimental one where the sudden drop in turbine efficiency is observed, these criteria should be taken into account when designing or redesigning the runner.

In analyzing a swirling flow one benefits from a large body of literature on this subject. In laboratory investigations swirl was
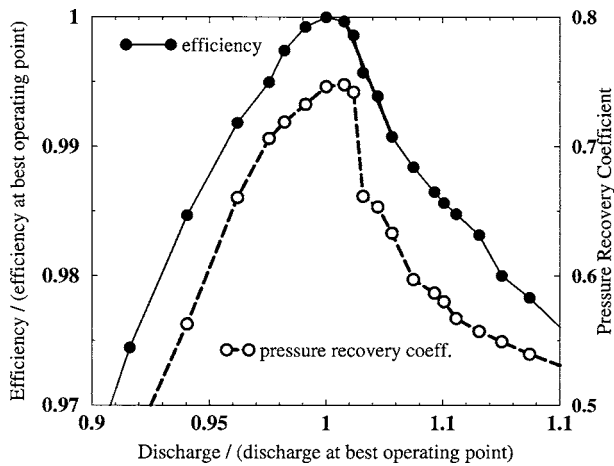

Fig. 1 Efficiency break off obtained by increasing the discharge and keeping the specific energy constant. Model test of a Francis turbine with specific speed 0.56.

Fig. 2 Sketch of the Francis turbine model and LDA setup for the flow survey section at runner outlet-draft tube inlet

generated by adjustable guidevanes, by fixed vanes similar to those employed in combustors, or by tangential inflow through a long slit [1]. The closest setup to the hydraulic turbine case seems to be the adjustable radial guidevane apparatus, which has been largely used for more than 50 years to investigate, both experimentally and numerically, the so-called vortex breakdown (VB) phenomenon [7–10]. The formulas employed in these studies to fit both axial and circumferential velocity component radial variation are of particular relevance for our study.

Several theoretical developments have been devoted to explain the VB. However, a general consensus over the definition of this phenomenon has not been reached yet. For example, Benjamin [11] considers the VB to be a finite transition between two dynamically conjugate states of axisymmetric flow, analogous to the hydraulic jump in open-channel flow. A similar definition was later adopted by Keller [12], who argued that various authors or even schools have conflicting views on the correct interpretation of the physics of VB. Leibovich [13] relates VB to a disturbance characterized by the formation of an internal stagnation point on the vortex axis, followed by reversed flow in a region of limited axial extent. Goldshtik and Hussain [14] consider that VB occurs due to solution nonuniqueness in some range of inflow parameters when the entire steady flow experiences a jump to another metastable steady state with the same boundary conditions. They stress that VB is a loss-free process and, hence, analogies with shocks or hydraulic jumps are misleading and must be abandoned. All theories for confined swirling flows consider axisymmetric geometries with constant or variable cross section (e.g., slowly diverging pipes). It is difficult to imagine that a simplified theory could be elaborated for a swirling flow in an actual draft tube with both cross-section shape and area variation, as well as changes in the flow direction. However, at least for the draft tube cone where most of the pressure recovery occurs, swirling flow theories might provide valuable results for design evaluation and optimization.

Mauri et al. [15,3] developed and applied original techniques to analyze the three-dimensional flow in the FLINDT draft tube. They explain the draft tube efficiency drop from Fig. 1 by a global instability triggered by the flow rate increase. The topological structure of the velocity field changes abruptly with the emergence of a saddle point and a focus in the skin friction lines pattern on the elbow wall, leading to a global Werlé-Legendre separation that blocks the right channel. However, there is an important question to be answered: is this phenomenon the primary cause of the draft tube efficiency drop or it is one of the consequences of a corresponding abrupt change in the swirling flow ingested by the draft tube as the discharge increases? It is this question we address in
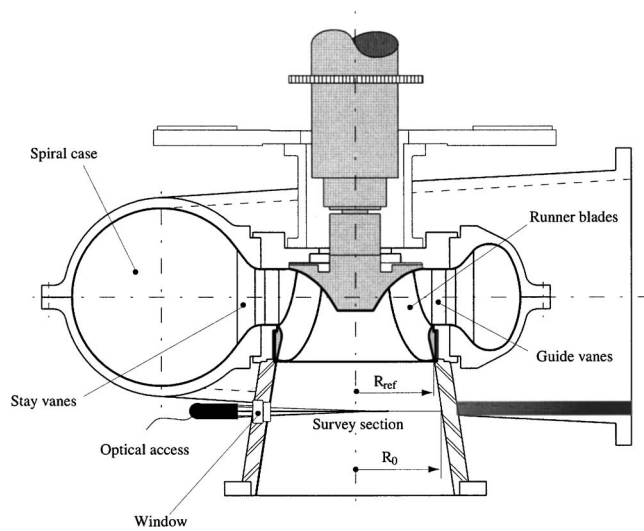
this paper, by investigating the swirling flow on the draft tube inlet section within the general framework of vortex breakdown theories.

In Sec. 2 we briefly present the experimental setup and measuring techniques used to investigate the flow in a Francis turbine draft tube. In this paper we examine the flow on a section at the runner outlet/draft tube inlet. Laser Doppler anemometry has been employed to investigate the velocity components, with particular attention paid to the data error control.

Section 3 is devoted to the analytical representation of velocity components radial variation. A critical analysis of swirling flow models available in literature is followed by the development of a model particularly suited to hydraulic turbines. It is shown that a three-vortex system accurately represents the experimental data, and a least squares technique is employed for computing the model parameters. Finally, the velocity profiles are parametrized only by the discharge coefficient, thus allowing a swirl behavior analysis as the operating point changes continuously.

The nonlinear Long-Squire equation is used in Sec. 4 as a mathematical model for the swirling flow at the draft tube inlet. The finite element method is employed to solve the corresponding boundary value problem for the stream function.

The solution behavior is examined in Sec. 5 using the linearized operator spectrum analysis. It was found that the critical state of the swirl configuration, defined by Benjamin [11], is in good agreement with the abrupt change experimentally observed in the draft tube pressure recovery coefficient.

The paper conclusions are summarized in Sec. 6.

2 Experimental Investigation of the Velocity Field on the Draft Tube Inlet

The FLINDT project [2] experimental investigations were carried out on a Francis turbine scaled model of specific speed 0.56 (Fig. 2). The turbine model has a spiral casing of double curvature type with a stay ring of 10 stay vanes, a distributor made of 20 guide vanes, a 17-blade runner of a 0.4 m outlet diameter, and a symmetric elbow draft tube with one pier. The global measurements for flow rate, head, and efficiency were performed according to the IEC 60193 International Standard [16].

The experimental data used in this paper were obtained with a two-component probe Laser Doppler Anemometer (LDA), using back-scattered light and transmission by optical fiber, with a laser of 5 W argon-ion source. The main characteristics of the optical system are laser wave lengths 488/514.5 nm, probe diameter
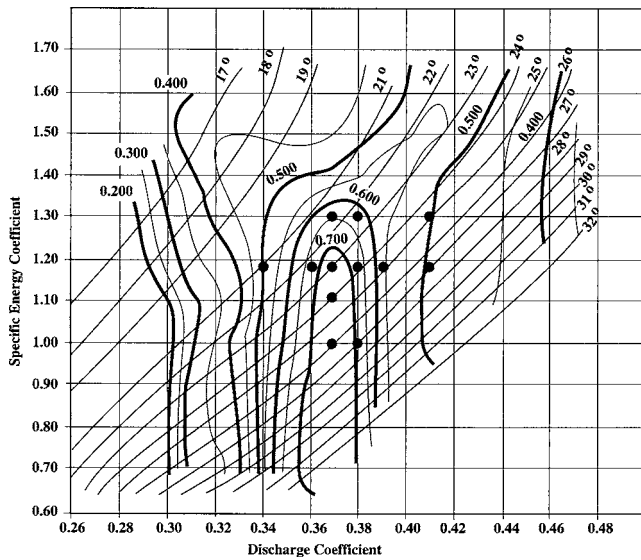
Fig. 3 Pressure recovery isolines (thick lines) for the draft tube investigated in the FLINDT project. The turbine operating points (discharge coefficient-specific energy coefficient) are shown with filled circles.
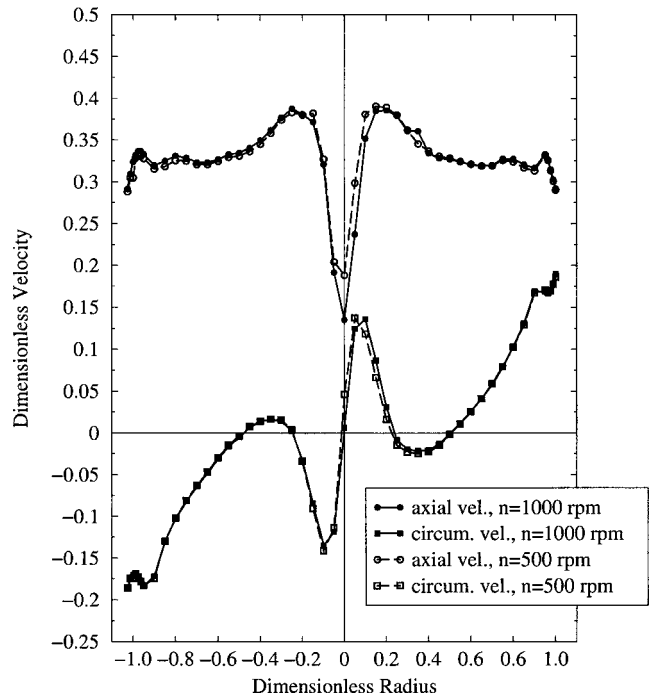

Fig. 4 Reynolds number influence on the dimensionless velocity profiles at operating point with discharge coefficient 0.368 and energy coefficient 1.18

60 mm, beam spacing probe with beam expander 73.3 mm, focal length 1000 mm, fringe spacing ~5.3 nm, and measuring volume $\sigma_x = \sigma_y \sim 0.2$ mm, $\sigma_z \sim 6$ mm.

Spherical silver-coated glass particles are introduced in the test rig flow. These particles are hollowed in order to match the water density and are able to follow flow fluctuations frequency up to 5 kHz [17]. The mean diameter of these particles is 10 μm.

In order to control the position of the measurement volume, a ray tracing technique is used for calculating direct and inverse light paths of laser beams through the different media (air, window, water). An optical window with plane and parallel faces is used as an interface. The measuring point geometrical location is controlled within a 0.05 mm accuracy. Both axial and circumferential components of the velocity are measured. The uncertainties of the velocity measurements are estimated to be 2% of the measured value [18].

The global "efficiency" of the draft tube is quantified using the static pressure recovery coefficient, defined as

$$\chi = \frac{(p/\rho + gz)_{out} - (p/\rho + gz)_{ref}}{Q^2/2A_{ref}^2}. \qquad (1)$$

Figure 3 presents isolines of the pressure recovery coefficient in discharge coefficient-energy coefficient coordinates. The operating points further referenced in this paper, where full velocity measurements are performed on the survey section from Fig. 2, are also marked. The turbine efficiency break-off, Fig. 1, is found to be produced by a corresponding drop in the draft tube pressure recovery. This phenomenon occurs practically at the same discharge value for a specific energy coefficient lower than 1.30.

Throughout this paper the velocity is made dimensionless by the *runner angular speed × runner outlet radius*, and lengths are made dimensionless with respect to the *runner outlet radius R_{ref}* (Fig. 2).

In order to assess the Reynolds number influence on the velocity field at the runner outlet, the same operating point (discharge coefficient, specific energy coefficient) has been investigated for two runner rotational speed values, 500 and 1000 rpm, respectively. The data for dimensionless axial and circumferential velocity components corresponding to the same operating point in Fig. 3 but at two runner rotational speeds are plotted in Fig. 4. According to the IEC 60193 Standard [16], the characteristic Reynolds number Re of the turbine is defined as Re = $UD/\nu = \pi n D^2/60\nu$.

The corresponding Reynolds number of the reduced scale model is changed from 4.2×10^6 (at $n = 500$ rpm) to 8.4×10^6 (at $n = 1000$ rpm) without any significant variation in the dimensionless velocity profiles. Moreover, the axial and circumferential velocity profiles measured at the same discharge coefficient value are not sensitive to specific energy coefficient changes within the investigated range 1.0–1.3, as one can observe Fig. 5. This led us to the conclusion that the only relevant parameter for the investigation further presented in this paper is the turbine discharge coefficient.

3 Analytical Representation of Axial and Circumferential Velocity Profiles

Several swirling flow models have been considered in the literature to study either the vortex stability or the vortex breakdown. We briefly review these models in order to develop a suitable representation for the swirl at the Francis runner outlet. Historically, vortex flow have been first studied in unbounded media and as a result the velocity circulation at very large distance from the vortex axis was naturally chosen as a vortex parameter. Since we are dealing with confined vortices, it is convenient to use the angular velocity at the vortex axis, Ω. A second parameter is a characteristic vortex radius R which measures the vortex core radial extent. These two parameters define the Rankine vortex circumferential velocity,

$$w(r) = \begin{cases} \dfrac{\Omega R^2}{r} & \text{for } r \geq R, \\ \Omega r & \text{for } r < R \end{cases}, \qquad (2)$$

where r is the radial distance from the vortex axis. This simplified model provides a continuous function for $w(r)$, but the derivative is discontinuous. A rigorous theoretical foundation is provided for the Burgers vortex (also known as the Lamb vortex), which gives the circumferential velocity profile as
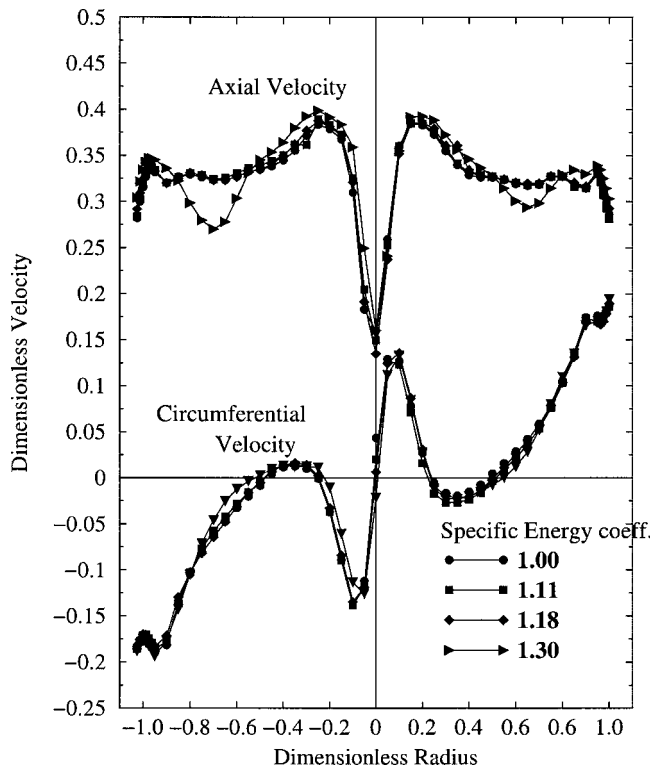
Fig. 5 Specific energy coefficient influence on the dimensionless velocity profiles at operating points with discharge coefficient 0.368

$$w(r) = \frac{\Omega R^2}{r}\left[1 - \exp\left(-\frac{r^2}{R^2}\right)\right]. \tag{3}$$

Formula (3) is an exact solution for a viscous vortex produced by radial inflow and axial outflow where the conditions at large radial distance are irrotational. The relationship between Rankine vortex (2) and Burgers vortex (3) models can be easily seen from Fig. 6. If we take the limit for $r \ll R$ in (3) we get Ωr, while for $r \gg R$ we obtain $\Omega R^2/r$. In conclusion, the Rankine vortex represents the asymptotic behavior of the Burgers vortex for large and small radius with respect to the vortex core extent R.
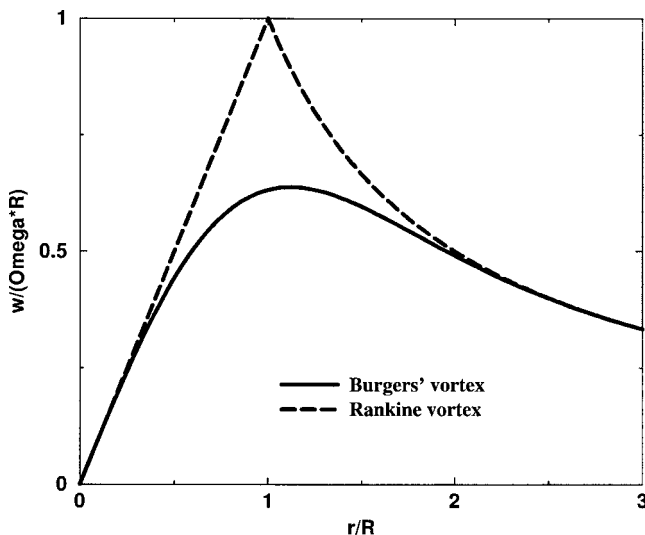

Fig. 6 Circumferential velocity profile for Rankine and Burgers vortex models, respectively

Both the above models consider a uniform axial velocity. It was Batchelor [19] who pointed out that a radial variation in circumferential velocity must be accompanied by a variation in the axial velocity. He showed that in the case of a trailing vortex from one side of a wing in an infinite body of fluid all streamlines originate in a region where the pressure is uniform and the fluid velocity is uniform with only an axial component U_0. When a Rankine vortex circumferential velocity (2) is induced by viscous effects in the boundary layer of the wing, the axial velocity inside the vortex core increases as

$$u = \begin{cases} U_0 & \text{for } r \gg R, \\ \sqrt{U_0^2 + 2\Omega^2(R^2 - r^2)} & \text{for } r < R, \end{cases} \tag{4}$$

Applying the same considerations for the Burgers vortex (3), we obtain

$$u^2 = U_0^2 + \int_r^\infty \frac{1}{r^2}\frac{\partial K^2}{\partial r}dr = U_0^2 + 2\Omega^2 R^2\left[\mathrm{Ei}_1\left(\frac{r^2}{R^2}\right) - \mathrm{Ei}_1\left(2\frac{r^2}{R^2}\right)\right],$$

where $K \equiv rw$ is $(2\pi)^{-1}$ times the circulation around a symmetrically placed circle and Ei_1 is the exponential integral of order one. On the axis the axial velocity is $\sqrt{U_0^2 + 2\ln(2)\Omega^2 R^2}$, which is smaller than the corresponding value for the Rankine vortex $\sqrt{U_0^2 + 2\Omega^2 R^2}$.

Faller and Leibovich [8] have used the following axial velocity functional form to fit their experimental data for a radial guide-vane swirl generator,

$$u(r) = U_0 + U_1\exp\left(-\frac{r^2}{R^2}\right), \tag{5}$$

where U_1 is the difference between the axial velocity on the axis and the axial velocity far away from the axis, U_0. Note that when using (5) together with (3) the vortex core radius R is the same. When $R \gg r$, Eq. (3) becomes $u(r) \approx \Omega r$ since $\lim_{x \to 0}[1 - \exp(-x^2)]/x^2 = 1$, and Eq. (5) becomes $u(r) \approx U_0 + U_1 = \text{const}$.

It was specifically stated in [8] that no theoretical justification for (5) is available. Indeed, in comparison with the axial velocity profile obtained, according to Batchelor, within the constant total head hypothesis

$$\frac{u(r)}{U_0} = \sqrt{1 + 2\left(\frac{\Omega R}{U_0}\right)^2\left[\mathrm{Ei}_1\left(\frac{r^2}{R^2}\right) - \mathrm{Ei}_1\left(2\frac{r^2}{R^2}\right)\right]}, \tag{6a}$$

the functional form (5) rewritten to have the same axial velocity

$$\frac{u(r)}{U_0} = 1 + \left[-1 + \sqrt{1 + 2\ln(2)\left(\frac{\Omega R}{U_0}\right)^2}\right]\exp\left(-\frac{r^2}{R^2}\right), \tag{6b}$$

seems to be completely different. However, one can easily conclude from Fig. 7 that (6b) is a rather good approximation for (6a). Obviously, (6b) or the more general form (5) is more convenient for analytical manipulation.

A more rigorous justification for (5) is attempted by Alekseenko et al. [20] who consider swirling flows with helical symmetry, i.e., the flow characteristics conserve their values along helical lines of pitch $2\pi l$. For axisymmetrical (columnar) helical vortices with a circumferential velocity as in (3) they obtain the axial velocity profile of the form

$$u(r) = U_{\mathrm{axis}} - \frac{\Omega R^2}{l}\left[1 - \exp\left(-\frac{r^2}{R^2}\right)\right], \tag{7}$$

where $U_{\mathrm{axis}} \equiv U_0 + U_1$. One can identify from (7) the characteristic velocity $U_1 = \Omega R^2/l$, and eventually use the length $l = (2\pi)^{-1} \times$ pitch instead of U_1 as a free parameter.

So far we have considered only an elementary vortex representation. However, the experimental data display a more complex structure which should be modeled by a combination of simple vortices. There are two possibilities to consider such combinations. One idea put forward by Alekseenko et al. [20] is to con-
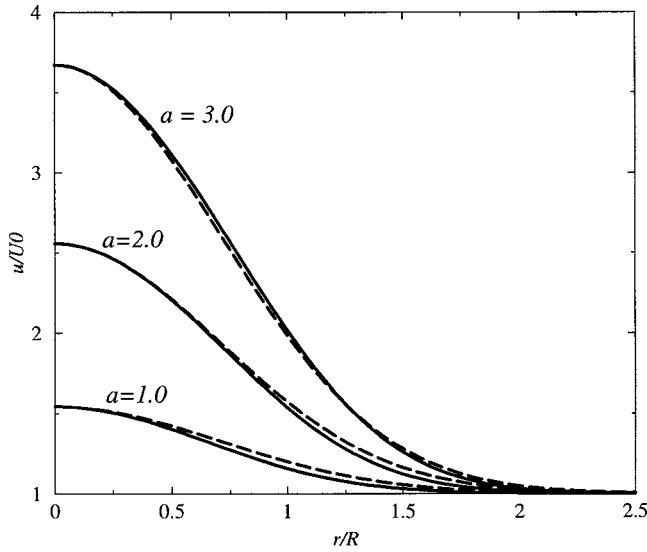
Fig. 7 Axial velocity profiles computed with (6a)—solid lines and (6b)—dashed lines, respectively, for several values of the dimensionless parameter $a \equiv \Omega R / U_0$
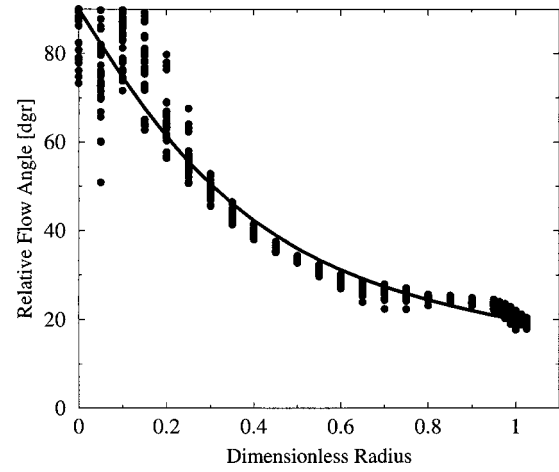

Fig. 8 Relative flow angle computed from the experimental data for axial and circumferential velocity components on the survey section. The solid curve is a least squares fit considering a rigid body rotation for the circumferential velocity and a constant axial velocity.

sider nonoverlapping regions along the radius, with piecewise continuous vorticity distribution. The resulting velocity profiles (both axial and circumferential) are made continuous by a proper choice of the integration constants. Another idea was put forward by Mattner et al. [9] who considered a sum of elementary velocity profiles for both axial and circumferential components. Essentially this second approach becomes equivalent to the first one if the vortices are well separated, i.e., the characteristic radii are well distinct one from each other.

In order to build a suitable vortex combination we should first consider a base flow. Using the dimensionless velocity components u and w, as well as the dimensionless runner tangential velocity, which coincides with the dimensionless radius r according to Sec. 2, the relative flow angle is

$$\beta = \arctan \frac{u}{r - w}. \quad (8)$$

Since the swirling flow examined in this paper is produced by a constant pitch Francis turbine runner, the relative flow angle should be consistent with an approximation corresponding to a solid body rotation, $w = \Omega_0 r$ and $u = U_0$. Indeed, the relative flow angle computed from the experimental data for circumferential and axial velocity can be reasonably fitted with $\beta = \arctan(\text{const}/r)$, as shown in Fig. 8. However, a solid body rotation is a rather crude approximation of the actual velocity profiles. Figures 4 and 5 suggest that two Batchelor vortices, one co-rotating and the other counter-rotating with respect to $w = \Omega_0 r$, and co-flowing/counter-flowing with respect to $u = U_0$, respectively, should be superimposed for consistency with experimental data for circumferential and axial velocity profiles:

$$w(r) = \Omega_0 r + \Omega_1 \frac{R_1^2}{r} \left[1 - \exp\left(-\frac{r^2}{R_1^2} \right) \right] + \Omega_2 \frac{R_2^2}{r} \left[1 - \exp\left(-\frac{r^2}{R_2^2} \right) \right], \quad (9a)$$

$$u(r) = U_0 + U_1 \exp\left(-\frac{r^2}{R_1^2} \right) + U_2 \exp\left(-\frac{r^2}{R_2^2} \right). \quad (9b)$$

If R_0 is the dimensionless survey section radius, then the discharge coefficient can be obtained by integrating the axial velocity profile (9b),

$$\varphi = U_0 R_0^2 + U_1 R_1^2 \left[1 - \exp\left(-\frac{R_0^2}{R_1^2} \right) \right] + U_2 R_2^2 \left[1 - \exp\left(-\frac{R_0^2}{R_2^2} \right) \right]. \quad (10)$$

The functional forms (9) have an eight-parameter set $\mathbf{\Pi} \equiv \{R_1, R_2, \Omega_0, \Omega_1, \Omega_2, U_0, U_1, U_2\}$ to be determined by fitting the experimental data. For each operating point under consideration, with a set of experimental data $(r_j, u_j, w_j) j = 1, \ldots, N$, the error vector $\mathbf{e}(\mathbf{\Pi}) = \{e_k(\mathbf{\Pi})\}$, $k = 1, 2, \ldots, 2N$ is defined as

$$e_k(\mathbf{\Pi}) = \begin{cases} u(r_k, \mathbf{\Pi}) - u_k & \text{for } k = 1, 2, \ldots, N, \\ w(r_{k-N}, \mathbf{\Pi}) - w_{k-N} & \text{for } k = N+1, \ldots, 2N. \end{cases} \quad (11)$$

The error vector includes both axial and circumferential velocity data since the vortex core radii R_1 and R_2 correspond to both velocity components. The parameter set is found by minimizing $\Sigma_{k=1}^{2N}[e_k(\mathbf{\Pi})]^2$, leading to a least squares estimate of $\mathbf{\Pi}$. Let $\mathbf{\Pi}_c$ be the current estimate of $\mathbf{\Pi}$. A new estimate is given by $\mathbf{\Pi}_c + \mathbf{\Pi}_c^*$, where $\mathbf{\Pi}_c^*$ is a solution to

$$[\mathbf{J}^T(\mathbf{\Pi}_c)\mathbf{J}(\mathbf{\Pi}_c) + \mu_c \mathbf{I}]\mathbf{\Pi}_c^* = \mathbf{J}^T(\mathbf{\Pi}_c)\mathbf{e}(\mathbf{\Pi}_c). \quad (12)$$

Here $\mathbf{J}(\mathbf{\Pi}_c)$ is the Jacobian $(2N) \times 8$ matrix evaluated analytically at $\mathbf{\Pi}_c$. The iterative algorithm uses a "trust region" approach with a step bound of δ_c. A solution of Eqs. (12) is first obtained for $\mu_c = 0$. If $\|\mathbf{\Pi}_c^*\|^2 < \delta_c$ this update is accepted. Otherwise, μ_c is set to a positive value and another solution is obtained.

Swirl parameters found by fitting formulas (9) to experimental data for 17 operating points are listed in Table 1. The last two columns contain the values of the discharge coefficient φ computed with (10), and the corresponding relative error with respect to the measured value shown in the first column. This error is a good indicator for the accuracy of the fit, as well as for the measurements overall accuracy. We conclude that (9b) is a very good representation for the axial velocity at the runner outlet and the superposition of three vortices in (9a) accurately represents the experimental data for the circumferential velocity over the whole discharge range under investigation.

Figures 9–14 display the data as well as the curves fitted with (9) for the first six points in Table 1. These operating points cover the investigated discharge domain at a constant head corresponding to the turbine best efficiency operating point. The quality of the fit can be assessed by observing that most of the time the curves approach the experimental points within the measurement

Table 1 Swirl parameters from Eqs. (9) for 17 turbine operating points

Operating point			Swirl parameters									Discharge coefficient	
Discharge coefficient	Energy coefficient	Speed (rpm)	Ω_0	Ω_1	Ω_2	U_0	U_1	U_2	R_1	R_2	Computed Eq. (10)	Error
0.340	1.18	1000	0.31765	−0.62888	2.2545	0.30697	0.01056	−0.31889	0.46643	0.13051	0.344	+1.1%
0.360	1.18	1000	0.26675	−0.79994	3.3512	0.31501	0.07324	−0.29672	0.36339	0.09304	0.363	+0.8%
0.368	1.18	1000	0.27113	−0.80310	3.4960	0.31991	0.08710	−0.27350	0.37291	0.08305	0.372	+1.0%
0.380	1.18	1000	0.27536	−0.81730	3.5187	0.32447	0.10618	−0.23545	0.38125	0.07188	0.381	+0.2%
0.390	1.18	1000	0.27419	−0.86579	3.2687	0.32916	0.12677	−0.19061	0.37819	0.06502	0.389	−0.2%
0.410	1.18	1000	0.28802	−0.96687	1.4590	0.33623	0.19121	−0.09215	0.39108	0.05012	0.409	−0.3%
0.368	1.00	1000	0.27710	−0.77440	3.3913	0.31704	0.08107	−0.24619	0.38128	0.08289	0.368	+0.1%
0.380	1.00	1000	0.26726	−0.83772	3.1082	0.32442	0.11387	−0.19284	0.35948	0.07312	0.380	+0.1%
0.370	1.11	1000	0.28119	−0.77668	3.5520	0.31731	0.08308	−0.25254	0.38947	0.07904	0.369	−0.1%
0.368	1.30	1000	0.29078	−0.79348	3.4239	0.31599	0.10086	−0.25499	0.39536	0.07939	0.371	+0.8%
0.380	1.30	1000	0.27618	−0.85846	3.2696	0.32691	0.12280	−0.19933	0.37413	0.06734	0.386	+1.5%
0.410	1.30	1000	0.27670	−0.96571	2.2165	0.33816	0.17829	−0.10984	0.37930	0.05021	0.407	−0.6%
0.370	1.11	500	0.27854	−0.77371	3.4491	0.31685	0.09058	−0.21118	0.38535	0.07827	0.370	+0.1%
0.340	1.18	500	0.29630	−0.67299	2.7487	0.30509	0.02987	−0.32612	0.41942	0.11679	0.345	+1.6%
0.368	1.18	500	0.27151	−0.78970	3.5902	0.31617	0.09131	−0.22465	0.37450	0.07914	0.369	+0.2%
0.380	1.18	500	0.27659	−0.79568	3.3111	0.32135	0.11063	−0.17502	0.38765	0.07002	0.379	−0.3%
0.410	1.18	500	0.28624	−0.93559	0.76010	0.33243	0.19587	−0.06119	0.39588	0.05147	0.406	−0.9%

errors of 2%. The wall boundary layer is not correctly reproduced since the swirling flow model (9) was specifically built for an inviscid flow analysis.

A main goal of this paper is to find a suitable parametric representation for the swirling flow at the Francis runner outlet. Figure 15 shows the variation of vortex characteristic angular velocities with respect to φ. Linear least squares fits accurately represent $\Omega_0(\varphi)$ and $\Omega_1(\varphi)$, while for $\Omega_2(\varphi)$ a parabolic fit seems to be quite satisfactory. Moreover, one should note that Ω_0 is almost constant over the investigated operating range. The variation of vortex characteristic axial velocities with respect to φ is shown in

Fig. 16, together with the corresponding linear fits. Finally, Fig. 17 displays the dependence of the vortex core radii on φ. A first conclusion from Figs. 15–17 is that swirl parameters in (9) have a smooth, generally linear, variation in φ over the investigated range. As a result, one obtains the velocity components as C^∞ functionals $w(r, \varphi)$ and $u(r, \varphi)$, further employed in a parametric study of the flow stability or other properties.

According to the qualitative picture of the three vortex system presented in Table 2, Vortex 0 is a rigid body rotation with angular speed Ω_0 and we can associate with it a constant axial velocity U_0. Vortex 1, which has a vortex core extent about half the wall radius, is counter-rotating and co-flowing with respect to vortex 0. The strength of this vortex, both in Ω_1 as well as in U_1 is growing
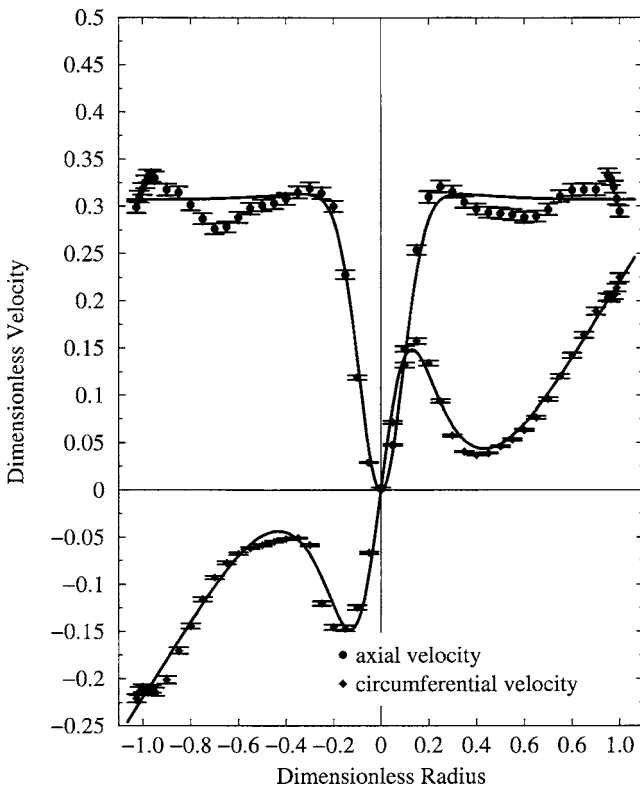

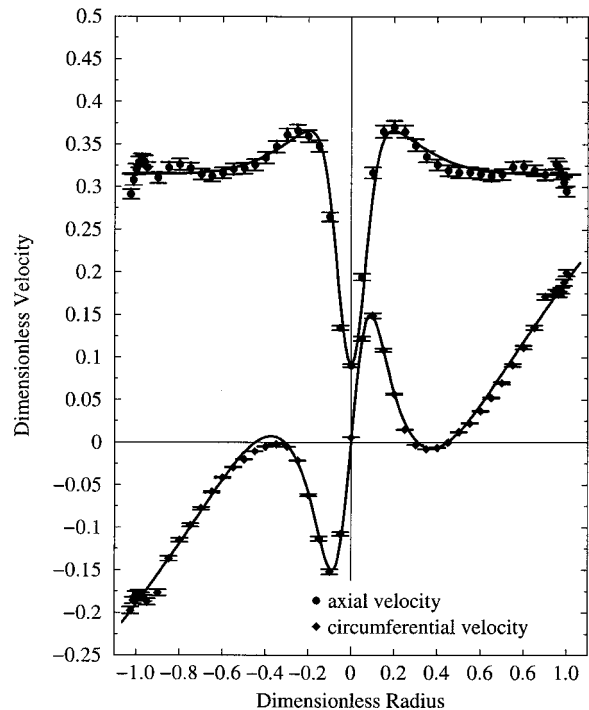**Fig. 9 Axial and circumferential velocity profiles at discharge $\varphi = 0.340$**

Fig. 10 Axial and circumferential velocity profiles at discharge $\varphi = 0.360$

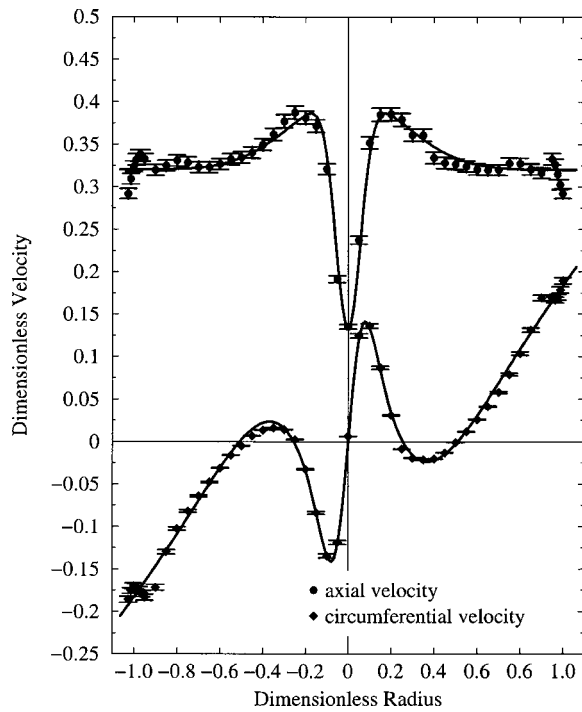**Fig. 11** Axial and circumferential velocity profiles at discharge $\varphi = 0.368$

Fig. 13 Axial and circumferential velocity profiles at discharge $\varphi = 0.390$

as the flow rate increases. Vortex 2 has a core at least four times smaller than vortex 1, is co-rotating and counter-flowing with respect to vortex 0, and its strength increases as the flow rate decreases. Note that as the flow rate increases (eventually beyond the upper limit in our investigation) vortex 2 will vanish. These two Batchelor vortices are mainly responsible for the swirling
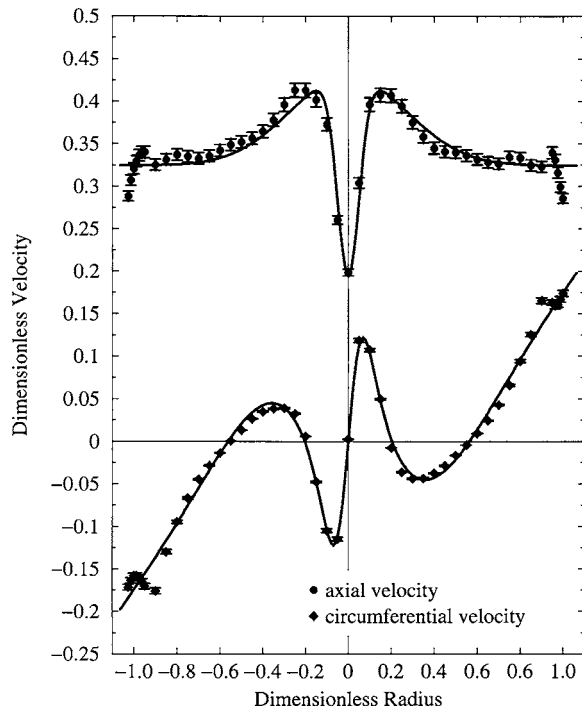
flow behavior. For φ smaller than the design value a wake-like axial velocity is developed (Fig. 9) while for larger φ the axial velocity has a jetlike profile (Fig. 14).

4 Swirling Flow Mathematical Model and Numerical Approach

Theoretical analysis of swirling flows can employ tools ranging from simplified axisymmetric, inviscid steady [11] or unsteady

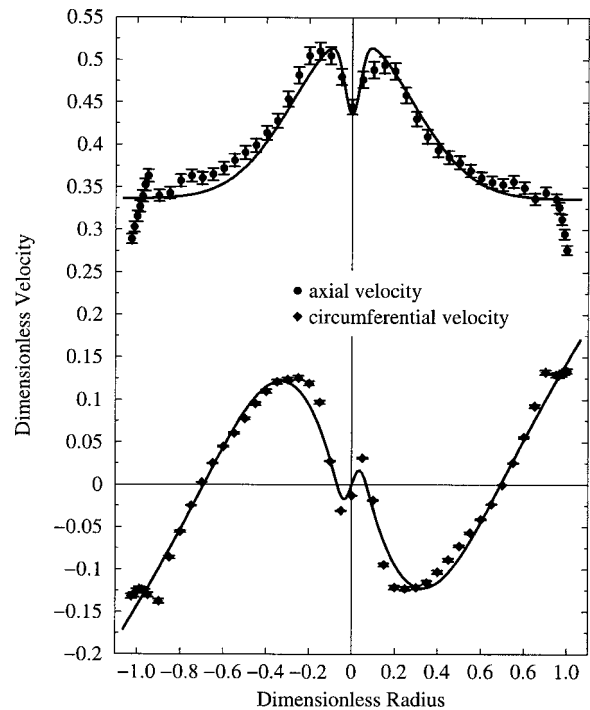**Fig. 12** Axial and circumferential velocity profiles at discharge $\varphi = 0.380$
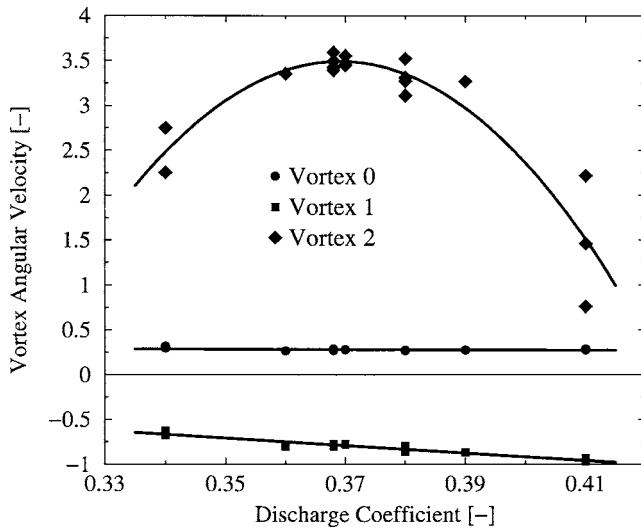

Fig. 14 Axial and circumferential velocity profiles at discharge $\varphi = 0.410$

Fig. 15 Characteristic angular velocities Ω_0, Ω_1, and Ω_2 versus discharge coefficient φ

Fig. 17 Vortex core radii R_1 and R_2 versus discharge coefficient φ

[21] flow models to full 3D laminar [10] or turbulent [22] numerical simulation. However, it is useful to first examine the swirling flow at the draft tube inlet before performing an analysis of the flow in the straight cone or even in the whole 3D geometry. Such results may be quite useful if there is a correlation (even qualitative) with the overall draft tube behavior over a certain range of discharge variation.

If we restrict for now our analysis only for the runner outlet section, several simplifications must be admitted, and the results must be interpreted accordingly. We consider a steady mean flow with axial and circumferential velocity profiles derived from experimental data in Sec. 3. An inviscid incompressible fluid is considered, since our swirling flow representation does not account for the boundary layer near the wall.

The cylindrical flow assumption may not seem appropriate for the flow in the draft tube cone shown in Fig. 2, since it is known that the diverging pipe geometry precipitates the formation of breakdown by creating an adverse pressure gradient along the vortex axis. Shtern and Hussain [23] show that the nonparallel character of jets strongly affects their stability. Flow deceleration significantly enhances the shear-layer instability for both swirl-free and swirling jets. Buntine and Saffman [24] study a diverging flow using the steady axisymmetric Euler flow model. They show
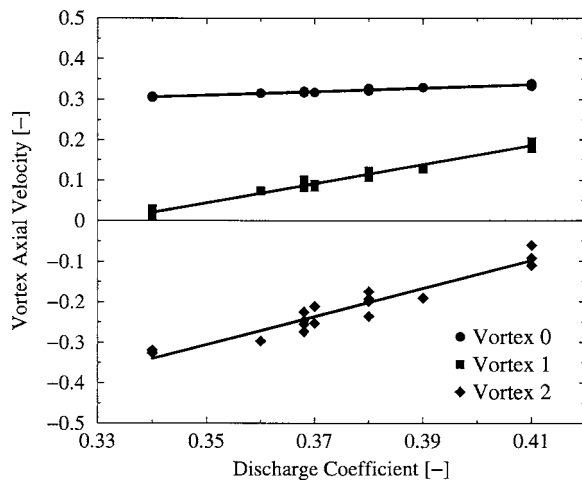
that solutions fail to exist or, alternatively, that flow ceases to be unidirectional, so that the breakdown can be inferred, when a parameter measuring the relative magnitude of rotation and axial flow exceeds critical values depending upon geometry and inlet profiles. However, for slightly diverging duct of angles less than 2°, Tsai [25] shows that the flow can be considered locally parallel for the flow stability analysis. This parallel flow assumption is not quite restrictive even for the 8.5° cone angle considered in this study. The diffusion process takes place only close to the wall, leading to a thin 3D boundary layer, as it can be seen from the measured velocity distribution (Figs. 4 and 5). Therefore, by neglecting the retarding influence of the wall, we can assume that the bulk flow is parallel. As far as the mean flow is concerned, the radial velocity is one order of magnitude smaller than the axial velocity since $v/u < \tan 8.5° \approx 0.15$.

Within these assumptions, the mathematical model to be considered here corresponds to the theory of finite transitions between frictionless cylindrical flows originally developed by Benjamin [11]. The equation of continuity for axisymmetric incompressible flows is automatically satisfied by introducing the streamfunction $\psi(z, r)$ such that the axial and radial velocity components can be written as

$$u = \frac{1}{r}\frac{\partial\psi}{\partial r} \quad \text{and} \quad v = -\frac{1}{r}\frac{\partial\psi}{\partial z}. \tag{13}$$

When applied to a circuit around a particular stream-surface ψ = const Kelvin's theorem shows rw to be a constant. Thus in general $rw \equiv K(\psi)$, where K is a function of ψ alone. Also, on a streamsurface the total specific energy $H = p/\rho + (u^2 + v^2 + w^2)/2$ is constant by Bernoulli's theorem, thus H is a function of ψ alone. The momentum equation for the steady, axisymmetric swirling flow becomes

$$\frac{1}{r^2}\left(\frac{\partial^2\psi}{\partial z^2} + \frac{\partial^2\psi}{\partial r^2} - \frac{1}{r}\frac{\partial\psi}{\partial r}\right) = H'(\psi) - \frac{K(\psi)K'(\psi)}{r^2}, \tag{14}$$

which is known in literature as the Long-Squire or Bragg-Hawthorne equation. Goldshtik and Hussain [14] noted that, in fact, Eq. (14) was derived much earlier by Meissel (in 1873). The prime denotes differentiation with respect to ψ. By introducing the new variable $y = r^2/2$ Eq. (14) can be rewritten as

$$\frac{\partial^2\psi}{\partial y^2} + \frac{1}{2y}\frac{\partial^2\psi}{\partial z^2} = H'(\psi) - \frac{K(\psi)K'(\psi)}{2y}. \tag{15}$$

If we substitute $Y_1 = R_1^2/2$ and $Y_2 = R_2^2/2$ the axial velocity profile (9b) can be written as

Fig. 16 Characteristic axial velocities U_0, U_1, and U_2 versus discharge coefficient φ

Table 2 Swirling flow structure

	Vortex 0	Vortex 1	Vortex 2
Circumferential velocity	rigid body rotation	counter-rotating	co-rotating
Axial velocity	constant	co-flowing	counter-flowing
Vortex core radius	—	$\sim 0.4 R_0$	$\sim 0.1 R_0$

$$u(y) = U_0 + U_1 \exp(-y/Y_1) + U_2 \exp(-y/Y_2). \qquad (16)$$

Since from (13) $u = \partial\psi/\partial y$, the streamfunction for the above velocity profile is

$$\psi(y) = U_0 y + U_1 Y_1[1 - \exp(-y/Y_1)] + U_2 Y_2[1 - \exp(-y/Y_2)], \qquad (17)$$

where without loss of generality we have considered $\psi = 0$ on the symmetry axis.

The discharge coefficient φ from Eq. (10) can be rewritten as

$$\varphi = 2U_0 Y_0 + 2U_1 Y_1[1 - \exp(-Y_0/Y_1)] + 2U_2 Y_2[1 - \exp(-Y_0/Y_2)], \qquad (18)$$

where $Y_0 = R_0^2/2$. As a result, at the wall we have $\psi_{\text{wall}} \equiv \psi(Y0) = \varphi/2$.

For a mean flow with negligible radial velocity, the right-hand side in Eq. (15) is simply du/dy,

$$H'(\psi) - \frac{K(\psi)K'(\psi)}{2y} := \psi \xrightarrow{\text{Eq. 17}} y \rightarrow -\frac{U_1}{Y_1}\exp\left(-\frac{y}{Y_1}\right)$$
$$- \frac{U_2}{Y_2}\exp\left(-\frac{y}{Y_2}\right).$$

The map $\Psi \rightarrow y$ has to be computed numerically, for example using the Newton iterative method,

$$y^{(m+1)} = y^{(m)} + \frac{\Psi - \psi(y^{(m)})}{u(y^{(m)})}, \quad \text{with initial guess } y^{(0)} = Y_0\frac{\Psi}{\varphi/2},$$

where m denotes the iteration index. Note that due to the nonlinearity of this map, the solution of Eq. (15) with boundary conditions $\psi(0) = 0$ and $\psi(Y_0) = \varphi/2$ may be *nonunique*. To investigate this feature let us consider the streamfunction in (15) of the form

$$\psi(z,r) = \Psi(y) + \varepsilon\tilde{\psi}(y)\exp(i\kappa z) \qquad (19)$$

where $\Psi(y)$ is the base flow given by (17), $\tilde{\psi}(y)$ is a perturbation of the base flow (Fig. 18), and κ is the axial wave number of this perturbation.

Introducing (19) in Eq. (15) one obtains the linearized equation

$$\frac{d^2\tilde{\psi}}{dy^2} - \left(H''(\Psi) - \frac{K'^2(\Psi) + K(\Psi)K''(\Psi)}{2y}\right)\tilde{\psi} = \frac{\kappa^2}{2y}\tilde{\psi}. \quad (20a)$$

Of course, in order to preserve the flow rate the perturbation must satisfy homogeneous boundary conditions

$$\tilde{\psi}(0) = \tilde{\psi}(Y_0) = 0. \qquad (20b)$$

Equations (20) define a generalized eigenvalue problem. The eigenvalues κ^2 can be computed numerically once the problem is discretized. The expression inside square brackets on the left-hand side can be easily evaluated once an analytical swirl representation is available:

$$C(y) \equiv H''(\Psi) - \frac{K'^2(\Psi) + K(\Psi)K''(\Psi)}{2y} = \frac{1}{u}\frac{d^2u}{dy^2} - \frac{K}{2y^2u^2}\frac{dK}{dy}. \qquad (21)$$

If we consider a grid $y_0 = 0, y_1, \ldots, y_1, \ldots, y_N, y_{N+1} = Y_0$ and a piecewise linear approximation of the solution $\tilde{\psi}(y) \approx \Sigma_j \tilde{\psi}_j N_j(y)$, the finite element discretization of problem (20) can be written in matrix form as

$$\mathbf{A}\tilde{\boldsymbol{\psi}} = \kappa^2 \mathbf{B}\tilde{\boldsymbol{\psi}}, \qquad (22a)$$

where $\tilde{\boldsymbol{\psi}}$ is the nodal values vector, and

$$A_{ij} = -\int \frac{dN_i(y)}{dy}\frac{dN_j(y)}{dy}dy - \int N_i(y)C(y)N_j(y)dy,$$
$$(22b)$$
$$B_{ij} = \int \frac{N_i(y)N_j(y)}{2y}dy$$

are $N \times N$ tridiagonal symmetric matrices. Obviously the matrix entries in (22b) are evaluated only for the N interior nodes, due to the homogeneous Dirichlet conditions (20b). The GVCSP procedure from the International Math and Statistics Libraries (IMSL) [26] is used here to compute all of the eigenvalues and eigenvectors of the generalized real symmetric eigenvalue problem (22a), with $\mathbf{B}$ symmetric and positive definite.

Let us summarize now the swirling flow model according to the synoptic Fig. 18. Once the analytical representation for axial and circumferential velocity components has been established, the mean flow streamfunction can be computed. A streamtube $\Psi = \text{const}$ may be subject to axisymmetric perturbations $\varepsilon\tilde{\psi}$, which are the eigenfunctions of problem (20). Such a perturbation can be
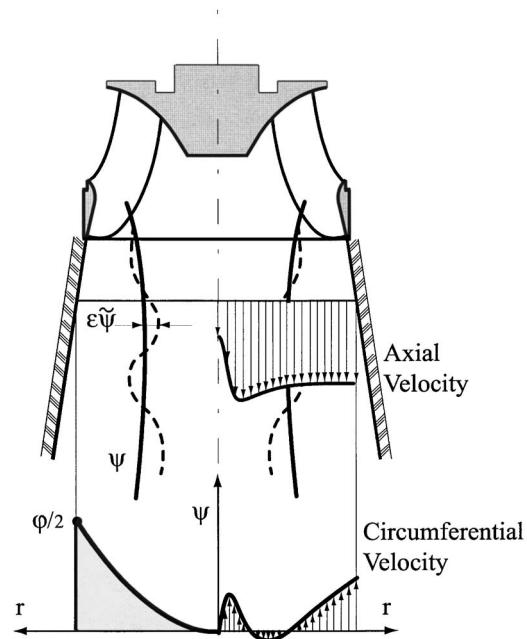

Fig. 18 Synoptic view of the model for swirling flow downstream of a Francis turbine runner
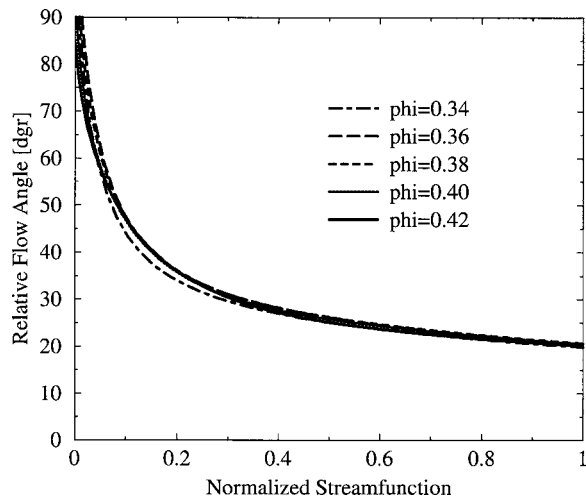
Fig. 19 Relative flow angle on streamtubes

Fig. 20 The swirlnumber S from (23a) versus the discharge coefficient φ

sustained or not depending on the sign of the corresponding eigenvalue κ^2, according to the analysis to be presented in the next section.

5 Analysis of the Swirling Flow

An important property of the swirling flows downstream a constant pitch hydraulic turbine runner is that the relative flow angle depends only on the blade exit angle provided that the flow remains attached. This is certainly the case for a turbine runner operating in the neighborhood of the best efficiency point, therefore we can expect that the relative flow angle remains practically independent for the operating points of interest in this study. Moreover, due to negligible retarding forces, the global moment of momentum of the flow at the runner outlet should remain constant in the cone. Therefore, the relative flow angle (8) should depend only on the streamtube, i.e., on the normalized streamfunction $\psi/(\varphi/2)$ (Fig. 19). In other words, the relative flow angle on the survey section at runner outlet is practically constant on a streamtube originating at the same radius on the blade trailing edge, being determined by the blade exit angle irrespective of the discharge. This shows the direct correlation between the runner blade design and the kinematics of the swirl on the draft tube inlet. Moreover, the significant changes in the circumferential and axial velocity profiles can be associated only with the streamtube's cross-section variation downstream the blade trailing edge, as the discharge is modified.

The above considerations on the relative flow angle (8) help us understand the striking feature that the flow rotates in some radius range in the opposite direction to that at smaller and larger radii. Since the relative flow angle remains constant on a streamtube, an increase in the dimensionless axial velocity u must be accompanied by an increase in the dimensionless relative circumferential velocity r-w. In consequence, as the axial flow accelerates, i.e., a jetlike axial velocity profile is developed when the discharge increases, the corresponding absolute circumferential velocity w becomes negative in order to increase r-w, thus keeping $u/(r$-$w)$ practically constant in Eq. (8).

A global quantitative description of the swirling flow is provided by the swirl number S defined as the axial flux of swirl momentum divided by the axial flux of axial momentum [[27], p. 2],
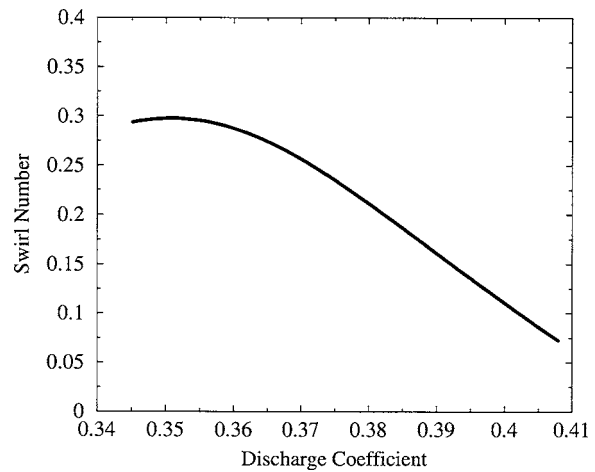
$$S = \frac{\displaystyle\int_0^{R_0} \rho u (rw) r\, dr}{R_0 \displaystyle\int_0^{R_0} (\rho u^2 + p - p_{R_0}) r\, dr}, \quad (23a)$$

where p_{R_0} is the pressure at the wall. The pressure term in (23a) can be evaluated using the equation of radial equilibrium,

$$\frac{\partial p}{\partial r} = \frac{\rho w^2}{r} \Rightarrow p - p_{R_0} = -\int_r^{R_0} \frac{\rho w^2}{r} dr. \quad (23b)$$

The swirl number computed for the swirling flow given by (9), with parameters from Figs. 15–17, is plotted versus the discharge coefficient in Fig. 20. One can see that for the investigated range of φ the swirl number decreases as the discharge increases, but nevertheless the variation is smooth.

More interesting and useful conclusions can be drawn from the analysis of eigenvalues κ^2 and the corresponding eigenvectors in (20). If $\kappa^2 < 0$, then κ is imaginary and the exponential factor in (19) will be $\exp(\pm|\kappa|z)$. As we move downstream the current section, $z > 0$, the only physically acceptable solution corresponds to $\exp(-|\kappa|z)$, showing an exponential damping of $\tilde{\psi}$. A swirl configuration for which all eigenvalues are negative is unable to sustain axisymmetric small-disturbance standing waves and it was termed *supercritical* by Benjamin [11]. On the other hand, if at least one eigenvalue κ^2 is positive, then the perturbation will take the form of a standing wave $\exp(\pm i\kappa z)$, and the corresponding flow is termed *subcritical*. All physical interpretations attempted for the distinction between supercritical and subcritical states were mainly focused at the vortex breakdown phenomena. Benjamin's original interpretation was that for a given distribution of $H(\psi)$ and $K(\psi)$ one possible state of flow is subcritical and the conjugate state is supercritical. A deduction of this theory is that, compared with their conjugates, supercritical flows possess a deficiency of total momentum defined as the integral of axial momentum flux plus pressure over a cross section. This property would imply that supercritical flows are liable to undergo spontaneous transitions to subcritical state. Later, this theory came under quite heavy criticism, mostly because of its lack of explaining the axial flow reversal associated with the vortex breakdown. For example, Hall [28] particularly disagrees with the hydraulic jump analogy. Leibovich [29] considers that the most serious weakness of Benjamin's theory is that there is no clear way to relate it to experiments which, at high Reynolds numbers, always have unsteady, non-axisymmetric wakes. A decade ago Keller [12]
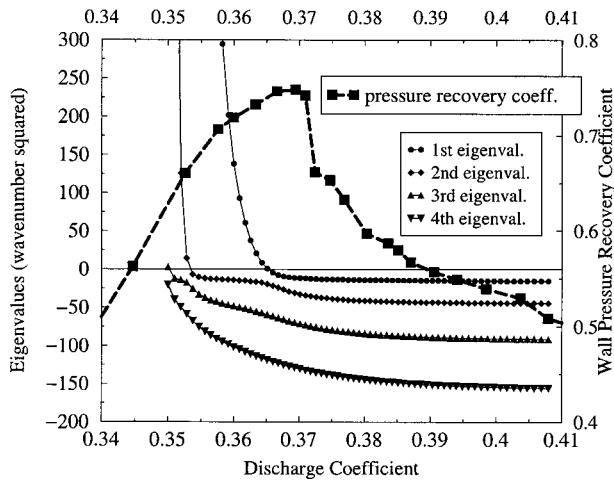
Fig. 21 The first four eigenvalues and the pressure recovery coefficient function of the discharge coefficient

Fig. 22 Eigenmodes corresponding to the largest (positive) eigenvalue for subcritical swirling flows

pointed that various authors or even schools have conflicting views on the correct interpretation of the physics of vortex breakdown. Moreover, in his opinion, Benjamin's theory already contained most ideas for a successful theory of axisymmetric vortex breakdown but it was missing the definition of the total head circulation in regions with flow reversal, i.e., beyond the upstream interval of streamfunction values. The stagnation model emerged, where the total head is uniform and circulation vanishes in the domain of flow reversal, and was lately employed by Rusak et al. [30] to examine axisymmetric vortex breakdown in a finite length pipe. They present a comprehensive study of the Burgers vortex behavior, using both steady and unsteady axisymmetric inviscid flow models. Using essentially the same linearized eigenvalue problem, they determined the critical swirl level above which the base solution will evolve downstream to a solution that is a global (not local) minimizer of a certain functional. The flow in the pipe is computed explicitly, thus supporting the conclusions. However, no attempt has been made to directly correlate the computational results with any experimental data.

The approach we take in this paper is to examine the transition of the swirling flow downstream a Francis turbine runner from subcritical to supercritical as the discharge coefficient increases and to correlate the critical state with the experimentally observed sudden drop in the draft tube pressure recovery coefficient. A similar approach was advocated by Goldshtik and Hussain [14] who consider that vortex breakdown necessarily occurs when solution nonuniqueness is achieved by a continuous change in flow parameters. Moreover, we consider that valuable insight might be gained also by examining the eigenmodes $\widetilde{\psi}$ corresponding to positive eigenvalues.

Let us examine first the main result of this paper, inferred from Fig. 21. For $\varphi > 0.365$, and correspondingly smaller swirl numbers, all eigenvalues from (20) are negative, thus the flow is supercritical and cannot sustain axisymmetric standing waves. However, for $\varphi < 0.365$ the largest eigenvalue becomes positive, followed by the next eigenvalues as φ decreases, and the flow is subcritical with standing waves described by the corresponding eigenvectors $\widetilde{\psi}$. The critical state occurs according to our computations at $\varphi = 0.365$. This discharge value is quite close (only 1.3% smaller) to the value of $\varphi = 0.37$ where the sudden drop in draft tube pressure recovery coefficient is observed. It seems reasonable to assume that the critical state is directly related to this experimentally observed phenomenon, since by trying several draft tube geometries while keeping the same runner (and the swirling flow) the same behavior has been observed practically at the same discharge. While reaching the critical swirl configuration seems to be
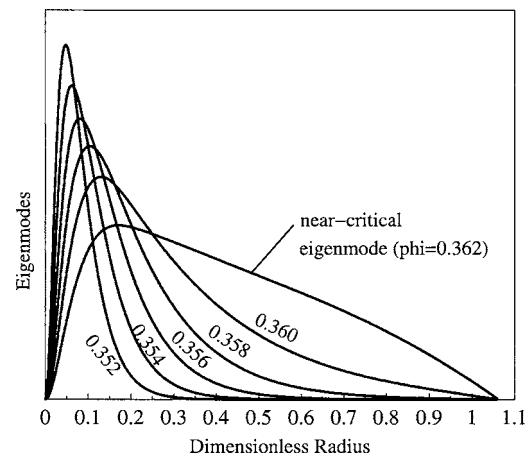
the cause, the actual physical mechanism by which the pressure recovery suffers an abrupt change cannot be inferred from the present analysis. Experimental [2] as well as numerical [3,4] investigations offer a comprehensive analysis of the Francis turbine draft tube flow.

Several eigenmodes $\widetilde{\psi}(r)$ corresponding to the largest eigenvalue for subcritical flows are shown in Fig. 22. Since the eigenmodes are defined up to a multiplicative constant, it makes no sense to have marks on the vertical axis. One can easily see that as the discharge coefficient decreases the support of the eigenmode shrinks toward the axis neighborhood. It means that the induced velocity perturbations, for example their real part

$$\widetilde{u} = \frac{d\widetilde{\psi}}{dy}\cos(\kappa z) \quad \text{and} \quad \widetilde{v} = \frac{\kappa\widetilde{\psi}}{\sqrt{2y}}\sin(\kappa z),$$

are confined closer to the axis as φ decreases. Moreover, the relative amplitude of the perturbation increases since κ gets larger (leading to larger $\widetilde{v}$) and also the slope at the origin increases (leading to larger $\widetilde{u}$) on the axis. Although no vortex breakdown bubble is observed in the draft tube cone, the above velocity perturbations can be related to the axial velocity deficit reduction further downstream. This mechanism of reducing the "wakelike" axial velocity nonuniformity might be responsible for the improvement in the draft tube overall performance as the discharge gets smaller than the critical value. For even smaller discharge, more eigenmodes are successively present. For example, Fig. 23 presents the first two eigenmodes at $\varphi = 0.348$, corresponding to the two positive eigenvalues. While the first eigenmode is confined near the axis, the second one is not, but its behavior will follow the same pattern when further decreasing the discharge.

6 Conclusions

The present work started from the idea that the swirling flow configuration at the outlet of a Francis turbine runner has a major influence on the overall behavior of the flow downstream in the draft tube.

We have investigated experimentally the velocity axial and circumferential components at the runner outlet for 17 operating points within the turbine normal operating range. Then, a suitable analytical representation of the velocity profiles is developed, with the turbine discharge as an independent parameter. It is shown that the swirling flow in the survey section can be accurately represented using a superposition of three distinct vortices: a rigid body rotation motion, a counter-rotating and co-flowing Batchelor vortex with large core radius, and a co-rotating and counter-flowing Batchelor vortex with small vortex core. The eight parameters of
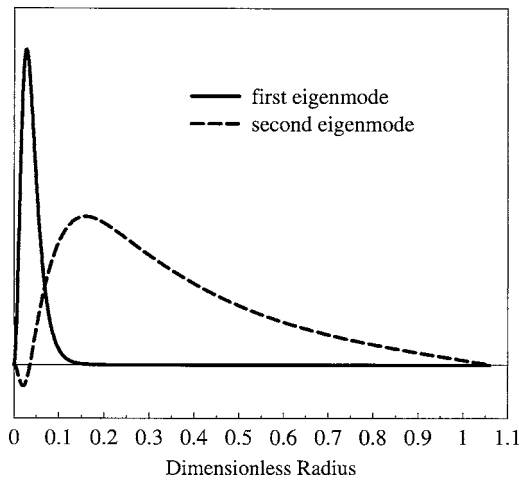
Fig. 23 First two eigenmodes for subcritical swirling flow at $\varphi = 0.348$

this three-vortex system are determined by fitting the experimental data and are shown to vary smoothly (generally linear) with the discharge coefficient.

The flow at the runner outlet is then analyzed using the mathematical model for a steady, axisymmetric, and inviscid swirling flow. Following Benjamin's theory of finite transitions between frictionless cylindrical flows, we have performed an eigenvalue analysis of the linearized problem. It is shown that the swirl reaches a critical state at discharge $\varphi = 0.365$. For larger discharge the flow ingested by the draft tube is supercritical, while at lower discharge it is subcritical. The critical state occurs quite close to the discharge $\varphi = 0.370$ where a sudden variation in the draft tube pressure recovery, as well as in the overall turbine efficiency, is experimentally observed. For the particular turbine under investigation this discharge value happens to correspond to the best efficiency point, leading to a negative impact on the turbine regulation.

A qualitative correlation between the swirling flow at the draft tube inlet and the complex flow behavior further downstream may be inferred in conjunction with the Werlé-Legendre separation in the bend, discovered by Mauri et al. [15]. For subcritical swirling flow the sustained axisymmetric waves weaken the integrity of the vortex core, thus preventing the interaction with secondary flows in the draft tube bend. As the swirling flow reaches the critical state, and becomes supercritical as the discharge increases, the vortex core is no longer affected by axisymmetric perturbations, thus being able to trigger a global Werlé-Legendre separation that blocks the right channel of the draft tube and accelerates the flow in the other channel. The static pressure recovery is strongly affected, leading to an important loss in the overall machine efficiency.

Our analysis leads to the conclusion that when designing or optimizing turbine runners one should avoid reaching a critical state for the swirl at the runner outlet within the normal operating range.

Acknowledgment

Nomenclature

$$
\begin{aligned}
A_{ref} &= \text{reference section area} \\
H &= \text{Bernoulli's total head} \\
K &= \text{circulation function} \\
Q &= \text{turbine discharge} \\
R_0 &= \text{survey section radius} \\
R_{ref} &= \text{reference section radius} \\
R_1, R_2 &= \text{vortex core radii} \\
S &= \text{swirl number} \\
U_0, U_1, U_2 &= \text{vortex characteristic axial velocities} \\
p &= \text{pressure} \\
r &= \text{radial coordinate} \\
u, \tilde{u} &= \text{axial velocity and its perturbation} \\
v, \tilde{v} &= \text{radial velocity and its perturbation} \\
w &= \text{circumferential velocity} \\
y &= \text{auxiliary variable} \\
z &= \text{axial coordinate, aligned with the vertical machine axis} \\
\Omega_0, \Omega_1, \Omega_2 &= \text{vortex characteristic angular velocities} \\
\beta &= \text{relative flow angle} \\
\chi &= \text{draft tube wall pressure recovery coefficient} \\
\kappa &= \text{wave number} \\
\psi &= \text{streamfunction} \\
\varphi &= Q/\omega R_{ref} A_{ref} \text{ discharge coefficient} \\
\rho &= \text{density}
\end{aligned}
$$

References

[1] Escudier, M., 1987, "Confined Vortices in Flow Machinery," Annu. Rev. Fluid Mech., **19**, pp. 27–52.
[2] Avellan, F., 2000, "Flow Investigation in a Francis Draft Tube: the FLINDT Project," in *Proceedings of the 20th IAHR Symposium*, Charlotte, NC.
[3] Mauri, S., 2002, "Numerical Simulation and Flow Analysis of an Elbow Diffuser," Ph.D. thesis, École Politechnique Fédérale de Lausanne, Lausanne, Switzerland.
[4] Mauri, S., Kueny, J.-L., and Avellan, F., 2000, "Numerical Prediction of the Flow in a Turbine Draft Tube. Influence of the Boundary Conditions," FEDSM'00-11084, *Proceedings of the ASME 2000 Fluids Engineering Division Summer Meeting*, Boston, MA.
[5] Engström, T. F., 2003, "Simulation and Experiments of Turbulent Diffuser Flow With Hydropower Applications," Ph.D. thesis, Luleå University of Technology, Luleå, Sweden.
[6] Cervantes, M. J., 2003, "Effects of Boundary Conditions and Unsteadiness on Draft Tube Flow," Ph.D. thesis, Luleå University of Technology, Luleå, Sweden.
[7] Harvey, J. K., 1962, "Some Observations of the Vortex Breakdown Phenomenon," J. Fluid Mech., **14**, pp. 585–592.
[8] Faler, J. H., and Leibovich, S., 1977, "Disrupted States of Vortex Flow and Vortex Breakdown," Phys. Fluids, **20**(9), pp. 1385–1400.
[9] Mattner, T. W., Joubert, P. N., and Chong, M. S., 2002, "Vortical Flow. Part 1. Flow Through a Constant Diameter Pipe," J. Fluid Mech., **463**, pp. 259–291.
[10] Snyder, D. O., and Spall, R. E., 2000, "Numerical Simulation of Bubble-Type Vortex Breakdown Within a Tube-and-Vane Apparatus," Phys. Fluids, **12**(3), pp. 603–608.
[11] Benjamin, T. J., 1962, "Theory of the Vortex Breakdown Phenomenon," J. Fluid Mech., **14**, pp. 593–629.
[12] Keller, J. J., 1995, "On the Interpretation of Vortex Breakdown," Phys. Fluids, **7**(7), pp. 1695–1702.
[13] Leibovich, S., 1978, "The Structure of Vortex Breakdown," Annu. Rev. Fluid Mech., **10**, pp. 221–246.
[14] Goldshtik, M., and Hussain, F., 1998, "Analysis of Inviscid Vortex Breakdown in a Semi-infinite Pipe," Fluid Dyn. Res., **23**, pp. 189–234.
[15] Mauri, S., Kueny, J.-L., and Avellan, F., 2004, "Werlé-Legendre Separation in a Hydraulic Machine Draft Tube," ASME J. Fluids Eng., **126**, pp. 976–980.
[16] International Electrotechnical Commision, 1999, "Hydraulic Turbines, Storage Pumps and Pump-Turbines—Model Acceptance Tests," International Standard IEC 60193, 2nd ed.
[17] Ciocan, G. D., 1998, "Contribution à l'Analyse des Ecoulements 3D Complexes en Turbomachines," Ph.D. thesis, Institut National Polytechnique de Grenoble, Grenoble, France.
[18] Ciocan, G. D., Avellan, F., and Kueny, J.-L., 2000, "Optical Measurement Techniques for Experimental Analysis of Hydraulic Turbines Rotor-Stator Interaction," FEDSM2000-11056, *Proceedings of the ASME 2000 Fluids Engineering Division Summer Meeting*, Boston, MA.
[19] Batchelor, G. K., 1964, "Axial Flow in Trailing Line Vortices," J. Fluid Mech.,

$\quad$ **20**(4), pp. 645–658.

[20] Alekseenko, S. V., Kuibin, P. A., Okulov, V. L., and Shtork, S. I., 1999, "Helical Vortices in Swirl Flow," J. Fluid Mech., **382**, pp. 195–243.

[21] Wang, S., and Rusak, A., 1997, "The Dynamics of a Swirling Flow in a Pipe and Transition to Axisymmetric Vortex Breakdown," J. Fluid Mech., **340**, pp. 177–223.

[22] Lu, P., and Semião, V., 2003, "A New Second-Moment Closure Approach for Turbulent Swirling Confined Flow," Int. J. Numer. Methods Fluids, **41**, pp. 133–150.

[23] Shtern, V., and Hussain, F., 2003, "Effect of Deceleration on Jet Instability," J. Fluid Mech., **480**, pp. 283–309.

[24] Buntine, J. D., and Saffman, P. G., 1995, "Inviscid Swirling Flows and Vortex Breakdown," Proc. R. Soc. London, Ser. A, **449**, pp. 139–153.

[25] Tsai, C.-Y., 1980, "Examination of Group-Velocity Criterion for Breakdown of Vortex Flow in a Divergent Duct," Phys. Fluids, **23**(5), pp. 864–870.

[26] Visual Numerics, 2003, "IMSL Fortran Library User's Guide. Mathematical Functions in Fortran."

[27] Gupta, A. K., Lilley, D. G., and Syred, N., 1984, *Swirl Flows*, Abacus Press, Cambridge, MA.

[28] Hall, M. G., 1972, "Vortex Breakdown," Annu. Rev. Fluid Mech., **4**, pp. 195–218.

[29] Leibovich, S., 1984, "Vortex Stability and Breakdown: Survey and Extension," AIAA J., **22**(9), pp. 1192–1206.

[30] Rusak, Z., Wang, S., and Whiting, C. H., 1998, "The Evolution of a Perturbed Vortex in a Pipe to Axisymmetric Vortex Breakdown," J. Fluid Mech., **366**, pp. 211–237.

Mathematical modelling of swirling flow in hydraulic turbines for the full operating range

R.F. Susan-Resiga [a,*], S. Muntean [b], F. Avellan [c], I. Anton [a]

[a] *"Politehnica" University of Timişoara, Hydraulic Machinery Dpt., Bvd. Mihai Viteazu 1, RO-300222 Timişoara, Romania*
[b] *Romanian Academy - Timişoara Branch, Bvd. Mihai Viteazu 24, RO-300223, Timişoara, Romania*
[c] *École Polytechnique Fédérale de Lausanne, Laboratory for Hydraulic Machines, Av. de Cour 33Bis, CH-1007, Lausanne, Switzerland*

ARTICLE INFO

ABSTRACT

We introduce and validate a novel mathematical model for computing the radial profiles of both axial and circumferential velocity components, respectively, of the swirling flow exiting the runner of hydraulic turbines within the full operating range. We assume an incompressible, inviscid, axisymmetrical, and steady swirling flow, with vanishing radial velocity at runner outlet. First we find the correlation between the flux of moment of momentum downstream the turbine runner and the operating regime given by turbine's discharge and head. Second, we express the relationship between the axial and circumferential velocity components, corresponding to the fixed pitch runner blades, using the swirl-free velocity instead of the traditional relative flow angle at runner outlet. It is shown that the swirl-free velocity profile practically does not change with the operating regime. Third, we introduce a constrained variational problem corresponding to the minimization of the flow force while maintaining the prescribed discharge and flux of moment of momentum. This formulation also accounts for a possible central stagnant region to develop when operating the turbine far from the best efficiency point. Fourth, we show that by representing the unknown axial velocity profile with a suitable Fourier–Bessel series, the discharge constraint can be automatically satisfied. The resulting numerical algorithm is robust and produces results in good agreement with available data for both axial and circumferential velocity profiles measured on a model Francis turbine at several operating regimes. Our mathematical model is suitable for the early optimization stages of the runner design, as it provides the swirling flow configuration at runner outlet without actually computing the runner. By optimizing the parameterized swirl-free velocity profile one can achieve through the inverse design approaches the most suitable runner blades configuration at the trailing edge.

© 2011 Elsevier Inc. All rights reserved.

1. Introduction

Modern hydraulic turbines meet new challenges associated with the variable demand on the energy market as well as limited energy storage capabilities, resulting in great flexibility required in operation. Quite often turbines tend to be operated over an extended range of regimes far from the best efficiency point. In particular, Francis turbines, which have a fixed pitch runner, experience an abrupt decrease in efficiency and severe pressure fluctuations at off-design operating regimes. In

Nomenclature

Notation definition
$Q[\mathrm{m}^3/\mathrm{s}]$, $\phi[-]$ volumetric turbine discharge and dimensionless discharge coefficient
$H[m]$, $\psi[-]$ turbine head and dimensionless specific energy coefficient
$\eta[-]$ hydraulic efficiency
$\rho[\mathrm{kg/m}^3]$ liquid density
$\Omega[\mathrm{rad/s}]$ runner angular speed
$R[m]$, $r[-]$ radius, dimensional and dimensionless
$y[-]$ dimensionless radius squared
$V[\mathrm{m/s}]$, $v[-]$ velocity, dimensional and dimensionless
$P[\mathrm{Pa}]$, $p[-]$ pressure, dimensional and dimensionless
$\alpha[\mathrm{rad}]$, $\beta[\mathrm{rad}]$ absolute and relative flow angles, respectively
$M[\mathrm{kg\,m}^2/\mathrm{s}^3]$, $m[-]$ flux of moment of momentum, dimensional and dimensionless

Index	definition
ref	reference section at runner outlet
sf	swirl-free
z, r, θ	axial, radial, and circumferential, respectively
w	wall
s	stagnation
★	reference operating regime
1, 2	upstream/downstream the runner cross-sections

his review of confined vortices in flow machinery Escudier [1] noticed that the when hydraulic turbines operate at partial load a high level of residual swirl in the draft tube results from a mismatch between the swirl generated by the wicket gates (guidevanes) and the angular momentum extracted by the turbine runner. The vortex breakdown associated with this high level swirl, and in particular helical vortex breakdown, is seen as the source of flow unsteadiness and associated pressure fluctuations.

Evaluation of the turbine efficiency for the whole range of admissible discharge and head was, and still is, the standard experimental investigation on model turbines in order to predict the performances of the real size machine. The resulting efficiency "hill chart" usually displays a peek efficiency at the so-called "best efficiency point" (BEP). For the past decade, progress in computer algorithms, software and hardware made possible the numerical prediction of the hill-chart with reasonable accuracy, [2]. In addition, numerical investigation of the flow on the complete Francis turbine allows the analysis of the hydraulic losses on (i) spiral casing, (ii) guide vanes, (iii) runner, and (iv) draft tube, respectively. As shown by Vu and Retieb [2], the hydraulic losses in the first three segments of the turbine hydraulic passage have a rather modest variation with the operation regime. This is mainly the result of the significant progress in turbine design over the past decades. On the other hand, the draft tube which is the machine component where the flow exiting the runner is decelerated, thereby converting the excess of kinetic energy into static pressure, displays an abrupt increase in hydraulic losses as the operating regime departs from the BEP. Practically, for modern Francis turbines the shape of the hill-chart is dictated by the losses in the draft tube. As a result it is not surprising that a lot of research efforts are devoted now to the draft tube hydrodynamics.

The FLINDT (Flow Investigation in Draft Tubes) project [3] was aimed at extensive, state of the art, experimental investigations of both velocity and pressure fields in the draft tube of hydraulic turbines. In the case of machine rehabilitation of an existing power plant, mostly only the runner and the guide vanes are currently modified. For economical and safety reasons, the spiral casing and the draft tube are seldom redesigned. However, it is still a challenge to determine the optimum flow distribution at the runner outlet which leads to the best overall performance of the machine, including efficiency, power output and smooth regime for an extended operating range. The swirling flow at runner outlet measured in the first phase of the FLINDT project has been analyzed by Susan-Resiga et al. [4] who discovered that the axial and circumferential velocity profiles can be simultaneously represented as a superposition of three vortices: (i) a rigid body rotation with constant axial velocity, (ii) a counter-rotating Batchelor vortex with large characteristic radius, and (iii) a co-rotating Batchelor vortex with small characteristic radius. The last vortex is associated with the wake of the runner hub (also called crown), while the other two vortices are the direct outcome of the runner design. The stability analysis of this swirling flow [4] showed that the flow experiences a transition from supercritical to subcritical, according to the terminology introduced by Benjamin [5], as the discharge decreases, and this transition was shown to correspond to the discharge value where the pressure recovery in the draft tube suffers an abrupt change. When this phenomenon occurs in the neighborhood of the BEP, as it was the case for the Francis turbine investigated in the FLINDT project, obviously the machine operation is hindered. This sudden change in the draft tube performance as the turbine discharge is varied was also correlated by Mauri et al. [6] with the numerically

found Werlé-Legendre flow separation on the draft tube wall. It was clear from these investigations that the swirling flow ingested by the draft tube is the key issue in both minimizing the draft tube losses and avoiding unexpected hydrodynamic effects, respectively. While successful in analyzing the swirling flow at runner outlet, our approach [4], further extended for the draft tube cone [7], lacks the capability of predicting the swirl configuration over a wide operating range. In particular, at low discharge conditions investigated in the second phase of the FLINDT project, where a precessing helical vortex is developed in the draft tube cone as a result of the self-induced swirl instability, also called helical vortex breakdown [8], with associated hydro-acoustic pressure waves [9], the three-vortex model from [4] fails to predict the circumferentially-averaged annular swirling flow with central quasi-stagnant region. However, we were able to compute this particular swirling flow in the draft tube cone [10], using axisymmetric turbulent swirling flow models, in good agreement with experimental data. We have used the Realizable $k - \epsilon$ turbulence model (RKE) in our axisymmetric flow simulations [10,7], but also the Reynolds-Stress model (RSM) or the renormalization group (RNG) $k - \epsilon$ model [11] are valid choices.

Predicting and understanding the swirling flow particularities at the runner outlet/draft tube inlet is also the key in developing novel flow control techniques aimed at mitigating the unwanted flow instabilities at partial discharge. Susan-Resiga et al. [12] propose a water jet injection from the runner crown, along the machine axis, and show that this method successfully mitigates the precessing helical vortex and the associated pressure fluctuations. This method was also confirmed by Zhang et al. [13] who also approximate the swirl in the draft tube cone with a Batchelor vortex in order to correlate the vortex rope occurrence with previous studies on the global instability of the swirling flow.

Most of the studies on draft tube hydrodynamics rely on velocity data at the draft tube inlet obtained either by direct measurements [6,8] or by computing the flow in the turbine runner [14,15]. It is clear however that the swirling flow ingested by the draft tube is directly related to the runner blades geometry in the neighborhood of the trailing edge. The state of the art in Francis turbine design half a century ago is well exemplified by Bovet [16]. With respect to the flow at Francis runner outlet, Bovet mentioned that the designer's choice for the absolute circumferential velocity is practically arbitrary. Following the argument in [16] one should keep in mind that the kinetic energy associated with the circumferential velocity downstream the runner cannot be recovered in the turbine diffuser (draft tube) and as a result it should be considered as a hydraulic loss. It follows that the runner should be designed with vanishing flow rotation at outlet. However, it is recommended to leave a small flow rotation at runner outlet in order to improve the flow in the draft tube cone. Without inlet rotation, the decelerated flow in the conical diffuser downstream the runner may have large hydraulic losses due to the flow detachment at the cone wall. This is particularly true for modern compact discharge cones with rather large cone angle. The benefits of inlet swirl on pressure recovery in conical diffusers has been well documented by Fox et al. [17]. As a result, Bovet [16] recommended to leave a small circumferential velocity component when designing the runner, arguing that the losses associated with this excess in outlet kinetic energy is more than compensated by the improvement in the draft tube performance. In quantitative terms, Bovet introduced the somehow arbitrary rule of choosing the magnitude of the relative velocity W equal to the transport velocity U on a mid streamline. Once the discharge velocity component is given at the design operating point, the above condition allows the computation of absolute circumferential velocity from the velocity triangle. Other choices for the runner design are detailed by Anton [18, Ch. 8]. Since a rigorous theory for choosing and optimizing the swirling flow at Francis runner outlet is still lacking, we attempt such a development in this paper.

The modern approaches use fully three-dimensional inverse design methods for turbomachinery blades, [19]. In this method the distribution of the *radius × circumferential velocity* on the meridional geometry of the runner is prescribed and the corresponding blade shape is computed iteratively. For a Francis hydraulic turbine the design data upstream the runner are relatively easy to prescribe for the flow exiting the guide vanes. However, downstream the runner we still need a systematic approach to determine the best swirling flow configuration such that the turbine will have high efficiency and smooth operation over an extended range. The real challenge is to determine the best choice of the flow at runner outlet before actually designing and analyzing the runner. It is this challenge we address in the present paper.

If one attempts to use the large body of literature devoted to swirling flows and vortex breakdown phenomenon for hydraulic turbines design, the main difficulty is that most of the papers consider theoretical swirl configurations associated with a one parameter Batchelor vortex, [20], or two-parameter vortex [21]. Even if using such simple analytical vortex representations may be useful in analyzing and understanding measured [4] or computed [13] turbine swirling flows, it is clear that we need an approach to actually construct the swirling flow configurations encountered in hydraulic turbines at runner outlet, if possible without computing the runner flow.

The paper is organized as follows. In Section 2 we introduce a simple model for analyzing the turbine operation over the full intended range. The main result of this model is the relationship between the flux of moment of momentum at runner outlet as function of turbine's discharge and head. Section 3 analyzes the kinematic constrained imposed on the swirling flow by the fixed-pitch runner blades. In doing so, we introduce the swirl-free velocity profile and show that it has a simple shape, practically independent on the operating regime. The main result of the paper is given in Section 4, where we present the constrained variational problem for the swirling flow at runner outlet. The numerical approximation for the unknown axial velocity profile is developed in Section 5, where we show that a Fourier–Bessel series automatically preserves the turbine discharge. The numerical approach for solving the variational problem is underlined in Section 6, where we also present a set of numerical results and validation against experimental data for axial and circumferential velocity profiles. The agreement between our model predictions and experimental data, in the framework of model simplified assumptions, is discussed in Section 7. The paper conclusions are summarized in the last section.

2. Francis turbine operation at variable regimes

The analysis of the hydraulic turbine operation at variable regimes starts with the fundamental equation of turbomachines, written for a hydraulic turbine as

$$\eta(\rho Q)(gH) = \underbrace{\int_{S_1} (\Omega R V_{1\theta})\rho V_{1r}\mathrm{d}S_1}_{M_1} - \underbrace{\int_{S_2} (\Omega R V_{2\theta})\rho V_{2z}\mathrm{d}S_2}_{M_2} . \tag{1}$$

In the left-hand side of Eq. (1) we have the hydraulic power written as the product of the mass flow rate ρQ and specific energy gH, multiplied by the hydraulic efficiency η. In the right-hand side of Eq. (1) we have the rate at which the fluid does work on the rotor, which by Newton's second law applied to the moment of forces is equal to the difference in the flux of moment of momentum between cross-sections upstream the runner, S_1, and downstream the runner, S_2, respectively. Figs. 1 and 2 show that S_1 is a cylindrical cross-section located at the outlet of the guide vanes, while S_2 is a plane normal to the machine axis located just downstream the runner outlet. Obviously, when computing the flux of moment of momentum upstream the runner, M_1, we use the discharge velocity V_{1r}, while for M_2 the discharge velocity is V_{2z}. The circumferential velocity uspstream the runner is $V_{1\theta}$, while downstream the runner we have $V_{2\theta}$.

The above equation can be written in dimensionless form by introducing the following coefficients:

$$\phi \equiv \frac{\rho Q}{\rho(\Omega R_{\mathrm{ref}})\pi R^2_{\mathrm{ref}}} \quad \text{discharge coefficient,} \tag{2a}$$

$$\psi \equiv \frac{gH}{(\Omega R_{\mathrm{ref}})^2/2} \quad \text{energy coefficient,} \tag{2b}$$

$$m \equiv \frac{M}{\rho(\Omega R_{\mathrm{ref}})^3\pi R^2_{\mathrm{ref}}} \quad \text{flux of moment of momentum coefficient.} \tag{2c}$$

The reference radius R_{ref} is the runner outlet radius, as shown in Fig. 1. We can rewrite now Eq. (1) in the simple dimensionless form:

$$\eta\phi\frac{\psi}{2} = m_1 - m_2. \tag{3}$$

A turbine operating regime is defined by the turbine discharge and specific energy, i.e. by the pair (ϕ,ψ). For the preliminary design of a hydraulic turbine, the hydraulic efficiency can be considered from an estimated hill-chart $\eta(\phi,\psi)$. Our goal for the present investigation is to evaluate the flux of moment of momentum downstream the runner,
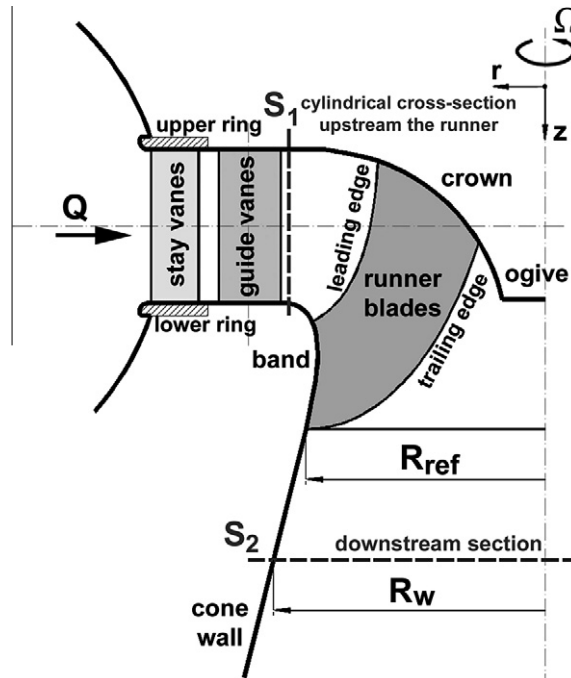

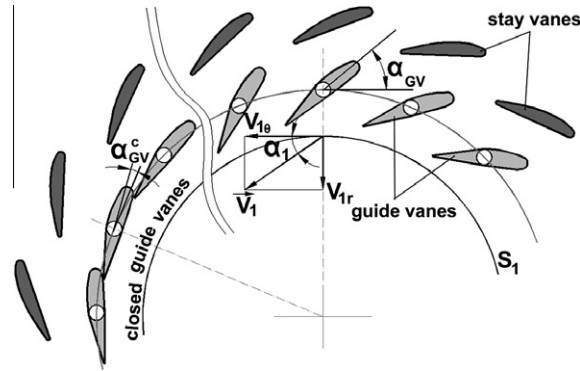**Fig. 1.** Meridian cross-section of a Francis turbine.

Fig. 2. Flow angle α_1 at distributor outlet/runner inlet.

$$m_2(\phi, \psi) = m_1(\phi, \psi) - \eta\phi\frac{\psi}{2}. \tag{4}$$

In order to use Eq. (4) we need to build an approximation for $m_1(\phi, \psi)$ taking into account that the turbine discharge is modified by opening or closing the guide vanes, Fig. 2.

In our simplified model we consider an averaged velocity at guide vanes outlet, with the magnitude V_1 and the flow angle α_1 with respect to the tangential direction. Note that α_1 is not the same as the guide vane opening angle α_{GV}, but a correlation can be found by solving for the flow in the two circular cascades corresponding the both stay vanes and guide vanes. The velocity magnitude should depend on the turbine head as $V_1 \sim \sqrt{\eta g H}$. On the other hand, the discharge is proportional to the radial velocity component, $Q \sim V_{1r} = V_1\sin\alpha_1$. The moment of momentum flux should be proportional to the product of radial and circumferential velocity components, $M_1 \sim V_{1r}V_{1\theta} = V_1^2 \sin\alpha_1\cos\alpha_1$. These considerations should be viewed as first approximations to be used for the preliminary design stages.

If we consider a reference operating point (e.g. the design operating point, or the best efficiency point for an existing runner), further denoted by $(\phi^\star, \psi^\star)$, the above considerations lead to

$$\frac{\phi}{\phi^\star} = \sqrt{\frac{\eta\psi}{\eta^\star\psi^\star}}\frac{\sin\alpha_1}{\sin\alpha_1^\star}, \tag{5a}$$

$$\frac{m_1}{m_1^\star} = \frac{\eta\psi}{\eta^\star\psi^\star}\frac{\sin 2\alpha_1}{\sin 2\alpha_1^\star}. \tag{5b}$$

Given an arbitrary operating point (ϕ, ψ), Eqs. (5) form a system of two algebraic equations with the unknowns m_1 and α_1. Note that at the reference operating point $(\phi^\star, \psi^\star)$ we assume $\eta^\star, \alpha_1^\star$, and $m_1^\star$ as known quantities. With m_1 computed by solving Eqs. (5) we can find from Eq. (4) the flux of moment of momentum downstream the runner at any operating point.

In order to validate this mathematical model we consider several operating regimes for a Francis model turbine, where both axial and circumferential velocity profiles have been measured in a survey section just downstream the runner, S_2 section in Fig. 1, using Laser Doppler Velocimetry, [4,10]. Using the experimental data for the axial and circumferential velocity components, shown in Section 6 of this paper, we have computed the turbine discharge and the flux of moment of momentum as follows:

$$Q = \int_0^{R_w} V_{2z}2\pi R dR, \tag{6a}$$

$$M_2 = \int_0^{R_w} (\Omega R V_{2\theta})\rho V_{2z}2\pi R dR, \tag{6b}$$

where R_w is the wall radius in section S_2.

By introducing the dimensionless velocity $v \equiv V/(\Omega R_{ref})$ and the dimensionless radius $r \equiv R/R_{ref}$, respectively, Eqs. (6) can be written in dimensionless form using the definitions (2a) and (2c),

$$\phi = \int_0^{r_w} v_{2z}2r dr, \tag{7a}$$

$$m_2 = \int_0^{r_w} (r v_{2\theta}) v_{2z}2r dr. \tag{7b}$$

The integrals in (7a) and (7b) are computed for the data shown in Fig. 6 using a simple trapezoidal rule, and the corresponding values are given in Table 1.

Table 1
Experimental data for operating regimes with variable discharge ϕ and constant specific energy ψ = 1.18.

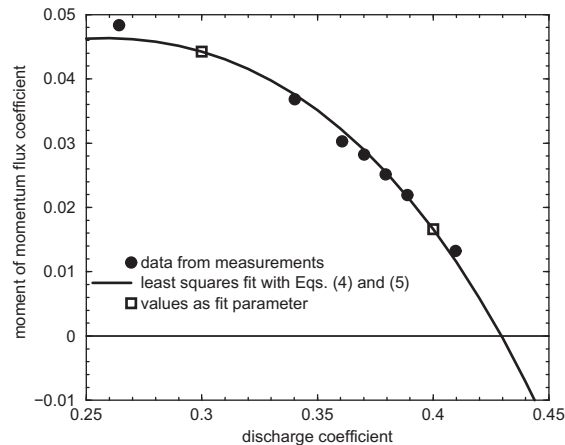| Relative turbine discharge	Discharge coefficient ϕ	Moment of momentum flux coefficient m_2
$Q = 0.714\ Q_{BEP}$	0.26428	0.048341
$Q = 0.919\ Q_{BEP}$	0.34015	0.036829
$Q = 0.974\ Q_{BEP}$	0.36066	0.030264
$Q = Q_{BEP}$	0.37014	0.028227
$Q = 1.025\ Q_{BEP}$	0.37950	0.025154
$Q = 1.050\ Q_{BEP}$	0.38881	0.021944
$Q = 1.107\ Q_{BEP}$	0.40976	0.013239

Fig. 3. Dimensionless flux of moment of momentum downstream the runner, m_2, versus the discharge coefficient, ϕ.

Six of the operating points in Table 1 are clustered within ± 10% the discharge at the best efficiency point, while the point at 0.7 Q_{BEP} corresponds to the partial discharge regime with well-defined precessing vortex rope. The data from Table 1 are shown with filled circles in Fig. 3, where the solid line corresponds to the least squares fit using Eqs. (4) and (5). All data points correspond to the constant energy coefficient $\psi^\star$ = 1.18. The reference discharge coefficient $\phi^\star$ can be arbitrary chosen and it does not have to coincide with a data point. For example, by choosing $\phi^\star$ = 0.3 the fit parameters obtained with the IMSL [22] routine RNLIN are $m_2^\star = 0.044232$ and $\alpha_1^\star = 30.348°$, respectively. When choosing $\phi^\star$ = 0.4 the fit parameters are $m_2^\star = 0.016612$ and $\alpha_1^\star = 42.351°$, respectively. However, the fit curve is unchanged with the two points $m_2^\star(\phi^\star)$ on the curve, as shown in Fig. 3 with squares. We conclude that the least squares fit procedure based on Eqs. (4) and (5) is robust in the sense that the fit curve does not depend, as expected, on the choice of the reference discharge $\phi^\star$.

One can see that the simple mathematical model introduced in this section is in quite good agreement with the experimental data. No data were available to check the model for variable head, but it is clear that the model captures correctly the qualitative behavior of the residual flux of moment of momentum downstream the runner as the turbine is operated within a wide range. Moreover, this model is not intended for analyzing the turbine swirling flow. Instead, our model provides valuable information in the early design and optimization stages for Francis runners. In particular, the model provides the two main integral quantities defining the swirling flow downstream the runner, i.e. the discharge ϕ and the flux of moment of momentum m_2, respectively, for the whole intended operating range of the turbine.

3. Swirling flow kinematics at Francis runner outlet

For turbine runners with fixed pitch blades, such as Francis runners, the swirling flow at the runner outlet must satisfy the kinematic constraints given by the runner blades geometry close to the trailing edge.

The well-known velocity triangle, shown in Fig. 4, provides the kinematic constraint corresponding to the relative flow angle β_2. Note that β_2 is not the blade angle at the trailing edge. Moreover, β_2 is changing along the radius, corresponding to the blade geometry from hub to shroud. For the present simplified model we assume that β_2 depends only on the radius for the section S_2 at runner outlet. In doing so, we consider that this β_2 radial variation is not changing with the operating point. This assumption is acceptable for Francis turbines, where the large number of blades provide a good guidance of the flow with minimal three-dimensional effects in the inter-blade channel. However, it is clear that the relative flow angle β_2
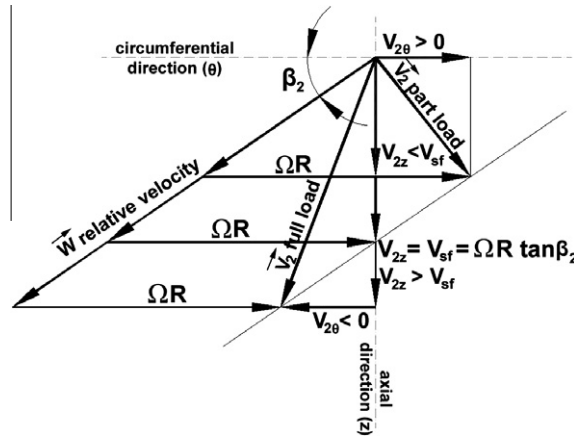
Fig. 4. Velocity triangle downstream the runner, for variable operating regimes.

changes with the operating point even for inviscid flows, but here we assume that such variations could be neglected in a first approximation.

Fig. 4 shows three particular configurations of the velocity triangle, with the relative velocity kept on the same direction given by β_2. Also, the transport velocity ΩR remains the same for all three cases further examined. At low discharge, corresponding to turbine's part-load regimes, the absolute circumferential velocity $V_{2\theta}$ has the same direction as the transport velocity, and the swirling flow co-rotates with respect to the runner. At large discharge, corresponding to turbine's full-load operating regimes, $V_{2\theta}$ is in opposite direction with the transport velocity, and the swirl counter-rotates with respect to the runner. In-between we can always identify a regime where the absolute circumferential velocity vanishes, i.e. $V_{2\theta} = 0$. We call the corresponding axial velocity the "swirl-free velocity", V_{sf}. Since the relative flow angle is directly related to the swirl-free velocity as $\tan\beta_2 = V_{sf}/(\Omega R)$, we can use the V_{sf} instead of β_2 to describe the kinematical flow constraint at runner outlet. For an arbitrary operating regime we have,

$$\frac{V_{2z}}{\Omega R - V_{2\theta}} = \tan \beta_2 = \frac{V_{sf}}{\Omega R}, \tag{8}$$

thus the swirl free-velocity can be written as

$$V_{sf} = \frac{\Omega R V_{2z}}{\Omega R - V_{2\theta}}, \quad \text{or in dimensionless form} \quad v_{sf} = \frac{r v_{2z}}{r - v_{2\theta}}, \tag{9}$$

with dimensionless radius and velocity defined as $r \equiv R/R_{ref}$ and $v \equiv V/(\Omega R_{ref})$, respectively. Once the swirl-free velocity profile is known, $v_{sf}(r)$, the circumferential velocity follows from the axial velocity profile as

$$v_{2\theta} = r\left(1 - \frac{v_{2z}}{v_{sf}}\right). \tag{10}$$

Eq. (10) shows that at part load, i.e. $v_{2z} < v_{sf}$, we have $v_{2\theta} > 0$ with co-rotating swirl, while at full-load, $v_{2z} > v_{sf}$, we have counter-rotating swirl with $v_{2\theta} < 0$.

The concept of swirl-free velocity has been employed by Kubota et al. [23] who investigate the draft tube losses for the GAMM model Francis turbine, and in particular the influence of the swirl intensity of runner outflow for variable operating points given by the discharge and specific energy coefficients. When analyzing the swirl velocity at runner outlet, they assume a constant runner outflow angle and express a representative circumferential velocity $V_{2\theta}$ using the transport velocity $U_2 = \Omega R$, the swirl-free discharge coefficient ϕ_{sf}, and the discharge coefficient value ϕ corresponding to the operating point, as $V_{2\theta} = U_2(1 - \phi/\phi_{sf})$. Both $V_{2\theta}$ and U_2 are considered by Kubota et al. [23] on a representative mid-streamline at runner outlet, corresponding to a radius of 0.1394 m while the runner outlet radius is 0.200 m. This rather crude evaluation does not account for the axial and circumferential velocity profiles, and obviously it does not describe the evolution of the swirling flow configuration when changing the operating point. However, it introduces the idea of the swirl-free meridian velocity to replace the relative flow angle.

In this paper we develop the swirl-free concept, but instead of using a single value corresponding to an arbitrary chosen streamline we introduce a swirl-free velocity profile at runner outlet. Moreover, we argue that this is an essential ingredient for the runner design and optimization within a range of operating regimes.

The main hypothesis concerning the swirl-free velocity profile introduced above as an alternative to the relative flow angle at runner outlet is that $v_{sf}(r)$ is practically unchanged as the operating regime spans the whole operating range of the turbine. Fig. 5 shows with filled circles the v_{sf} values computed with Eq. (9) from the experimental data for axial and circumferential velocities measured at the operating points indicated in Table 1. It can be seen that the experimental points are
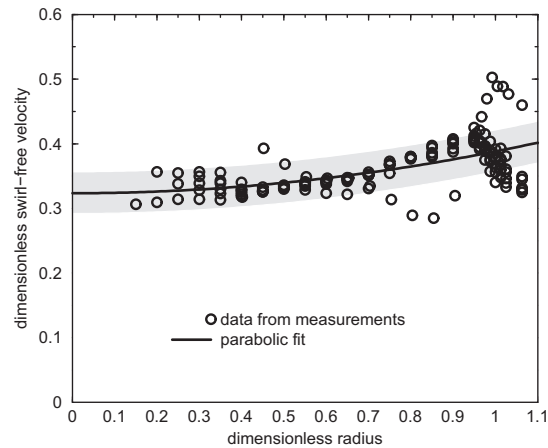
Fig. 5. The swirl-free velocity profile at a Francis runner model outlet.

reasonably clustered around the parabolic fit $v_{sf}(r) = 0.323505 + 0.0646465r^2$, with a standard deviation for the errors of 0.03136 as shown with the grey strip in Fig. 5. We postulate that an expression of the form $v_{sf}(r) = a + b\,r^2$ can be employed for optimizing the swirling flow downstream the Francis runner, with a and b as optimization parameters, as an alternative to consider the relative flow angle β_2 at runner outlet. The optimization of $v_{sf}(r)$ should be performed mainly to minimize the weighted hydraulic losses in the turbine draft tube, or at least with respect to the losses in the draft tube cone.

4. Variational formulation for swirling flow at Francis runner outlet

In Section 2 we have shown that the swirling flow downstream the Francis turbine runner is characterized by two integral quantities: the discharge coefficient and the flux of moment of momentum coefficient. In addition, this swirling flow satisfies a kinematic constraint corresponding to the runner blade geometry, described in Section 3 by the swirl-free velocity profile. The swirling flow exiting the runner is further decelerated by the draft tube in order to convert the excess of kinetic energy into static pressure, thus reducing the overall losses in the hydraulic turbine. However, in order to evaluate the hydraulic losses in the draft tube, generated by both swirl deceleration and change in the overall flow direction one needs to know the axial and circumferential velocity profile at the draft tube inlet for the whole operating range of the turbine.

From now on, for the rest of the paper we will refer only to the swirling flow at the runner outlet S_2, thus we will drop the index 2 in order to simplify the notations.

In order to find the swirling flow configuration we will consider a simplified swirling flow model corresponding to steady, axisymmetric, incompressible and inviscid swirling flow. In this case, the Euler equations reduce to the Bragg–Hawthorne equation [24] for the stream-function. The symmetry investigations of the Bragg–Hawthorne equation led Frewer et al. [25] to the conclusion that it possesses additional symmetries not being admitted by the original Euler equations. As a result, it appears that not the Euler equations but rather a set of integro-differential equations attains full equivalence to the Bragg–Hawthorne equation. A particularity of the Bragg–Hawthorne equation is that it includes two arbitrary functions, circulation and total specific energy, which depends only on the stream function by Kelvin's and Bernoulli's theorems, respectively. For the problem examined in this paper, the information available for the swirling flow downstream the Francis turbine runner does not allow the determination of the two generating functions in the Bragg–Hawthorne equation.

The Bragg–Hawthorne equation became the mathematical foundation for the throughflow theory of turbomachines. However, Oates et al. [26] introduced a variational formulation of the throughflow problem, leading to robust finite element algorithms. Their variational functional corresponds to the integral of the meridional momentum over all computational domain. The variational approach had been previously used by Benjamin [5] to explain the vortex breakdown phenomenon, where the functional was named "flow force". The variational formulation has been extended by Keller et al. [27] to allow variable lower endpoints, i.e. for cases when the flow occupies an annulus starting from a positive radius and going up to the wall. This approach has been further developed by Wang and Rusak [20] who explore both local and global minimizers of the variational functional for inviscid, incompressible and steady axisymmetric swirling flows to explain the dynamics of swirling flows in a pipe and transition to axisymmetric vortex breakdown.

Going back to the swirling flow at the Francis runner outlet, we consider that the flow is locally parallel (so-called columnar flow) due to the proximity to the turbine throat. Indeed, the radial velocity component close to the runner outlet is much smaller than either axial and circumferential velocities. Cervantes and Gustavsson [28] attempt to estimate the radial velocity in swirling flow at the draft tube inlet of a Kaplan turbine using the Bragg–Hawthorne equation (also known in literature as Long (1953)-Squire (1956) equation). However, we consider vanishing radial velocity at Francis runner outlet for the present simplified model. This assumption is also supported by experimental data of Tridon et al. [29].

The variational formulation for incompressible, inviscid, steady, columnar, swirling flow requires the minimization of the integral flow force,

$$F \equiv \int_0^{R_w} \left(\rho V_z^2 + P_w - P \right) 2\pi R dR, \tag{11}$$

where we have employed the pressure deficit with respect to the wall pressure, $P_w - P$ instead of the static pressure P. The corresponding dimensionless flow force and pressure are defined as

$$f \equiv \frac{F}{\rho(\Omega R_{ref})^2 \pi R_{ref}^2}, \tag{12a}$$

$$p \equiv \frac{P_w - P}{\rho(\Omega R_{ref})^2}. \tag{12b}$$

The dimensionless flow force can now be written as

$$f = \int_0^{y_w} \left(v_z^2 + p \right) dy, \tag{13}$$

where $y \equiv r^2$ being a modified radial coordinate.

The radial distribution of the pressure is correlated with the circumferential velocity through the radial equilibrium equation, i.e. the radial component of the axisymmetric Euler equation for vanishing radial velocity,

$$\frac{1}{\rho} \frac{dP}{dR} = \frac{V_\theta^2}{R}. \tag{14}$$

After integrating Eq. (14) and using Eq. (10) we obtain the dimensionless pressure,

$$p(y) = \frac{1}{2} \int_y^{y_w} \left(1 - \frac{v_z}{v_{sf}} \right)^2 dx. \tag{15}$$

Given the swirl-free velocity profile, for example $v_{sf}(y) = a + by$ as shown in Section 3, the functional f will depend only on the axial velocity profile $v_z(y)$ as follows:

$$f(v_z) = \int_0^{y_w} v_z^2 dy + \frac{1}{2} \int_0^{y_w} \int_y^{y_w} \left(1 - \frac{v_z}{v_{sf}} \right)^2 dx dy. \tag{16}$$

The minimization of functional $f(v_z)$ should be done with the integral constraints Eqs. (7), rewritten here as

$$\int_0^{y_w} v_z dy = \phi, \tag{17}$$

$$\int_0^{y_w} \left(1 - \frac{v_z}{v_{sf}} \right) v_z y dy = m, \tag{18}$$

where the values of ϕ and m depend on the operating regime as shown in Section 2. Once the axial velocity v_z is found by minimizing (16) subject to constraints (17) and (18), the circumferential velocity follows from Eq. (10).

When the turbine operates at low discharge, the swirling flow downstream the runner develops a self-induced instability leading to an unsteady precessing helical vortex, also known as vortex rope. A qualitative model of this particular flow-field was given by Nishi et al. [30] who observed a quasi-stagnant (stalled) central region with the spiral vortex core wrapped around it. Of course, the flow in the central region is highly fluctuating, but on average all velocity components vanish. The thin shear layer between the central stalled region and the main annular swirling flow becomes unstable, breaks-up and rolls-up in a helical vortex with precession. This model has been further confirmed by the measurements of axial and circumferential velocity profiles made in Francis turbines [8,31], numerical simulations [10], or analytical models [32]. In order to incorporate the stagnant region model into the present variational formulation we proceed as Keller et al. [27] and introduce an additional unknown in the problem, $y_s \equiv r_s^2$, where r_s is the radius of the central stagnant region. As a result, we re-formulate the variational problem corresponding to the swirling flow downstream the Francis turbine runner as follows:

Given the discharge coefficient, ϕ, the dimensionless flux of moment of momentum, m, the swirl-free velocity profile $v_{sf}(y)$ and the radial extent of the cross-section at runner outlet, y_w, find the axial velocity profile $v_z(y)$ and the stagnant region extent y_s that minimize the functional,

$$f(v_z, y_s) = \int_{y_s}^{y_w} v_z^2 dy + \frac{1}{2} \int_{y_s}^{y_w} \int_y^{y_w} \left(1 - \frac{v_z}{v_{sf}} \right)^2 dx dy, \tag{19}$$

subject to the integral constraints,

$$\int_{y_s}^{y_w} v_z \mathrm{d}y = \phi, \tag{20}$$

$$\int_{y_s}^{y_w} \left(1 - \frac{v_z}{v_{sf}}\right) v_z y \mathrm{d}y = m. \tag{21}$$

The problem (19)–(21) admits solutions with jump in v_z at $y_s > 0$, in contrast to the solutions with central stagnant region obtained from Bragg–Hawthorne equation where $v_z(y_s) = 0$, [27]. This is consistent with the circumferentially averaged velocity field from the analytical solution for the helical vortex in a pipe of Alekseenko et al. [32].

5. Fourier–Bessel approximation of the axial velocity profile

In order to solve constrained variational problem (19)–(21) we consider a representation of the axial velocity profile at runner outlet, $v_z(r)$, in terms of a truncated Fourier–Bessel series, [33]

$$v_z(r) = v_0 + \sum_{i=1}^{N} v_i J_0\left(\lambda_i \frac{r}{r_w}\right) \tag{22}$$

where N is the finite number of modes and λ_i are the zeros of the J_1 Bessel function, i.e. the non-zero solutions of $J_1(\lambda_i) = 0$. These zeros are computed numerically and have the values $\lambda_1 = 3.831705970$, $\lambda_2 = 7.015586670$, $\lambda_3 = 10.17346814, \ldots$, with the asymptotic sequence $\lambda_n = (n + 1/4)\pi + \mathcal{O}(1/n)$. The Bessel functions in (22) are orthogonal,

$$\int_0^{r_w} J_0\left(\lambda_i \frac{r}{r_w}\right) J_0\left(\lambda_j \frac{r}{r_w}\right) r \mathrm{d}r = \begin{cases} 0 & \text{if } i \neq j \\ \frac{r_w^2}{2} J_0^2(\lambda_i) & \text{if } i = j \end{cases} \tag{23}$$

If we evaluate the discharge coefficient using Eq. (7a), we obtain

$$\phi = \int_0^{r_w} v_0 2r \mathrm{d}r + \sum_{i=1}^{N} v_i \int_0^{r_w} J_0\left(\lambda_i \frac{r}{r_w}\right) 2r \mathrm{d}r = v_0 r_w^2. \tag{24}$$

This result follows from the Bessel function property that

$$\int_0^{r_w} J_0\left(\lambda_i \frac{r}{r_w}\right) r \mathrm{d}r = 0, \quad i = 1, 2, \ldots \tag{25}$$

In other words, each mode $J_0(\lambda_i r/r_w)$ has a vanishing contribution to the discharge. As a result, by replacing v_0 with ϕ/r_w^2 the Fourier–Bessel approximation of the axial velocity will always satisfy the discharge constraint (20).

Since we have introduced the modified radial coordinate $y = r^2$, we can re-write the discharge preserving axial velocity profile as

$$v_z(y) = \frac{\phi}{y_w} + \sum_{i=1}^{N} v_i J_0\left(\lambda_i \sqrt{\frac{y}{y_w}}\right), \quad 0 \leqslant y \leqslant y_w. \tag{26}$$

When a stagnant region is present, i.e. $y_s \leqslant y \leqslant y_w$, with $y_s > 0$, each mode will have a non-zero contribution to the overall discharge as follows:

$$\int_{y_s}^{y_w} J_0\left(\lambda_i \sqrt{\frac{y}{y_w}}\right) \mathrm{d}y = -2 \frac{\sqrt{y_s y_w}}{\lambda_i} J_1\left(\lambda_i \sqrt{\frac{y_s}{y_w}}\right), \quad i = 1, 2, \ldots \tag{27}$$

Using Eq. (27) we can compute the discharge for the annular section $y_s \leqslant y \leqslant y_w$ as

$$\phi = \int_{y_s}^{y_w} v_z(y) \mathrm{d}y = v_0(y_w - y_s) - 2\sqrt{y_s y_w} \sum_{i=1}^{N} \frac{v_i}{\lambda_i} J_1\left(\lambda_i \sqrt{\frac{y_s}{y_w}}\right). \tag{28}$$

We can now write the discharge-preserving axial velocity representation as

$$v_z(y) = \frac{\phi}{y_w - y_s} + \frac{2\sqrt{y_s y_w}}{y_w - y_s} \sum_{i=1}^{N} \frac{v_i}{\lambda_i} J_1\left(\lambda_i \sqrt{\frac{y_s}{y_w}}\right) + \sum_{i=1}^{N} v_i J_0\left(\lambda_i \sqrt{\frac{y}{y_w}}\right), \quad y_s \leqslant y \leqslant y_w \tag{29}$$

Note that in this case the average discharge velocity $\phi/(y_w - y_s)$ should be corrected because the modes have no longer vanishing contributions to the overall discharge. Obviously, if y_s vanishes in Eq. (29) we recover Eq. (26).

6. Numerical method and results

With the Fourier–Bessel representation of the axial velocity profile, Eq. (29), the discharge constraint (20) is automatically satisfied and we have to minimize the functional (19), subject to the constraint (21), with respect to the unknowns y_s and v_i,
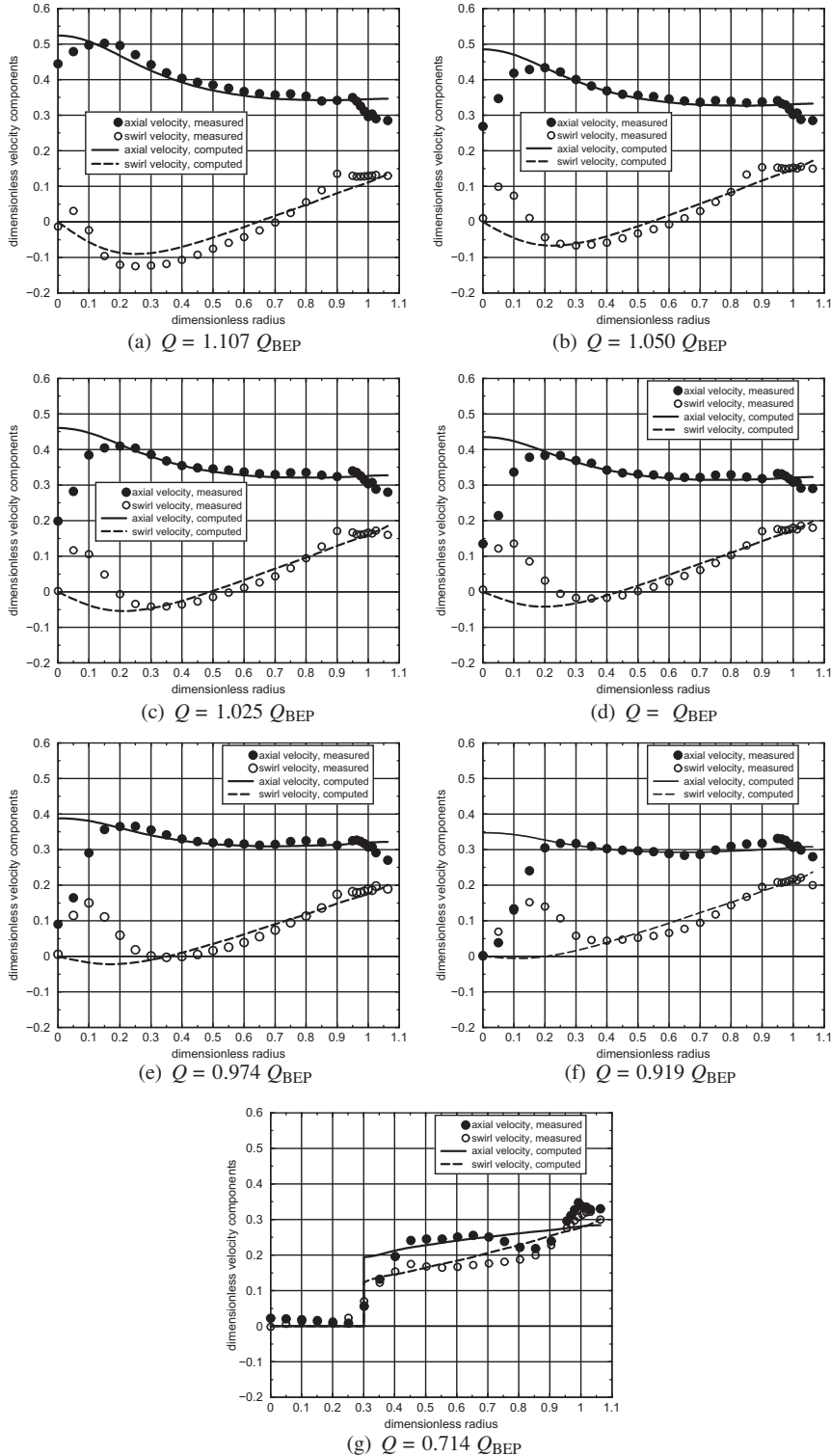

Fig. 6. Axial and circumferential velocity profiles at S_2 cross-section, Fig. 1.

$i = 1, 2,\dots N$. For the numerical results further presented in this section we have used $N = 9$, since the solution does not change anymore by adding Fourier–Bessel modes.

We have developed a computer code using the IMSL (International Mathematics and Statistics Library) FORTRAN numerical library, [22]. The constrained minimization problem (19), (21) is solved numerically with the IMSL routine NCONF which is based on subroutine NLPQL developed by Schittkowski [34]. It uses a successive quadratic programming method to solve the general nonlinear programming problem. The simple integrals are evaluated numerically using the QDAG subroutine which uses a globally adaptive scheme based on Gauss-Konrod rules, [35]. The two-dimensional integral in the functional (19) is computed with the TWODQ subroutine by iterated calls to QDAG. The Bessel functions are evaluated with BSJ0 and BSJ1, respectively. The zeros of the J_1 function are computed only once using Műller [36] method implemented by the ZREAL subroutine, with the initial guess $\lambda_n = (n + 1/4)\pi$.

The numerical results presented in this section are aimed at validating the mathematical model introduced in the previous sections. As a result, we examine the operating points presented in Table 1, with the swirl-free velocity profile $v_{sf}(y) = 0.323505 + 0.0646465y$ from Fig. 5.

Fig. 6 shows the measured and computed velocity profiles, for axial and circumferential velocity components, respectively. The experimental data were obtained within the FLINDT project phase 1 [3], Figs. 6(a)-(f), and phase 2 [8], Fig. 6(g), respectively. The velocity was measured with a two-component probe Laser Doppler Anemometry (LDA), using back-scattered light. The measuring point geometrical location is controlled within a 0.05 mm accuracy, and uncertainties in velocity measurements are estimated at 2% of the measured value [37]. The same data have also been used in our previous investigations [4,10,7]. The computed axial velocity profile is shown with solid lines in Fig. 6, and the circumferential velocity computed with Eq. (10) is represented with dashed lines. The dimensionless wall radius at S_2 is $r_w = 1.063$.

7. Discussion

Fig. 6 shows that our mathematical model correctly captures the swirling flow evolution as the turbine discharge is varied. At full load, $Q > Q_{BEP}$, one can see an increase of the axial velocity excess near the axis. On the other hand, at part load $Q < Q_{BEP}$ this velocity excess is gradually decreased until a stagnant region develops in the axis neighborhood.

The agreement with experimental data within the ±10% the best efficiency discharge Q_{BEP}, Figs. 6(a)-(f), is quite good except the wake of the crown which widens as the discharge decreases. This discrepancy is expected since our model does not account for the viscous effects which lead to the crown wake.

At low discharge, our model correctly captures the central stagnant region extent, Fig. 6(g), as well as the overall shape of the velocity components radial variation. The measured flow acceleration close to the wall is associated with the inter-blade vortex developed at the junction of the blade with the band [15, section 7.1]. Obviously, the present axisymmetric inviscid swirling flow model cannot capture the effects induced by such three-dimensional flow structures. The transition between the central stagnant region and the main annular swirling flow corresponds to the vortex sheet which evolves in the precessing helical vortex, [10]. In reality, the helical vortex has a finite core size and the corresponding circumferentially averaged flow displays a finite gradient in the stagnation - main flow transition zone, [38]. The swirl predicted by our simplified model corresponds to a thin vortex filament when the circumferentially averaged vortex sheet has vanishing thickness and a jump in the velocity.

Using the relationship between the flux of moment of momentum downstream the runner and the discharge, as shown in Fig. 3 for constant turbine head, we can examine the evolution at runner outlet for variable discharge. Fig. 7 shows the maps
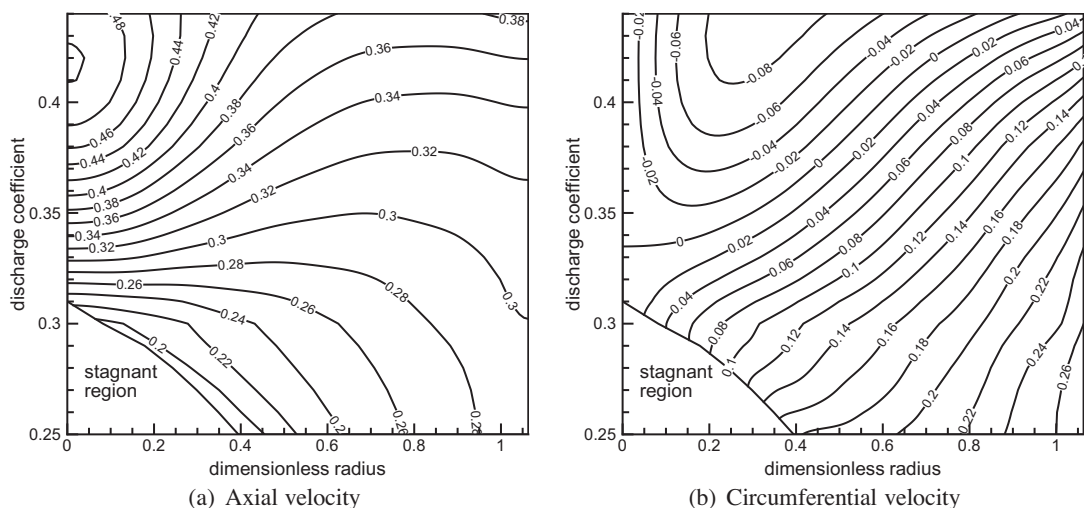

Fig. 7. Axial and circumferential velocity profiles for variable discharge coefficient $\phi = 0.25 \cdots 0.44$.

of axial and circumferential velocity components versus the radial coordinate and discharge. The radial profiles of the velocity components shown in Fig. 6 are horizontal slices of the 2D maps from Fig. 7. One can immediately identify the occurrence and development of the central stagnant region as the discharge decreases, as shown on the lower-left corner of the plots. Fig. 7(a) shows the excess in axial velocity at the axis for large discharge, and the graduate flow deceleration at the axis as the discharge decreases. However, our model predicts the development of the stagnant region before the axial velocity vanishes at the axis. Fig. 7(b) shows the development of the counter-rotation in the central region as the discharge increases, with the increase of the radius of vanishing circumferential velocity. For low discharge values the whole flow rotates in the same direction with the runner, and the circumferential velocity does not vanish at the stagnant region. In our opinion, it is this jump in both axial and circumferential velocity components at the stagnant region boundary, with a corresponding vortex sheet, which triggers the self-induced instabilities of the swirling flow and the development of the helical precessing vortex. It is clear that from the design point of view, the swirl-free velocity profile must be optimized such that the stagnant region shown in Fig. 7 be reduced and moved to lower values of the discharge.

8. Conclusions

We introduce a complete mathematical methodology for computing the swirling flow, i.e. radial profiles of axial and circumferential velocity components, respectively, at the runner outlet for Francis hydraulic turbines operated within the full admissible range. Since this methodology does not require the computation of the flow in the runner, it is suitable for early stages of turbine design and optimization.

Using the basic Euler equation of turbomachines, together with several considerations on the flow generated by the guide vanes of the turbine, we find a set of algebraic equations which allow the correlation between the flux of moment of momentum downstream the runner and the turbine operating regimes. As a result, given the turbine discharge and head, one can evaluate the level of swirl for the flow exiting the runner and further ingested by the draft tube.

For the fixed pitch runners, such as Francis hydraulic turbines, the swirling flow at runner outlet must satisfy a kinematic constraint usually given by the relative flow angle. However, we introduce in this paper the swirl-free velocity as a more suitable approach to describe the swirl kinematics at runner outlet. We show that the radial profile of the hypothetical swirl-free velocity at runner outlet is practically unchanged by the operating regime once three-dimensional and viscous effects of the flow in the inter-blade channels are neglected in the first approximation. The kinematic constraint on the swirl exiting the runner provides a simple relationship for computing the circumferential velocity once the radial profile of the axial velocity is known.

Several simplified assumptions are made on the swirl at runner outlet, consistent with the flow conditions in Francis turbines. We assume a steady, axisymmetric, parallel flow, of an inviscid and incompressible fluid. As a result, such swirling flow must minimize the so-called flow force, a functional introduced by Benjamin [5]. Using the kinematic constraint at runner outlet and the radial equilibrium equation, we express the flow force functional only with the axial velocity. Moreover, in agreement with the flow physics and experimental data, we modify the functional to allow the development of a central stagnant region. The radial profile of the axial velocity component is found by minimizing the flow force functional, while maintaining the overall discharge and flux of moment of momentum, resulting in a constrained variational problem. This is the core of the mathematical methodology introduced in this paper.

In order to solve numerically the variational problem we represent the unknown axial velocity as a truncated Fourier–Bessel series. We show that by suitably choosing the first coefficient in this series the overall discharge constraint is identically satisfied. As a result, the flow force functional must be minimized with respect to the set of mode coefficients in the Fourier–Bessel series and the additional unknown for the stagnant region radius, respectively, while satisfying only the constraint for the flux of moment of momentum. The resulting numerical algorithm is robust, most likely thanks to the Fourier–Bessel modes orthogonality.

The above mathematical methodology is validated against available experimental data for axial and circumferential velocity profiles measured at the runner outlet of a Francis model turbine for seven operating regimes. We show that our model correctly captures the swirling flow evolution with the variable operating regime of the Francis turbine. However, as expected the flow features associated with viscous effects, such as the runner hub wake, or three-dimensional effects, such as inter-blade vortices, cannot be captured within the simplified assumptions of our model.

Finally, let us summarize the main advantages and potential applications of the mathematical model introduced in this paper:

(i) The model allows the computation of the swirling flow, i.e. radial profiles of axial and circumferential velocity components, at the runner outlet of Francis turbines for any operating regime without any computation of the three-dimensional flow in the turbine.
(ii) The runner blades geometry at the trailing edge is embedded in the swirl-free velocity profile. The radial profile of the swirl-free velocity has a simple shape, and a simple two-parameter representation is quite suitable for optimizing the swirling flow ingested by the turbine's draft tube before designing the runner. This is essential for modern hydraulic turbines where the shape of the efficiency hill-chart is actually driven by the hydraulic losses in the draft tube.

(iii) The model is intended to be used in the early design and optimization stages of a new hydraulic turbine, or for refurbishment of existing turbines, as it allows the evaluation of a large number of operating regimes and design choices with very low computational costs.

(iv) Since the model correctly captures the development of the central stagnant region when operating the turbine far from the design operating regime, one can estimate in the early design stages the boundaries of the smooth operation range.

(v) Once an optimum swirling flow configuration at runner outlet is achieved by optimizing the swirl-free velocity in conjunction with the performances of the draft tube, the runner blades geometry follows through an inverse design approach.

Due to the simplified assumptions taken into account, the present model is recommended for *a priori* evaluation of design choices for hydraulic turbines, leaving the *a posteriori* evaluation to the current experimental protocols or to the full three-dimensional viscous flow computations.

Acknowledgements

References

[1] M. Escudier, Confined vortices in flow machinery, Annual Rev. Fluid Mech. 19 (1987) 27–52.
[2] T.C. Vu, S. Retieb, Accuracy assessment of current cfd tools to predict hydraulic turbine efficiency hill chart, in: Proceedings of the 21st IAHR Symposium on Hydraulic Machinery and Systems, volume 1, École Polytechnique Fédérale de Lausanne, Lausanne, Switzerland, 2002, pp. 193–198.
[3] F. Avellan, Flow investigation in a Francis draft tube: the FLINDT project, in: Proceedings of the 20th IAHR Symposium on Hydraulic Machinery and Systems, IAHR, Charlotte (NC), U.S.A., 2000. Paper DY-03.
[4] R. Susan-Resiga, G.D. Ciocan, I. Anton, F. Avellan, Analysis of the swirling flow downstream a Francis turbine runner, J. Fluids Eng. 128 (2006) 177–189.
[5] T.J. Benjamin, Theory of the vortex breakdown phenomenon, J. Fluid Mech. 14 (1962) 593–629.
[6] S. Mauri, J.L. Kueny, F. Avellan, Werlé-Legendre separation in a hydraulic machine draft tube, J. Fluid Eng. 126 (2004) 976–980.
[7] R. Susan-Resiga, S. Muntean, V. Hasmaţuchi, I. Anton, F. Avellan, Analysis and prevention of vortex breakdown in the simplified discharge cone of a francis turbine, J. Fluid Eng. 132 (2010) 15 pages. 051102.
[8] G.D. Ciocan, M.S. Iliescu, T.C. Vu, B. Nennemann, F. Avellan, Experimental study and numerical simulation of the FLINDT draft tube rotating vortex, J. Fluids Eng. 129 (2007) 146–158.
[9] J. Arpe, C. Nicolet, F. Avellan, Experimental evidence of hydroacoustic pressure waves in a Francis turbine elbow draft tube for low discharge conditions, J. Fluids Eng. 131 (2009) 9. Paper 081102.
[10] R. Susan-Resiga, S. Muntean, P. Stein, F. Avellan, Axisymmetric swirling flow simulation of the draft tube vortex in Francis turbines at partial discharge, Int. J. Fluid Mach. Sys. 2 (2009) 295–302.
[11] A. Escue, J. Cui, Comparison of turbulence models in simulating swirling pipe flows, Appl. Math. Model. 34 (2010) 2840–2849, doi:10.1016/j.apm.2009.12.018.
[12] R. Susan-Resiga, T.C. Vu, S. Muntean, G.D. Ciocan, B. Nennemann, Jet control of the draft tube vortex rope in francis turbines at partial discharge, in: Proceedings of the 23rd IAHR Symposium on Hydraulic Machinery and Systems, IAHR, Yokohama, Japan, 2006. Paper F192 (on CD-ROM).
[13] R.K. Zhang, J.Z. Wu, S.Y. Chen, Y.L. Wu, S.H. Liu, Characteristics and control of the draft-tube flow in part-load Francis turbine, J. Fluids Eng. 131 (2009) pp 13. Paper 021101.
[14] A. Ruprecht, T. Helmrich, T. Aschenbrenner, T. Scherer, Simulation of vortex rope in a turbine draft tube, in: Proceedings of the 21st IAHR Symposium on Hydraulic Machinery and Systems, volume 1, École Polytechnique Fédérale de Lausanne, Lausanne, Switzerland, 2002, pp. 259–266.
[15] P. Stein, Numerical Simulation and Investigation of Draft Tube Vortex Flow, Ph.D. thesis, Coventry University, 2007.
[16] M.T. Bovet, Contribution a l'étude du tracé d'aubage d'une turbine a réaction du type Francis, Technical Report 9, Information Techniques Charmilles, 1963.
[17] R.W. Fox, A.T. McDonald, R.W. Van Dewoestine, Effects of swirling inlet flow on pressure recovery in conical diffusers, AIAA J. 9 (1971) 2014–2018.
[18] I. Anton, Hydraulic Turbines, Ed. Facla, Timişoara, 1979, (in Romanian).
[19] M. Zangeneh, A compressible three-dimensional desigh method for radial and mixed flow turbomachinery blades, Int. J. Numer. Methods Fluids 13 (1991) 599–624.
[20] S. Wang, Z. Rusak, The dynamics of a swirling flow in a pipe and transition to axisymmetric vortex breakdown, J. Fluid Dyn. 340 (1997) 177–223.
[21] B. Leclaire, D. Sipp, A sensitivity study of vortex breakdown onset to upstream boundary conditions, J. Fluid Mech. 645 (2010) 81–119.
[22] IMSL MATH/LIBRARY: FORTRAN Subroutines for Mathematical Applications, Visual Numerics Inc., 1994.
[23] T. Kubota, F. Han, F. Avellan, Performance analysis of the draft tube for GAMM Francis turbine, in: E. Cabrera, V. Espert, F. Martinez (Eds.), Hydraulic Machinery and Cavitation, vol.1, Kluwer Academic Publishers, Dordrecht, The Netherlands, 1996, pp. 130–139.
[24] S.L. Bragg, W.R. Hawthorne, Some exact solutions of the flow through annular cascade actuator discs, J. Aero. Sci. 17 (1950) 243.
[25] M. Frewer, M. Oberlack, S. Guenter, Symmetry investigations on the incompressible stationary axisymmetric Euler equations with swirl, Fluid Dyn. Res. 39 (2007) 647–664.
[26] G.C. Oates, C.J. Knight, G.F. Carey, A variational formulation of the compressible throughflow problem, J. Eng. Power (1976) 1–8.
[27] J.J. Keller, W. Egli, J. Exley, Force- and loss-free transitions between flow states, J. Appl. Math. Phy. (ZAMP) 36 (1985) 854–889.
[28] M.J. Cervantes, H. Gustavsson, On the use of the Squire–Long equation to estimate radial velocities in swirling flows, J. Fluids Eng. 129 (2007) 209–217.
[29] S. Tridon, S. Barre, G.D. Ciocan, L. Tomas, Experimental analysis of the swirling flow in a francis turbine draft tube: Focus on radial velocity component determination, Euro. J. Mech. B/Fluids 29 (2010) 321–335.
[30] M. Nishi, S. Matsunaga, M. Okamoto, M. Uno, K. Nishitani, Measurement of three-dimensional periodic flow in a conical draft tube at surging condition, in: U.S. Rohatgi (Ed.), Flows in Non-Rotating Turbomachinery Components, FED, vol. 69, ASME, 1988, pp. 81–88.
[31] O. Kirschner, A. Ruprecht, Vortex rope measurement in a simplified draft tube, in: R. Susan-Resiga, S. Muntean, S. Bernad (Eds.), Proceedings 2nd IAHR International Meeting of the Workgroup on Cavitation and Dynamic Problems in Hydraulic Machinery and Systems, vol. 52, Transactions on Mechanics, Politehnica University of Timişoara of Scientific Bulletin, Romania, 2007, pp. 81–88.

[32] S.V. Alekseenko, P.A. Kuibin, V.L. Okulov, S.I. Shtork, Helical vortices in swirl flow, J. Fluid Mech. 382 (1999) 195–243.
[33] F. Bowman, Introduction to Bessel Functions, Dover Publications Inc.,, New York, 1958.
[34] K. Schittkowski, NLPQL: A FORTRAN subroutine solving constrained nonlinear programming problems, Ann. Oper. Res. 5 (1986) 485–500.
[35] R.E. Piessens, E. deDoncker Kapenga, C.W. Uberhuber, D.K. Kahaner, QUADPACK, Springer-Verlag, New York, 1983.
[36] D.E. Müller, A method for solving algebraic equations using an automatic computer, Math. Tables Aids Comput. 10 (1956) 208–215.
[37] G.D. Ciocan, F. Avellan, J.L. Kueny, Optical measurement techniques for experimental analysis of hydraulic turbines rotor-stator interaction in: Proceedings of the ASME 2000 Fluids Engineering Division Summer Meeting, ASME, Boston (MA), U.S.A., 2000, (Paper FEDSM2000-11056).
[38] P.A. Kuibin, V.L. Okulov, R. Susan-Resiga, S. Muntean, Validation of analytical formulae for predicting the vortex rope rotating frequency, in: Proceedings of the 25th IAHR Symposium on Hydraulic Machinery and Systems, vol. 12, Earth and Environmental Science of Institute of Physics Conference Series, IoP, <http://iopscience.iop.org/1755-1315/12/1/012051>, 2010, Paper 012051 (10 pp).

Alin Ilie Bosioc
Scientific Researcher
Center for Advanced Research
in Engineering Science,
Romanian Academy – Timisoara Branch,
Bvd. Mihai, Viteazu 24,
RO-300223, Timisoara, Romania
e-mail: alin@mh.mec.upt.ro

Romeo Susan-Resiga[1]
Professor
Hydraulic Machinery Department,
"Politehnica" University of Timisoara,
Romania, Bvd. Mihai Viteazu 1,
RO-300222, Timisoara, Romania
e-mail: resiga@mh.mec.upt.ro

Sebastian Muntean
Senior Researcher
Center for Advanced Research
in Engineering Science,
Romanian Academy – Timisoara Branch,
Bvd. Mihai Viteazu 24,
RO-300223, Timisoara, Romania
e-mail: seby@acad-tim.tm.edu.ro

Constantin Tanasa
Research Center for Engineering
of Systems with Complex Fluids,
"Politehnica" University of Timisoara,
Bvd. Mihai Viteazu 1,
RO-300222, Timisoara, Romania
e-mail: costel@mh.mec.upt.ro

Unsteady Pressure Analysis of a Swirling Flow With Vortex Rope and Axial Water Injection in a Discharge Cone

The variable demand of the energy market requires that hydraulic turbines operate at variable conditions, which includes regimes far from the best efficiency point. The vortex rope developed at partial discharges in the conical diffuser is responsible for large pressure pulsations, runner blades breakdowns and may lead to power swing phenomena. A novel method introduced by Resiga et al. (2006, "Jet Control of the Draft Tube in Francis Turbines at Partial Discharge," Proceedings of the 23rd IAHR Symposium on Hydraulic Machinery and Systems, Yokohama, Japan, Paper No. F192) injects an axial water jet from the runner crown downstream in the draft tube cone to mitigate the vortex rope and its consequences. A special test rig was developed at "Politehnica" University of Timisoara in order to investigate different flow control techniques. Consequently, a vortex rope similar to the one developed in a Francis turbine cone at 70% partial discharge is generated in the rig's test section. In order to investigate the new jet control method an auxiliary hydraulic circuit was designed in order to supply the jet. The experimental investigations presented in this paper are concerned with pressure measurements at the wall of the conical diffuser. The pressure fluctuations' Fourier spectra are analyzed in order to assess how the amplitude and dominating frequency are modified by the water injection. It is shown that the water jet injection significantly reduces both the amplitude and the frequency of pressure fluctuations, while improving the pressure recovery in the conical diffuser. [DOI: 10.1115/1.4007074]

Keywords: decelerated swirling flow, vortex rope, water injection method, unsteady pressure, experimental investigation

1 Introduction

The swirling flow emerging from a Francis turbine runner has a major influence in a draft tube cone downstream. It produces self-induced flow instabilities leading to pressure fluctuations and ultimately to the draft tube surge [1]. At part load operation it develops a precessing helical vortex (also known as vortex rope) in the Francis turbine draft tube cone. Consequently, the vortex rope generates pressure fluctuations, additional hydraulic losses, and power swing phenomena at the electrical generator [2]. Unsteady pressure measurements for hydraulic Francis turbines operating at part load have been performed on site by Wang et al. [3] and Baya et al. [4]. They reveal a low frequency oscillation (from 1/5 to 1/3 of the runner rotation frequency) associated with the vortex rope. Extensive unsteady wall pressure measurements in the elbow draft tube of the hydraulic Francis turbine model at partial discharge are performed by Arpe et al. [5]. The pressure waves' source was located near the inner part of the elbow draft tube based on experimental data. Moreover, these waves are propagated in all hydraulic systems. The synchronous nature of the pressure fluctuations and the pressure distribution along the draft tube suggests hydro acoustic resonance of the entire hydraulic system.

Different methods were proposed in order to mitigate the instabilities produced by the vortex rope. Examples include aerators mounted at the inlet of the cone, stabilizer fins or runner

cone extensions [6]. Numerical Francis turbine simulation of the flow was performed by Qian et al. [7] in order to investigate the air admission from the spindle hole. Analysis of the draft tube cone air admission showed that the amplitude and the pressure difference in the cross section of the draft tube decreases while the blade frequency pressure pulsation increases in front of the runner. Therefore, proper air discharge to mitigate the pressure pulsations in the draft tube cone of the hydraulic turbine should be chosen according to specific operating conditions. These methods lead to some improvements in reducing the pressure pulsations for a narrow regime but they are not effective or even increase the unwanted effects. Given by the energy injected in the draft tube cone these methods can be divided into active, passive or semipassive control. If an external energy source is used to mitigate or eliminate the vortex rope, the control is called active. Examples of active control include air injection either downstream (through runner cone) or upstream (through wicket gates trailing edge) of the runner [6,8], or tangential water jets at the discharge cone wall [9]. The control involving no additional energy to destroy the vortex rope is called passive. Passive control methods include fins mounted on the cone [10,11], extending cones mounted on the runner's crown [12] or using J-grooves [13].

Resiga et al. [14] proposed a new method in order to mitigate the vortex rope, axial water injected through the runner's crown along to the discharge cone. An experimental test rig was designed and developed in the Hydraulic Machinery Laboratory at "Politehnica" University of Timisoara in order to investigate this new method. The rig is used to determine the parameters of the swirling flow with vortex rope and the optimum water jet in order to mitigate the pressure fluctuations.

---

[1]Corresponding author.

This paper presents our experimental investigations of the swirling flow with vortex rope in order to assess the water injection method benefits. The second section presents the experimental test rig and the swirl apparatus used to generate the swirling flow in a conical diffuser similar to the draft tube cone of a Francis turbine. The third section presents the equipment used for pressure measurements and the results obtained. Pressure data are analyzed to determine the vortex rope amplitude and frequency corresponding to the self-induced instabilities of the decelerated swirling flow. Energetically, the pressure recovery coefficient in the draft tube cone is used to assess the efficiency of this method. The pressure pulsations are analyzed for the swirling flow with vortex rope as well as for the swirling flow with water injection in order to evaluate this method. The last section draws the conclusions.

2 Experimental Test Rig for Swirling Flows

Two different methods are usually employed to generate a swirling flow under the laboratory conditions: using a turbine model or a swirl generator. Using a turbine model is quite expensive. Alternatively, a swirl generator is a simpler solution allowing physical phenomena investigation. For the production of a swirling flow, Kurokawa et al. [13] used an axial flow impeller at about $3.3d$ upstream of the diffuser inlet, where $d (=156\,\text{mm})$ is the inlet pipe diameter. Kurokawa's rig employs an additional blower arranged at far upstream of the divergent channel to widely change the discharge. Another method to generate a swirling flow in a conical diffuser was proposed by Kirschner et al. [15]. The swirl generator is installed instead of the turbine in order to investigate different swirl conditions, and was built with adjustable guide vanes. A straight draft tube was mounted downstream. The cone angle is 2×8.6 deg, similar to the angle of a real draft tube cone.

Based on the large experience accumulated over the decades of design, the hydraulic losses are small in the spiral casing, in the wicket gates, and runner. However, the hydraulic losses still exhibit large variations during the full operating range. According to Vu and Retieb [16] in the case of Francis turbines, the largest fraction of the hydraulic loses is located in the draft tube except in the neighborhood of the best efficiency regime. When the turbine is operated far from the best efficiency point, its losses increase sharply with a corresponding decrease in overall efficiency. This is the reason why researchers focus their efforts to improve the draft tube cone flow.

An experimental test rig was developed to analyze the decelerated swirling flow in a conical diffuser and to evaluate the new water-injection control method. The main purpose of the rig is to reproduce the flow field specific to a conical diffuser with a decelerated swirling flow and the development of the vortex rope. The rig, developed in the Hydraulic Machinery Laboratory at the Politehnica University of Timisoara, is composed of the following main elements: (i) the main hydraulic circuit used to generate the decelerated swirling flow in the conical diffuser; (ii) the auxiliary hydraulic circuit needed to supply water for the jet control method. The main hydraulic circuit (shown in Fig. 1) is employed to generate a flow similar to the one encountered at a partial discharge operated Francis runner while the auxiliary circuit (shown in Fig. 1) is used to inject water in the conical diffuser's inlet through a nozzle.

The swirling flow apparatus is installed along the main hydraulic circuit and it contains two main parts: the swirl generator and the convergent-divergent test section [17]. The swirl generator has an upstream annular section with stationary and rotating blades for generating swirling flow. It has three components: the ogive, the guide vanes, and the free runner. The ogive with four leaned struts has the role to sustain the swirl generator and to deliver the jet water to the nozzle (it can be seen in Fig. 2). The guide vane and the free runner are mounted in the cylindrical section, $D_s = 0.15$ m. The swirl generator was designed to
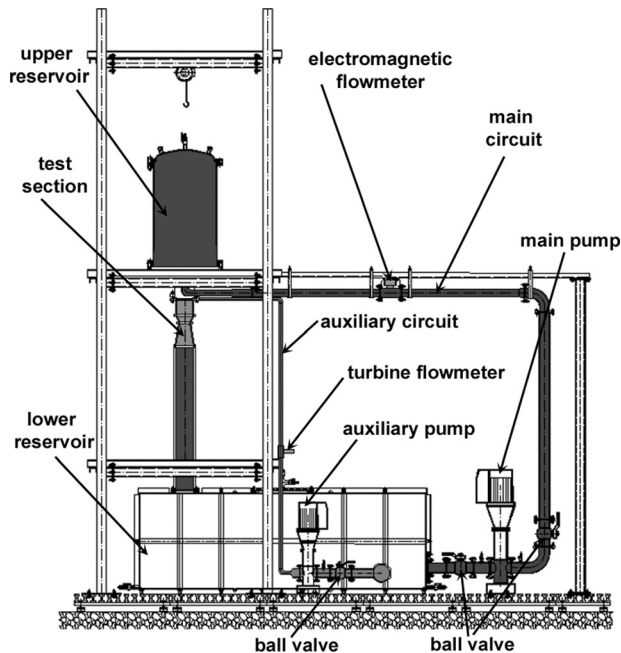

Fig. 1 Experimental closed loop test rig installed in the Hydraulic Machinery Laboratory. Sketch of the test rig with the main elements.

operate similar to a Francis turbine model at partial discharge [18,19]. This part load operating point was chosen at 70% because at this regime the vortex rope is well developed and generates the largest pressure pulsations [20]. The main part of the swirl generator is the free runner. Its main purpose is to redistribute the total pressure at the entrance. The free runner induces an excess of energy near the shroud and a deficit of energy near the hub. Therefore it acts as a turbine at the hub and as a pump at the shroud having a vanishing total torque. The swirl generator's hub and shroud diameters are $D_h = 0.09$ m and $D_s = 0.15$ m, respectively. The 10-bladed runner spins freely and ensures the designed output flow configuration. Teflon bearing was preferred as it ensures low friction. Supplied by the auxiliary hydraulic circuit (Fig. 1(a)), the injected water passes through the leaned struts of the ogive, the hub's interior and reaches the nozzle.

The inverse method [21] was used to design the runner and the guide vanes. The runner's exit velocity profiles resulting from the FLINDT project were imposed for design. These velocity profiles were measured by Ciocan et al. [22] and numerically determined by Stein et al. [23,24]. As a result, the axial and the swirl velocity profiles in the test section are quite similar to the ones measured downstream of the runner of a Francis turbine model according to Fig. 7 from Resiga and Muntean [25]. Note that this is the runaway speed for the swirl generator runner and it is not related to the turbine model runner speed. The dimensionless precession frequency of the vortex rope is expressed using the Strouhal number shown in Table 1. It can be seen that the swirl apparatus generates a vortex rope with Strouhal number equal to 0.39 quite close to the Strouhal number for the model Francis turbine (Sh = 0.408).

The vortex rope visualized in Fig. 3(a) was obtained using the above-described swirl. It can be seen that the vortex rope develops along the entire length of the cone. Having a spiral shape with a precession movement, it starts close to the injection nozzle and it disintegrates at the downstream exit having a total length of about 200 mm. When the jet is turned on, it pushes the stagnant region and the associated vortex rope downstream the cone, Fig. 3(b) [26].
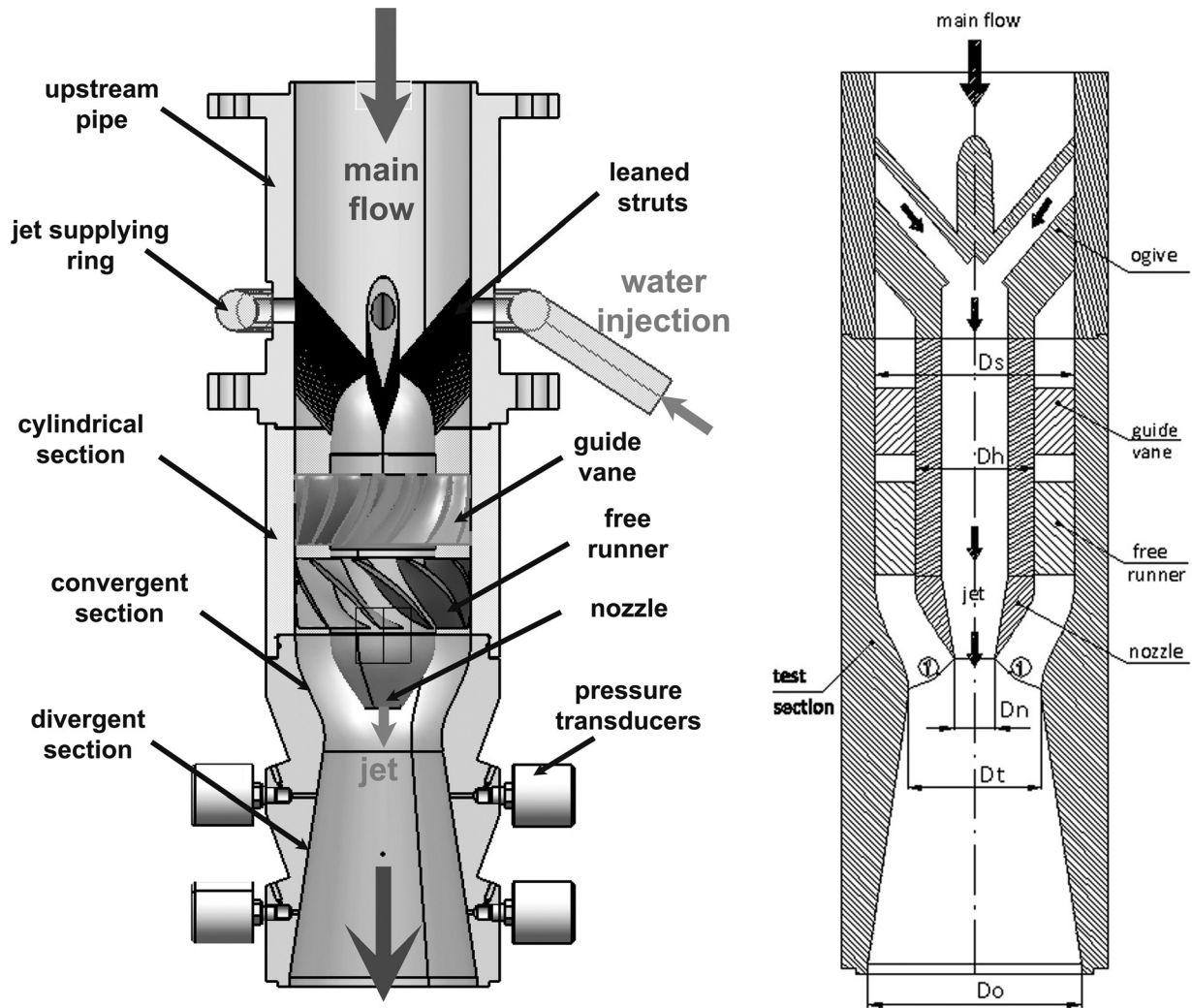
Fig. 2   The swirl apparatus and cross section with the main elements

3   Pressure Measurements

The aim of this research is to assess a new method for diminishing the pressure pulsations and increase pressure recovery in a straight conical diffuser similar to the draft tube cone of a Francis turbine. The recorded unsteady pressure is used to analyze the dynamic and energetic performances. Pressure fluctuation data are used to assess the dynamic behavior while the mean pressure is needed for energetic assessment.

Energetically, the pressure recovery coefficient along the cone is determined by analyzing the averaged pressure. Dynamically, the decelerated swirling flow's amplitude and frequency and the type of conical diffuser's unsteadiness are determined by analyzing the Fourier spectra. The latter is evaluated using two pressure transducers flash mounted on the same level. According to Jacob and Prenat [27], depending on the phase between the two pressure signals the conical diffuser unsteadiness is either rotating or plunging oscillation type.

Four levels were selected for pressure measurements as shown in Fig. 4. The top level located in the test section's throat was denoted MG0. This level is considered the benchmark (the references for dimensionless values are being calculated with respect to this level). The other levels MG1, MG2, and MG3 correspond to 50, 100, and 150 mm downstream in the discharge cone, relative to the MG0. The first step of experimental procedure was to confirm that two pressure transducers located on the same level indicate the same static pressure. The capacitive pressure transducers used for measurements have an accuracy of 0.13% within a range of ±1 bar relative pressure. Having two pressure transducers on the same level, allows the same level average pressure comparison confirming the transducer's accuracy.

The unsteady pressure was measured at the test section's wall to assess the influence of the water injection control method. A main operating discharge of 30 l/s was used for experimental investigation in all regimes. The water jet discharge used for control purposes was calculated as a percentage of the main flow. Pressure pulsation measurements were performed while injecting water of 5%, 7.5%, 9.3%, 10%, 10.9%, 11.3%, 11.6%, 11.9%, 12.5%, 13%, and 14% discharge. The unsteady pressure is measured using eight transducers mounted on the conical diffuser's wall. In order to verify the measurements repeatability ten experiments were performed for each jet discharge value. Each set corresponds to an acquisition time interval of 32 s at a

Table 1   Vortex rope Strouhal number for the model Francis turbine and for the swirl apparatus

|	Francis model turbine at partial discharge [22]	Swirl apparatus
f (Hz)	4.17	14.9
D_{ref} (m)	0.4	0.1
V_{ref} (m/s)	4.084	3.82
$Sh = (f \times D_{ref})/V_{ref}$	0.408	0.39
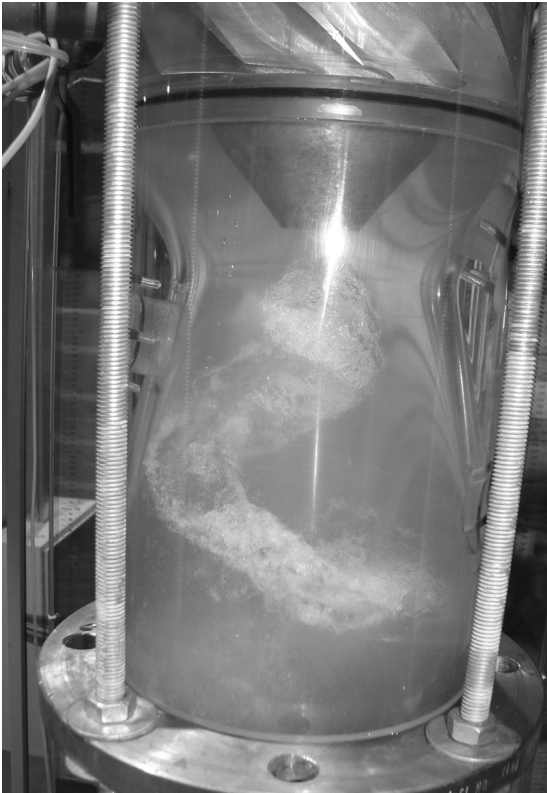
(a)

(b)

Fig. 3 The visualization of the cavitating vortex rope from the discharge cone of the test section (*a*) and with water injection (*b*)

sampling rate of 256 samples/s. The investigations reported in this paper follow two research directions. Energetically, the cone pressure recovery coefficient is evaluated using the experimental data to assess the efficiency of the proposed control method for different jet discharge values. Dynamically, the pressure pulsations are evaluated for several different jet discharge values.
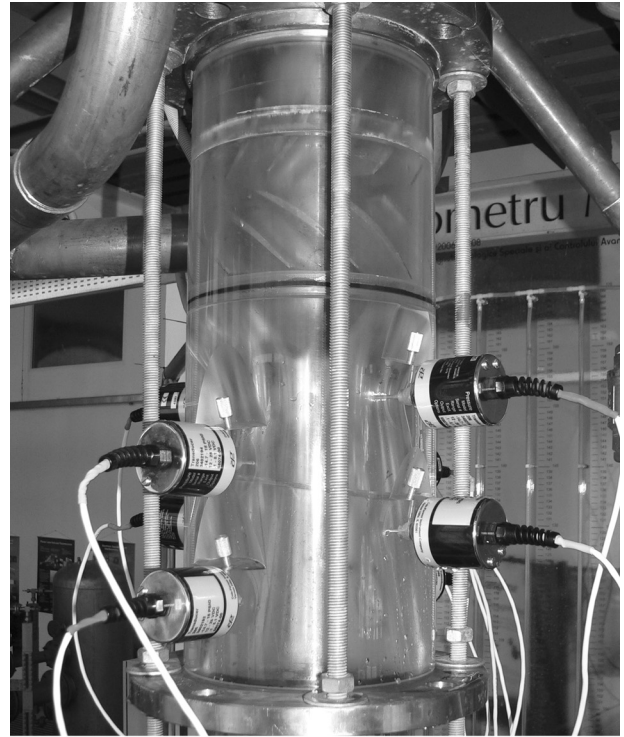
(a)
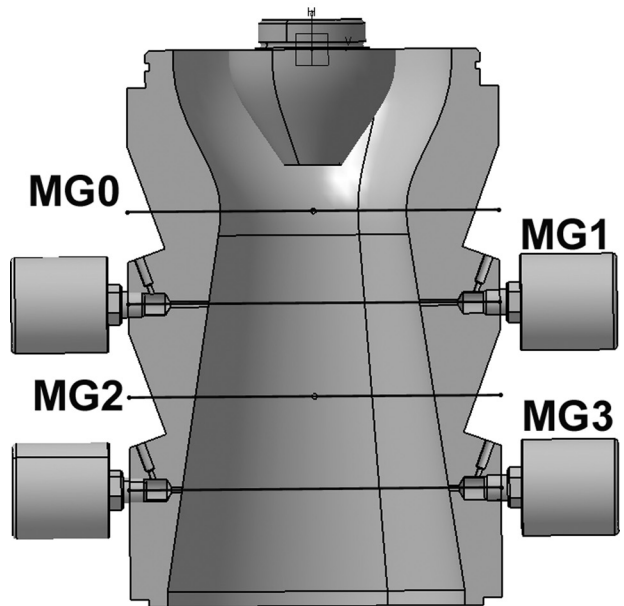
(b)

Fig. 4 The test section with wall flash mounted pressure transducers on the rig (*a*) and the labels for each level (*b*)

4 Pressure Data Analysis

4.1 Averaged Pressure Analysis. Energetically, the mean pressure has to be analyzed for all measurement levels in order to assess the influence of our flow control approach on the overall diffuser efficiency. The pressure recovery coefficient is given by the following equation:

$$c_p = \frac{\overline{p} - \overline{p_{\mathrm{MG0}}}}{\rho \cdot v_t^2 / 2} \tag{1}$$

where c_p is the pressure recovery coefficient, $\overline{p}_{MG0}$ is the mean pressure recorded in the MG0 level, $\overline{p}$ is the mean pressure recorded at downstream levels from MG0 (see Fig. 4), ρ is the water density, and v_t is the throat velocity. The pressure recovery coefficient expressed by Eq. (1) for the MG1, MG2, and MG3 levels in terms of the ratio of Q_{jet}/Q was analyzed. This coefficient (relative to the throat section labeled MG0 which is considered as a reference) is plotted in Fig. 5 for all the above mentioned levels. The measurements have been repeated ten times, with a resulting standard deviation less than 2% as shown with error bars in Fig. 5.

After a drop down at 1%, the pressure recovery coefficient start to increase up to 2% discharge for the first 50 mm along the cone (level MG1), Fig. 5(a). At over 2% control jet discharge value, the stagnant region is located below the MG1 level. As such, increasing the control jet discharge over this value causes insignificant pressure recovery coefficient modification at the MG1 level (Fig. 5(a)). The pressure recovery coefficient variation related to the control jet discharge at the MG2 level (located in the middle of the cone) reveals two distinctive regions. A significant improvement (about 30%) of the pressure recovery coefficient is observed between 0% and 5% control jet discharge. Over this 5% value, the pressure recovery coefficient increases monotonically up to 60% in the full water injection domain (Fig. 5(b)). At the MG3 level one can see a monotonic increase about 30% of the pressure recovery coefficient as the control jet discharge increases from 0% to about 13%, Fig. 5(c). It is important to note that the pressure recovery coefficients for levels MG2 and MG3 continue to grow as the control jet discharge exceeds the critical threshold value (11.5%) towards 13%. This suggests a better pressure recovery along the cone up to 13% control jet discharge. However, the optimum control jet discharge value is a balance between the cone recovered energy and the jet hydraulic power [28]. Over the 13% control jet discharge value the pressure recovery coefficient is practically constant for all the levels. Consequently, an analysis of the pressure recovery coefficient variation along the cone is performed for a control jet discharge of 14%. Figure 6 shows a comparison of the pressure recovery coefficient's distribution along the cone in two cases, vortex rope (no control jet) and 14% control jet discharge. One can see an increase of the pressure recovery coefficient for all levels (MG1, MG2, and MG3) in the jet case versus the vortex rope case, Fig. 6. At MG1 level the pressure recovery coefficient increases by 23% (from around 0.55 to around 0.68). The second level MG2 shows a significant improvement of 110% of this coefficient (from around 0.39 to around 0.82). On the third investigated level MG3, one can notice an increase of 47% of this coefficient (from around 0.55 to around 0.81). Figure 6 demonstrates that our control method increases the energy recovery in the cone which exhibits the designed hydrodynamic behavior even in these conditions [17].

4.2 Unsteady Pressure Analysis.
Dynamically, the unsteady pressure signal's Fourier spectra has to be analyzed in order to understand the swirling flow configuration and to assess the water injection method. A new approach is employed to analyze the pressure signal. It offers a metric which allows quantitatively dynamical characterization of the unsteady pressure signal. Based on the acquired unsteady pressure signal, this approach leads to an accurate evaluation of the unsteadiness level. Mathematically, it compares two signals having different Fourier spectra (amplitude, harmonics number, and their frequencies). The second signal is reconstructed based on the acquired one using the Parseval's theorem. It has the same frequency as the first harmonic of the acquired signal and root mean square (rms) equivalent amplitude.

The results will be presented as dimensionless. The following reference values are considered in the analysis: (i) the throat diameter of the test section $D_t = 0.1$ m, (ii) the overall throat discharge, which includes the main circuit discharge $Q = 30$ l/s and the jet discharge Q_{jet} (associated with a different water injection regime), (iii) the throat average static pressure denoted $\overline{p}_{MG0}$.
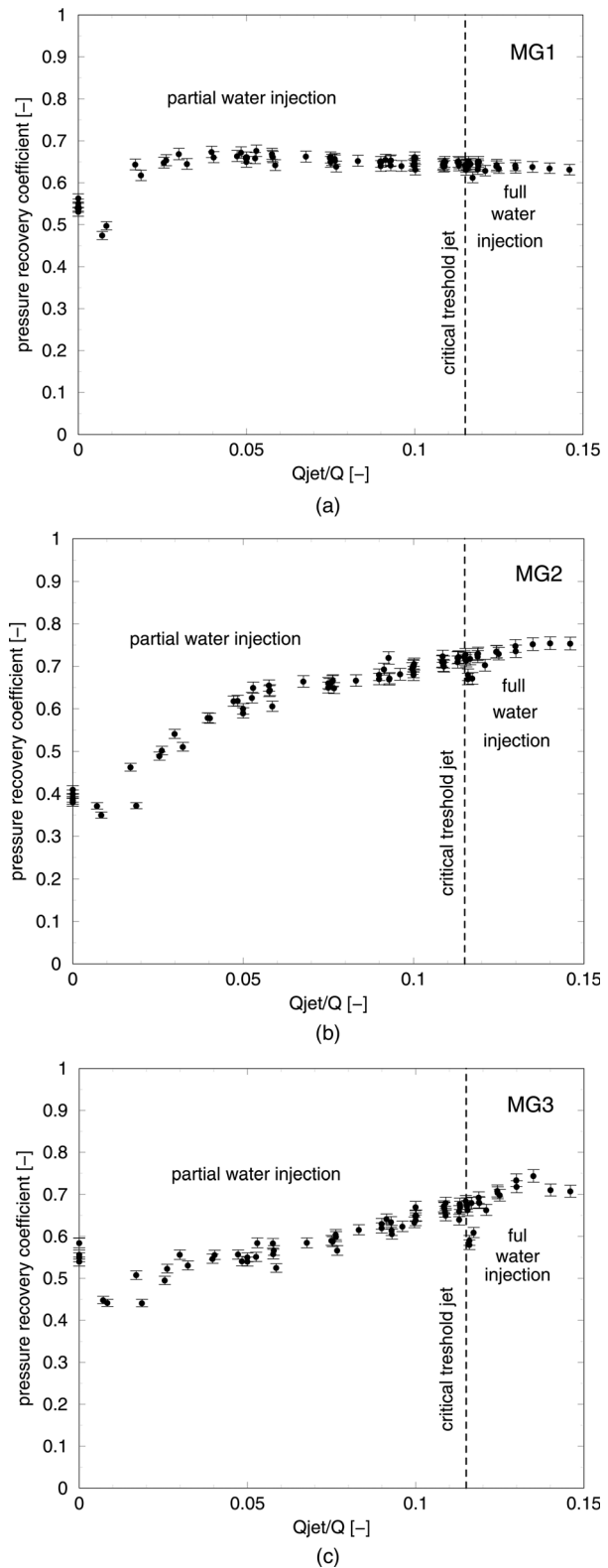

Fig. 5 Evolution of the pressure recovery coefficient for MG1 (a), MG2 (b), and MG3 (c) levels depending on the Q_{jet}/Q

The first dimensionless parameter to be used is the Strouhal number Eq. (2) associated with the frequency. The throat reference velocity value takes into account the overall discharge which includes the main circuit's and the jet's discharges. Particularly, the overall discharge equals to the main circuit's discharge when the jet is turned off,
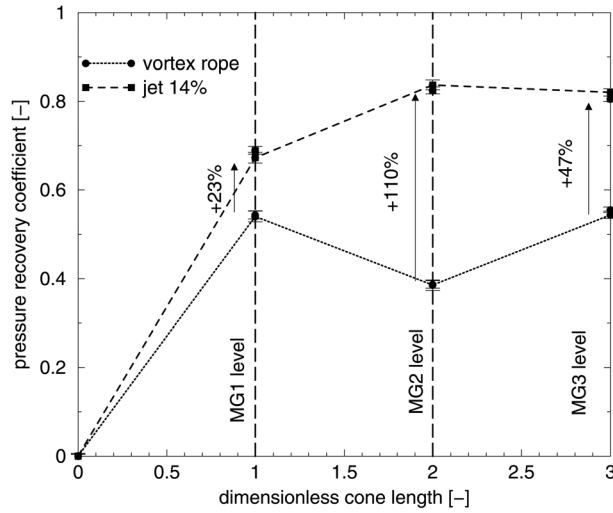
Fig. 6 Pressure recovery coefficient comparison between the swirling flow with vortex rope regime and the full water injection 14% discharge of the main flow at all levels

$$Sh = f \cdot \frac{D_t}{v_t} \quad \text{where} \quad v_t = \frac{4(Q + Q_{\text{jet}})}{\pi D_t^2} \tag{2}$$

The second dimensionless parameter to be used is the pressure's amplitude. This is described in the following. The Fourier transform for a continuous signal $p(t)$ is defined according to statistical theory [29,30]

$$p(t) = \frac{p_0}{2} + \sum_{m=1}^{\infty} \left[a_m \cos\left(\frac{2\pi mt}{T}\right) + b_m \sin\left(\frac{2\pi mt}{T}\right) \right] \tag{3}$$

where T is the period, m the mode, t the time, and a_m and b_m are the Fourier transform coefficients defined as

$$a_m = \frac{2}{T} \int_{t_0}^{t_0+T} p(t) \cos\left(\frac{2\pi mt}{T}\right) dt; \quad b_m = \frac{2}{T} \int_{t_0}^{t_0+T} p(t) \sin\left(\frac{2\pi mt}{T}\right) dt \tag{4}$$

with t_0 being the initial time.

The first coefficient represents the average value $\bar{p}$ of the signal and it is defined in Eq. (5),

$$p_0 = \frac{2}{T} \int_{t_0}^{t_0+T} p(t) dt = 2\bar{p} \tag{5}$$

where $p_0/2$ is the mean value of $p(t)$. The amplitude and the angular frequency can be written as follows:

$$A_m = \sqrt{a_m^2 + b_m^2}; \quad \omega_m = m \frac{2\pi}{T} \tag{6}$$

The Parseval's theorem applied to the Fourier transform is written as below,

$$\frac{1}{T} \int_{t_0}^{t_0+T} |p(t)|^2 dt = \left(\frac{1}{2} p_0\right)^2 + \frac{1}{2} \sum_{m=1}^{\infty} (a_m^2 + b_m^2) \tag{7}$$

The pressure root mean square (rms) is defined according to the following equation:

$$p_{\text{rms}} = \sqrt{\frac{1}{T} \int_{t_0}^{t_0+T} (p(t) - \bar{p})^2 dt} \tag{8}$$

Appling the Parseval's theorem yields

$$p_{\text{rms}}^2 = \frac{1}{T} \int_{t_0}^{t_0+T} p^2(t) dt - \bar{p}^2 \tag{9}$$

According to this theorem, the pressure's rms is defined as

$$p_{\text{rms}}^2 = \frac{1}{2} \sum_{m=1}^{\infty} (a_m^2 + b_m^2) \tag{10}$$

For a discrete signal the following equation applies:

$$p_{\text{rms}} = \sqrt{\frac{1}{N} \sum_{i=1}^{N} (p_i - \bar{p})^2} = \sqrt{\frac{1}{2} \sum_m A_m^2} \tag{11}$$

The amplitude's dimensionless form for a discrete signal can be defined as

$$A = \sqrt{2} p_{\text{rms}}$$

leading to

$$\bar{A} = \left(\sqrt{2} p_{\text{rms}}\right) \bigg/ \left(\frac{1}{2} \rho v_t^2\right) \quad \text{where} \quad v_t = \frac{4(Q + Q_{\text{jet}})}{\pi D_t^2} \tag{12}$$

This means that the equivalent amplitude (A) of the pressure pulsation is proportional to the rms. In other words, the equivalent amplitude collects all spectrum contributions. As a result, the original signal can be accurately reconstructed using its fundamental frequency and the equivalent amplitude computed based on the pressure signal. Both the acquired (points) and the reconstructed signals according to the above approach (continuous line), can be seen in Fig. 7 for all investigated levels. However, this procedure may be employed to reconstruct rms equivalent signals using the fundamental frequency and a number of harmonics. With no control water jet the swirling flow loses the stability and develops the vortex rope and associated unsteadiness. Consequently, the vortex rope's Strouhal number is 0.39 as shown in Fig. 8(b). A qualitative model of the vortex rope flow field was given by Nishi et al. [31] who observed a quasi-stagnant (stalled) central region with the spiral vortex core wrapped around it. This statement was validated with experimental data using the FLINDT turbine model operating at part load by Resiga et al. [32]. The vortex rope geometrical shape is almost cylindrical having a very small eccentricity (see Fig. 3) close to the nozzle. It is important to note that at MG0 and MG1 levels (Fig. 7), the amplitude of the fundamental frequency associated with the vortex rope is dominant, while the higher harmonics have negligible amplitudes. The highest equivalent amplitude corresponds to the MG2 level, Fig. 8(a) (the rhombus-marked curve). These differences in amplitude for each level (Fig. 8(a), corresponding to $Q_{\text{jet}}/Q = 0$) are due to the vortex rope shape. Indeed, the angle of the cone the vortex rope wraps on larger than the geometry cone's angle. As a result, the vortex rope's eccentricity is largest at the MG2 level. As it advances downstream, the vortex rope loses strength and begins to disintegrate (level MG3) and its higher harmonics increase significantly [33,34].

When starting to inject the water, the stagnant region associated with the vortex rope is gradually pushed downstream of the cone. Consequently, at 5% control jet discharge the vortex rope's amplitudes remain almost constant for the MG0 level, decrease for the next two levels (MG1 and MG2) approximately by 10%, and increase for the last level (MG3) by approximately 40% (Fig. 8(a)). The vortex rope Strouhal number sharply decreases from 0.39 to 0.27 (Fig. 8(b)). Exceeding this discharge value leads to a monotonous decrease of frequency and amplitudes for all
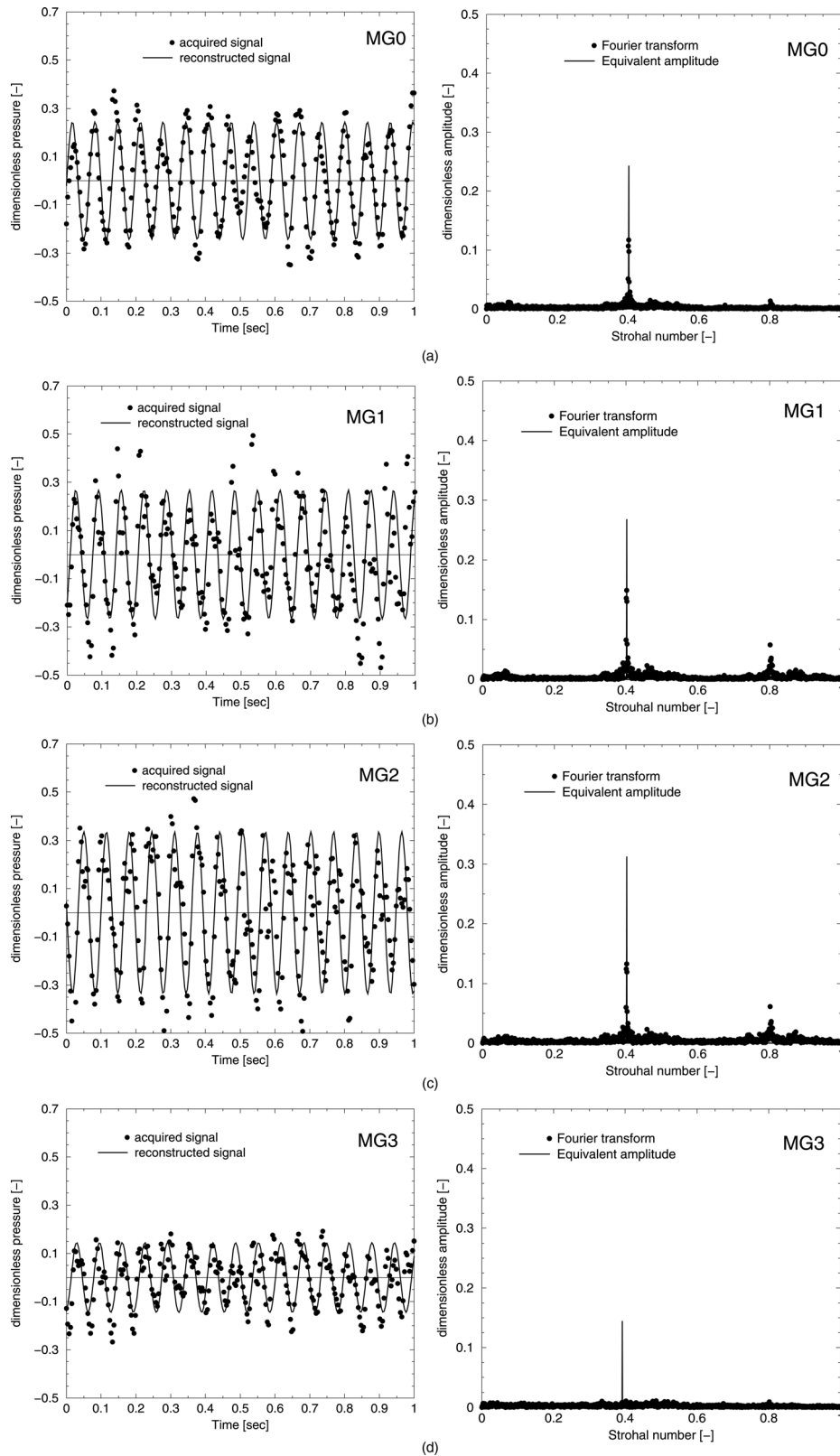
Fig. 7 Reconstructed signal against acquired signal for MG0, MG1, MG2, and MG3 levels (left) and equivalent amplitude overlapped with Fourier spectra of pressure signal (right) in the case of swirling flow with vortex rope

levels until reaching the 11.5% jet discharge critical threshold. At 11.5% jet discharge, the frequency decreases by 35% with respect to no control jet. Correspondingly, the amplitudes decrease for all levels except MG3 due to the fact that the top of the stagnant region reaches this level. Over this critical threshold, this region gets completely pushed out of the cone. As a result, a sudden drop is noted in both amplitudes (at all levels) and frequency. Further jet discharge increase causes no modification in amplitudes and
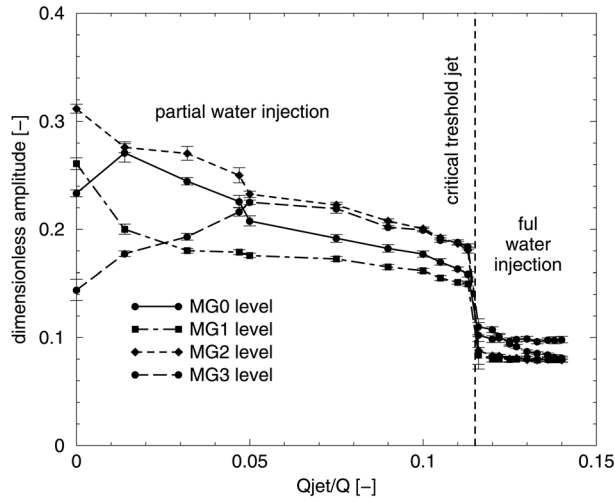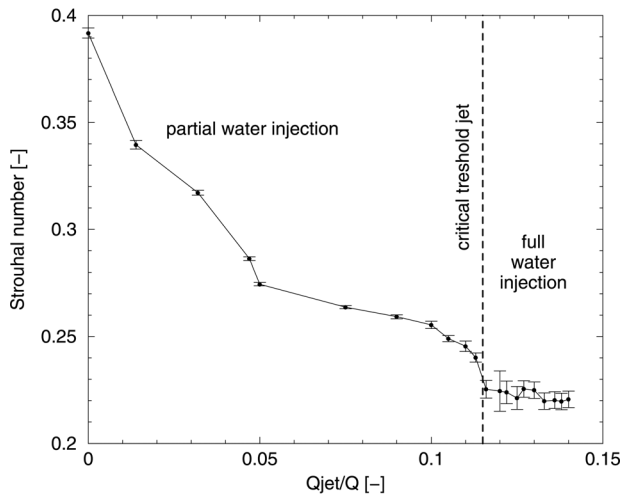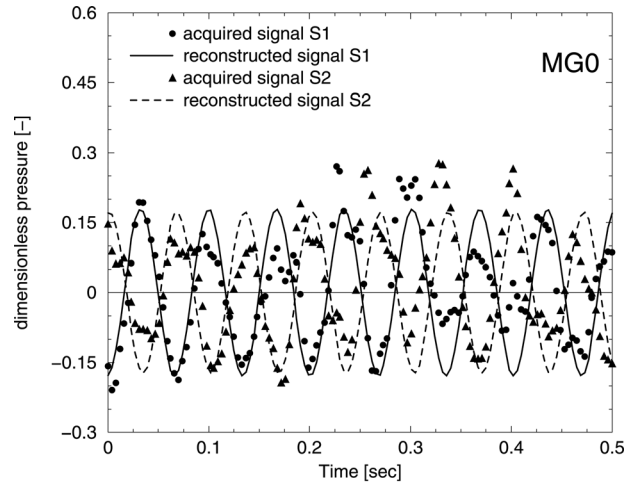
Fig. 8 Equivalent amplitudes corresponding to levels from the test section (a) and Strouhal number (b) versus ratio Q_{jet}/Q

Fig. 9 Dimensionless pressure signals for MG0 level for swirling flow with vortex rope (a) and 14% full water injection (b)
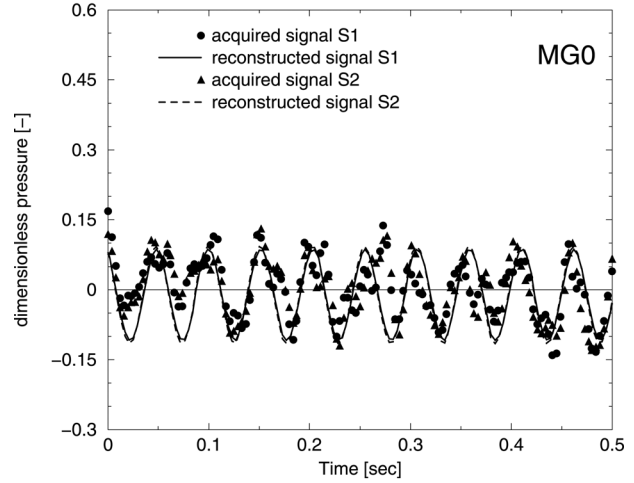
frequency. Both plots in Fig. 8 include the 2% error band of the main value for each measuring point. It is important to note that below the critical jet threshold the error bands are small. This occurs due to the fact that the value of the amplitudes and frequency associated to the swirling flow are significantly larger than the noise. Over the threshold, the error bands increase due to the fact that the noise becomes significant with respect to the measured values.

4.3 Pressure Signal Decomposition. As mentioned above, according to Jacob and Prenat [27], there are two types of draft tube cone pulsations. The plunging type (synchronous) is acting like a water hammer along the cone axis. The rotation type (asynchronous) is acting in the cross sections. A minimum of two sensors located on the same section are required for measurements in order to evaluate this pulsation type. The asynchronous pulsation is produced by instabilities, such as the vortex rope due to its shape and its precession motion, Koutnik et al. [35]. Two unsteady pressure signals S1 and S2 are used to discriminate between the two pulsation types as follows:

$$\frac{S_1 + S_2}{2} \Rightarrow \text{Synchronous component (plunging) of the pressure signal}$$

$$(13)$$

$$\frac{S_1 - S_2}{2} \Rightarrow \text{Asynchronous component (rotating) of the pressure signal}$$

$$(14)$$

In this analysis, the S1 and S2 signals are reconstructed from the acquired experimental data using the procedure based on the Parceval's theorem. As described above, this procedure was employed at all levels for ten cases (from no jet to 14% control jet discharge). Figure 9 exemplifies the S1 and S2 reconstructed signals in the two outermost cases for the MG0 level: no control jet and 14% control jet discharge.

As mentioned above, each reconstructed signal has the same frequency as the first harmonic of the acquired signal used and its amplitude is rms-equivalent. Therefore, the reconstructed signal is sinusoidal. The phase between the two reconstructed signals indicates the type of pressure pulsation. Indeed, if S1 and S2 are in phase then according to Eq. (14) the asynchronous component vanishes. In this first ideal case, only the pure plunging pulsation is detected. On the contrary, when S1 and S2 are out of phase, according to Eq. (13) the synchronous component vanishes. This is the second ideal case in which only the pure rotation component is found. Generally, both pulsation types are expected to be found in all investigated cases. The pressure pulsation type's distributions along the cone in the two outermost cases are displayed in Fig. 10. The swirling flow with vortex rope case (Fig. 10(a)) reveals predominant rotational pressure pulsations at all
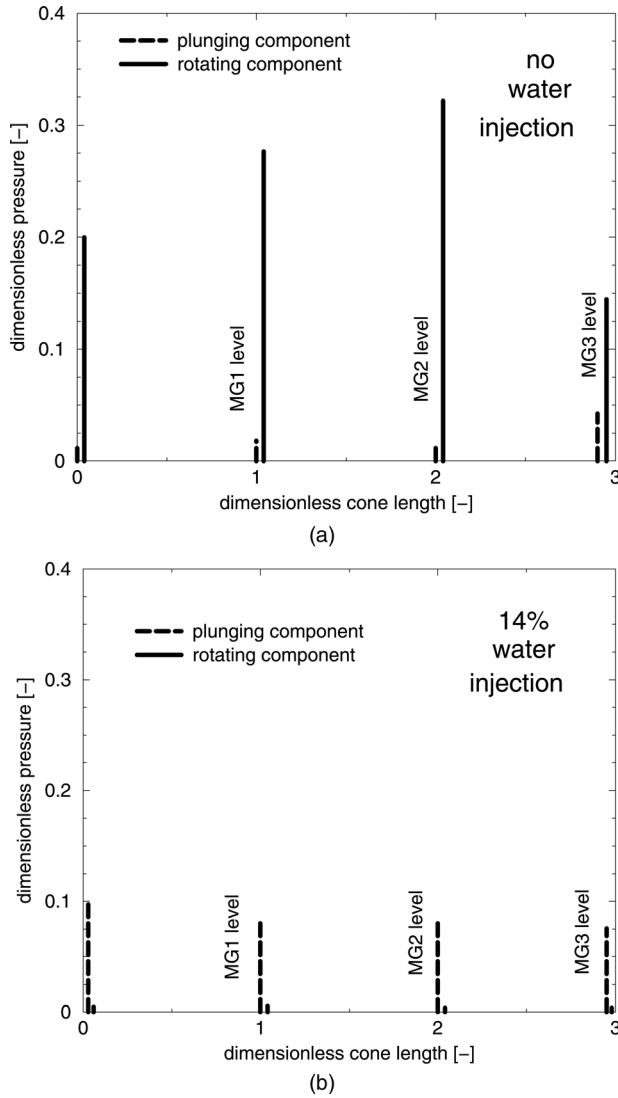
Fig. 10 Dimensionless pressure signal decomposition for swirling flow with vortex rope (*a*) and 14% water injection (*b*) in the length of the cone

investigated levels. This is expected due to the vortex rope precession motion. On the contrary, the 14% control jet discharge (Fig. 10(*b*)) highlights a significant decrease (about 30 times for the most significant level – MG2) of the rotational pulsation component. However, one can observe an increase (about five times for the MG2 level) of the plunging component of the pressure pulsation in comparison to the vortex rope case. We conclude from Fig. 10 that the jet injection along the cone axis removes the precessing helical vortex and its associated rotating pressure fluctuations. As a result, the swirling flow becomes axisymmetric, and the relative increase in the level of plunging pressure fluctuations might be related to a possible "subcritical" swirl configuration, as defined by Benjamin [36], when the swirling flow can sustain axisymmetric waves.

Figure 11 displays the two pressure component types (plunging and rotational) distribution with respect to the control jet discharge values for the four investigated levels. The following ten values of jet discharges were used for measurements: 0%, 1.4%, 3.2%, 5%, 7.5%, 9%, 11%, 11.6%, 13.8%, and 14%. The rotational component of the pressure pulsation associated with the vortex rope is significant for all jet values located in the partial water injection domain. In the full water injection domain, the plunging pulsation becomes predominant for all injection values.
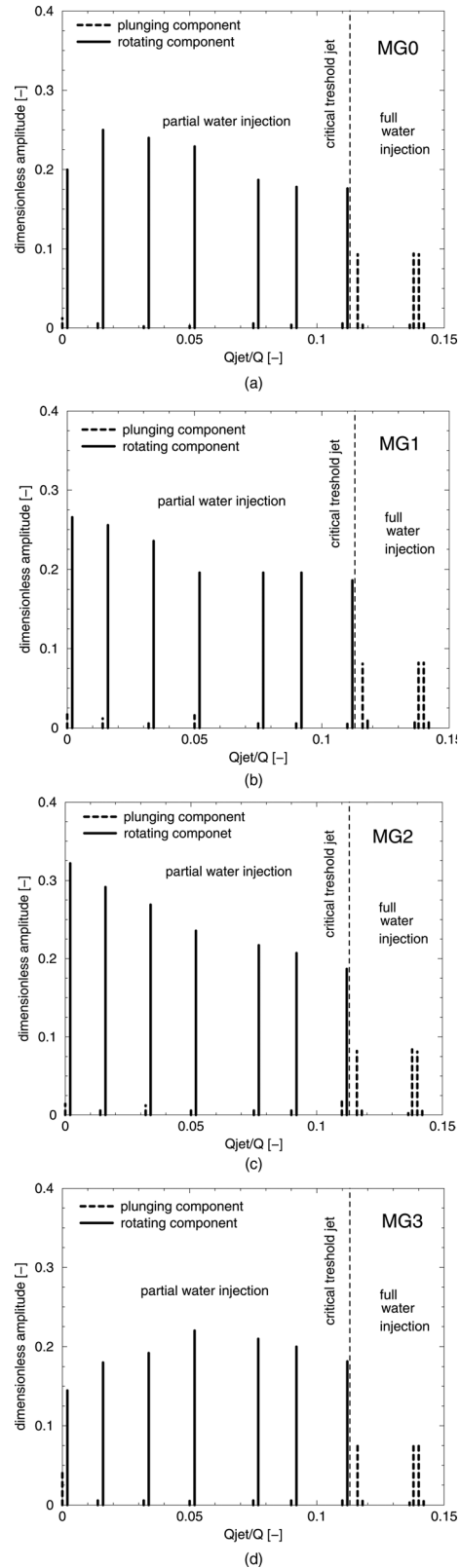

Fig. 11 Pressure pulsations types' distributions versus control jet discharge

This behavior characterizes all investigated levels in Fig. 11. Overall, the pulsations have decreased. The significant decrease of the rotational pulsation component allows a safe turbine operation at these conditions.

5 Conclusions

The paper investigates the decelerated swirling flow with vortex rope in a conical diffuser, using a swirl generator that mimics the flow in the discharge cone of hydraulic turbines operated at partial discharge. A novel flow control technique which uses axial injection is proposed, in order to improve the pressure recovery coefficient and to mitigate the pressure pulsations. The unsteady pressure measurements were performed on the wall test sections. Eight points located on four levels were investigated. For each operating mode (swirling flow with vortex rope or swirling flow with water injection) ten sets were measured.

Firstly, the average pressure was determined to compute the pressure recovery coefficient in order to assess the energetic performance of the new control method. The jet discharge increase reveals two domains: the partial water injection and the full water injection. The two domains are separated by the critical water injection threshold at 11.5% discharge. The experiments reveal an increase of the pressure recovery coefficient when increasing the control jet discharge. Overall, the pressure recovery coefficient associated with the full water injection leads to about 30% improvements. The highest improvement was measured for the MG2 level (located in the middle of the cone) and it was about 60%. This fact suggests a better energetic behavior of compact discharge cones. These overall results demonstrate an improved energetic cone behavior at this operating point. However, the optimum control jet discharge value has to be selected as a balance between the draft tube cone recovered energy and the jet hydraulic power. Although, the method proves consistent energy recovery, the 11.5% jet discharge value is prohibitive from an energetic point of view if taking into account that the control jet is considered a volumetric loss.

Secondly, the dynamical behavior associated to this control method was investigated by analyzing the pressure signal's Fourier spectra. A new method based on the Parceval's theorem was employed to reconstruct the acquired unsteady pressure signal. The result of this procedure was a sinusoidal signal having the same frequency as the first harmonic of the acquired signal and rms equivalent amplitude. As the control jet discharge increases, the unsteady pressure frequency decreases monotonically in the partial water injection domain. During the full water injection domain, the frequency remains practically constant. Generally, the unsteady pressure amplitudes decrease as the jet discharge increases in the partial water injection domain (MG0 and MG3 show a different variation pattern for small discharge values). The amplitudes variations display a sudden drop at 11.5% jet discharge. This is the reason why the 11.5% discharge was labeled "critical threshold jet." Above this value, the amplitudes exhibit negligible variations with regard to the jet discharge. Therefore, the instabilities associated with the vortex rope have been mitigated. As such this domain becomes desirable for operation.

The unsteady pressure signal is decomposed into rotational and plunging components. The rotational component of pressure pulsation associated with the vortex rope is significant for all jet values located in the partial water injection domain. In the full water injection domain, the plunging pulsation becomes dominant for all injection values, but with small amplitudes. In general, the pulsations have decreased. The significant decrease of the rotational pulsation component suggests operation under these conditions. However, the plunging pulsation propagates into the whole hydraulic system. Mitigation of this component is the subject of future research.

Generally, the proposed control method leads to an improvement of energetic and dynamic performances of the decelerated swirling flow in the discharge cone. The necessary jet discharge values to attain optimum operation conditions have to be evaluated particularly from case to case. Each case will be defined by the cone geometry and the swirling flow configuration. Although 0.115 jet discharge seems to be too large for a real turbine with respect to pumping energy, one should note that the jet does not necessarily need a separate water supply. The novel flow-feedback technique proposed by Susan-Resiga et al. [25] uses a fraction of the main discharge, collected near the wall, at the cone outlet, to supply the jet. It is proved numerically [25] and experimentally [37] that the pressure excess at the cone wall with respect to nozzle outlet can drive the control jet with large enough discharge in order to mitigate the central stagnation region and associated vortex rope.

Nomenclature

$a_m, b_m(\text{Pa})$ = Fourier transform coefficients
$D_h(\text{m})$ = hub diameter of the swirl generator, $D_h = 0.09(\text{m})$
$D_i(\text{m})$ = nozzle exit diameter, $D_i = 0.033(\text{m})$
$D_o(\text{m})$ = outlet diameter from the test section, $D_o = 0.16(\text{m})$
$D_s(\text{m})$ = shroud diameter of the swirl generator, $D_s = 0.15(\text{m})$
$D_t(\text{m})$ = reference diameter from the throat of the convergent-divergent test section, $D_t = 0.1(\text{m})$
$f(\text{Hz})$ = dominant frequency from Fourier spectrum
$Q(\text{m}^3/\text{s})$ = main discharge from the primary hydraulic circuit
$Q_{\text{jet}}(\text{m}^3/\text{s})$ = jet discharge at the nozzle
c_p = pressure recovery coefficient
$p(t)$ = continuous pressure signal
$\overline{p}(\text{Pa})$ = average pressure for each level
$p_0(\text{Pa})$ = mean value of a pressure signal
$\overline{p}_{\text{MG0}}(\text{Pa})$ = average pressure from level MG0 situated in the throat of convergent-divergent test section
$p_{\text{rms}}(\text{Pa})$ = root mean square of a continuous pressure signal
Sh = Strouhal number
S_1, S_2 = pressure signals measured for the same level
$v_t(\text{m}/\text{s})$ = reference velocity from the throat of convergent-divergent test section

References

[1] Susan-Resiga, R., Ciocan, G. D., Anton, I., and Avellan, F., 2006, "Analysis of the Swirling Flow Downstream a Francis Turbine Runner," ASME J. Fluids Eng., 128, pp. 177–189.

[2] Rheigans, W. J., 1940, "Power Swings in Hydroelectric Power Plant," Trans. ASME, 62(174), pp. 171–184.

[3] Wang, F., Li, X., and Ma, J. Y. M., 2009, "Experimental Investigation of Characteristic Frequency in Unsteady Hydraulic Behavior of a Large Hydraulic Turbine," J. Hydrodynam., 21(1), pp. 12–19.

[4] Baya, A., Muntean, S., Câmpian, V. C., Cuzmoş, A., Diaconescu, M., and Bălan, G., 2010, "Experimental Investigations of the Unsteady Flow in a Francis Turbine Draft Tube Cone," Proceedings of the 25th IAHR Symposium on Hydraulic Machinery and Systems, IOP Conf. Ser.: Earth and Environmental Science of Institute of Physics, 12, p. 012007.

[5] Arpe, J., Nicolet, C., and Avellan, F., 2009, "Experimental Evidence of Hydroacoustic Pressure Waves in a Francis Turbine Elbow Draft Tube for Low Discharge Conditions," ASME J. Fluids Eng., 131(8), p. 081102.

[6] Thicke, R. H., 1981, "Practical Solutions for Draft Tube Instability," Int. Water Power Dam Constr., 33(2), pp. 31–37.

[7] Qian, Z.-D., Yang, J.-D., and Huai, W.-X., 2007, "Numerical Simulation and Analysis of Pressure Pulsation in Francis Hydraulic Turbine With Air Admission," J. Hydrodynam., 19(4), pp. 467–472.

[8] Pappilon, B., Sabourin, M., Couston, M., and Deschenes, C., 2002, "Methods for Air Admission in Hydro Turbines," Proceedings of the 21st IAHR Symposium on Hydraulic Machinery and Systems, Lausanne, Switzerland, pp. 1–6.

[9] Kjeldsen, M., Olsen, K., Nielsen, T., and Dahlhaug, O., 2006, "Water Injection for the Mitigation of Draft Tube Pressure Pulsations," IAHR International Meeting of the Workgroup on Cavitation and Dynamic Problems in Hydraulic Machinery and Systems, Barcelona, Spain.

[10] Nishi, M., Wang, X. M., Yoshida, K., Takahashi, T., and Tsukamoto, T., 1996, "An Experimental Study on Fins, Their Role in Control of the Draft Tube Surging," Hydraulic Machinery and Cavitation, E. Cabrera, V. Espert, and F. Martínez, eds., Kluwer Academic Publishers, Dordrecht, The Netherlands, pp. 905–914.

[11] Miyagawa, K., Sano, T., Kunimatsu, N., Aki, T., and Nishi, M., 2006, "Flow Instability With Auxiliary Parts in High Head Pump – Turbines," Proceedings of the 23rd IAHR Symposium on Hydraulic Machinery and Systems, Yokohama, Japan, Paper No. F307.

[12] Vevke, T., 2004, "An Experimental Investigation of Draft Tube Flow," Ph.D. thesis, Norwegian University of Science and Technology, Trondheim, Norway.

[13] Kurokawa, J., Kajigaya, A., Matusi, J., and Imamura, H., 2000, "Suppression of Swirl in a Conical Diffuser by Use of J-Groove," Proceedings of the 20th IAHR Symposium on Hydraulic Machinery and Systems, Charlotte, NC, Paper No. DY-01.

[14] Susan-Resiga, R., Vu, T. C., Muntean, S., Ciocan, G. D., and Nennemann, B., 2006, "Jet Control of the Draft Tube in Francis Turbines at Partial Discharge," Proceedings of the 23rd IAHR Symposium on Hydraulic Machinery and Systems, Yokohama, Japan, Paper No. F192.

[15] Kirschner, O., Grupp, J., and Schmidt, H., 2008, "Experimental Investigation of Vortex Control in a Simplified Straight Draft Tube Model," 4th German-Romanian Workshop of Vortex Dynamics in Hydraulic Machinery, Stuttgart, Germany, IHS, University of Stuttgart.

[16] Vu, T. C., and Retieb, S., 2002, "Accuracy Assessment of Current CFD Tools to Predict Hydraulic Turbine Efficiency Hill Chart," Proceedings of the 21st IAHR Symposium on Hydraulic Machinery and Systems, Lausanne, Switzerland, pp. 193–198.

[17] Bosioc, A., Susan-Resiga, R., and Muntean, S., 2008, "Design and Manufacturing of a Convergent-Divergent Section for Swirling Flow Apparatus," 4th German-Romanian Workshop in Turbomachinery, Stuttgart, Germany, IHS, University of Stuttgart.

[18] Avellan, F., 2000, "Flow Investigation in a Francis Draft Tube: The FLINDT Project," Proceedings of the 20th IAHR Symposium on Hydraulic Machinery and Systems, Charlotte, NC, Paper No. DY-03.

[19] Susan-Resiga, R., Muntean, S., Tanasa, C., and Bosioc, A. I., 2008, "Hydrodynamic Design and Analysis of a Swirling Flow Generator," 4th German-Romanian Workshop of Vortex Dynamics in Hydraulic Machinery, Stuttgart, Germany, IHS, University of Stuttgart.

[20] Bosioc, A., Tanasa, C., Muntean, S., and Susan-Resiga, R., 2010, "Pressure Recovery Improvement in a Conical Diffuser With Swirling Flow and Jet Injection," Proc. Rom. Acad., Ser. A, 11(3), pp. 245–252.

[21] Zangeneh, M., 1991, "A Compressible Three-Dimensional Design Method for Radial and Mixed Flow Turbomachinery Blades," Int. J. Numer. Methods Fluids, 13, pp. 599–624.

[22] Ciocan, G., Iliescu, M., Vu, T. C., Nennemann, B., and Avellan, F., 2007, "Experimental Study and Numerical Simulation of the FLINDT Draft Tube Rotating Vortex," ASME J. Fluids Eng., 129, pp. 146–158.

[23] Stein, P., Sick, M., Doerfler, P., White, P., and Braune, A., 2006, "Numerical Simulation of the Cavitating Draft Tube Vortex in a Francis Turbine," Proceedings of the 23rd IAHR Symposium on Hydraulic Machinery and Systems, Yokohama, Japan, p. 228.

[24] Stein, P., 2007, "Numerical Simulation and Investigation of Draft Tube Vortex Flow," Ph.D. thesis, Coventry University, United Kingdom.

[25] Susan-Resiga, R., and Muntean, S., 2008, "Decelerated Swirling Flow Control in the Discharge Cone of Francis Turbines," The 4th International Symposium on Fluid Machinery and Fluid Engineering, J. Xu, Y. Wu, and Y. Zhang, eds., Beijing, China, Springer, pp. 89–96.

[26] Bosioc, A., Tanasa, C., Muntean, S., and Susan-Resiga, R., 2009, "2D LDV measurements of Swirling Flow in a Simplified Draft Tube," The 14th International Conference on Fluid Flow Technologies, Budapest, Hungary.

[27] Jacob, T., and Prenat, J., 1996, "Francis Turbine Surge: Discussion and Data Base," Proceedings of the 18th IAHR Symposium on Hydraulic Machinery and Cavitation, Valencia, Spain, Vol. 2, pp. 855–865.

[28] Susan-Resiga, R., Muntean, S., Hasmatuchi, V., Anton, I., and Avellan, F., 2010, "Analysis and Prevention of Vortex Breakdown in the Simplified Discharge Cone of a Francis Turbine," ASME J. Fluids Eng., 132(5), p. 051102.

[29] Mandel, J., 1964, The Statistical Analysis of Experimental Data, Dover Publications, Inc., New York.

[30] Riley, K. F., Hobson, M. P., and Bence, S. J., 2002, "Mathematical Methods for Physics and Engineering," Cambridge University Press, Cambridge, United Kingdom.

[31] Nishi, M., Matsunaga, S., Okamoto, M., Uno, M., and Nishitani, K., 1988, "Measurements of Three-Dimensional Periodic Flow in a Conical Draft Tube at Surging Condition," Flows in Non Rotating Turbomachinery Components, FED, 69, pp. 81–88.

[32] Susan-Resiga, R., Muntean, S., Stein, P., and Avellan, F., 2009, "Axisymmetric Swirling Flow Simulation of the Draft Tube Vortex in Francis Turbines at Partial Discharge," Int. J. Fluid Mach. Syst., 2(4), pp. 295–302.

[33] Muntean, S., Susan-Resiga, R. F., and Bosioc, A. I., 2009, "3D Numerical Analysis of Unsteady Pressure Fluctuations in a Swirling Flow Without and With Axial Water Jet Control," Proceedings of the 14th International Conference on Fluid Flow Technologies (CMFF'09), Budapest, Hungary, Vol. 2, pp. 510–518.

[34] Zhang, R., Mao, F., Wu, J., Chen, S., Wu, Y., and Liu, S., 2009, "Characteristics and Control of the Draft-Tube in Part-Load Francis Turbine," ASME J. Fluids Eng., 131(2), p. 021101.

[35] Koutnik, J., Krüger, K., Pochyly, F., Rudolf, P., and Haban, V., 2006, "On Cavitating Vortex Rope Form Stability During Francis Turbine Part Load Operation," IAHR International Meeting of the Workgroup on Cavitation and Dynamic Problems in Hydraulic Machinery and Systems, Barcelona, Spain.

[36] Benjamin, T., 1962, "Theory of Vortex Breakdown Phenomenon," J. Fluid Mech., 14, pp. 593–629.

[37] Tanasa, C., Bosioc, A. I., Muntean, S., and Susan-Resiga, R., 2011, "Flow-Feedback Control Technique for Vortex Rope Mitigation From Conical Diffuser of Hydraulic Turbines," Proc. Rom. Acad., Ser. A, 12(2), pp. 125–132.

Constantin Tănasă
Scientific Researcher
Research Center for Engineering of
Systems With Complex Fluids,
"Politehnica" University of Timişoara,
Boulevard Mihai Viteazu 1,
RO-300222 Timişoara, Romania
e-mail: costel@mh.mec.upt.ro

Romeo Susan-Resiga[1]
Professor
Hydraulic Machinery Department,
"Politehnica" University of Timişoara,
Boulevard Mihai Viteazu 1,
RO-300222 Timişoara, Romania
e-mail: resiga@mh.mec.upt.ro

Sebastian Muntean
Senior Researcher
e-mail: seby@acad-tim.tm.edu.ro

Alin Ilie Bosioc
Scientific Researcher
e-mail: alin@mh.mec.upt.ro

Center for Advanced Research in
Engineering Science,
Romanian Academy—Timişoara Branch,
Boulevard Mihai Viteazu 24,
RO-300223 Timişoara, Romania

Flow-Feedback Method for Mitigating the Vortex Rope in Decelerated Swirling Flows

When reaction hydraulic turbines are operated far from the design operating regime, particularly at partial discharge, swirling flow instability is developed downstream of the runner, in the discharge cone, with a precessing helical vortex and its associated severe pressure fluctuations. Bosioc et al. (2012, "Unsteady Pressure Analysis of a Swirling Flow With Vortex Rope and Axial Water Injection in a Discharge Cone," ASME J. Fluids Eng., 134(8), p. 081104) showed that this instability can be successfully mitigated by injecting a water jet along the axis. However, the jet discharge is too large to be supplied with high pressure water bypassing the runner, since this discharge is associated with the volumetric loss. In the present paper we demonstrate that the control jet injected at the inlet of the conical diffuser can actually be supplied with water collected from the discharge cone outlet, thus introducing a new concept of flow feedback. In this case, the jet is driven by the pressure difference between the cone wall, where the feedback spiral case is located, and the pressure at the jet nozzle outlet. In order to reach the required threshold value of the jet discharge, we also introduce ejector pumps to partially compensate for the hydraulic losses in the return pipes. Extensive experimental investigations show that the wall pressure fluctuations are successfully mitigated when the jet reaches 12% of the main flow discharge for a typical part load turbine operating regime. About 10% of the jet discharge is supplied by the plain flow feedback, and only 2% boost is insured by the ejector pumps. As a result, this new approach paves the way towards practical applications in real hydraulic turbines. [DOI: 10.1115/1.4023946]

Keywords: decelerated swirling flow, vortex rope, flow-feedback method, experimental investigations, unsteady pressure analysis

1 Introduction

Hydropower remains the main option for regulating power grids, whereas other renewable energy sources, such as wind, introduce power fluctuations [1]. However, Francis hydraulic turbines are designed to operate at, or in the neighborhood of, the best efficiency regime. Far from such optimal regime, hydraulic turbine operation is hindered by unwanted flow instabilities, with associated low-frequency phenomena developed in swirling flows [2]. For example, at partial discharge the self-induced instability of the decelerated swirling flow downstream the runner, in the discharge cone, with precessing helical vortex (also known as vortex rope), is accompanied by severe pressure fluctuations [3,4] leading to: (i) failure of the draft tube connecting bolts [5], (ii) removal of the runner hub cone due to the rupture of connecting bolts [6], (iii) breakdown of runner blades [7], (iv) damage of labyrinth seal, and (v) nonuniform wear of the bearings.

Conventionally, the characteristic length for hydraulic turbines is the runner diameter (marked with D in Fig. 1) according to the IEC standards [8]. Francis runner prototype diameters are typically in the range from 2 to 10 m while the associated Reynolds number ranges from 10^7 to 10^8, Anton [9]. Generally, extensive experimental investigations are performed on hydraulic turbines models in the laboratory. Correspondingly, runner model diameters are within range from 0.25 m up to 0.5 m, with Reynolds number values from 10^5 to 10^6.

Mitigating the vortex rope phenomenon is an open problem for modern Francis hydraulic turbines, with a plethora of techniques aimed either at removing the causes of flow instability or at dimin-

ishing its effects. Such techniques can be categorized as either active or passive [10], depending on the energy injected in the main flow. An early review of passive technical solutions that address hydraulic instabilities in the draft tubes of hydraulic turbines was compiled by Thicke [11], and later on, various methodologies have been developed up to their technical application: (i) air admission [12,13] (ii) stabilizer fins [14] (iii) runner cone extensions [15,16] (iv) J-grooves [17,18]. Although such techniques led to significant improvements in turbine operation at far off-design regimes, fins, cones, or grooves cannot be removed when their presence is no longer required, thus introducing unwanted additional hydraulic losses when operated in the neighborhood of the best efficiency regime. The air admission is self-adjusting with the operating point, however the large air pocket significantly changes the overall impedance of the hydraulic system, and it may trigger even larger problems than the original ones in case resonance occurs.

Active flow control methods generally use either air or water injection, using an external energy source, such as: (i) air injection at the trailing edge of the wicket gates [12] (ii) water injection at the trailing edge of the wicket gates [19] (iii) tangential water jet injection at the cone wall [20] (iv) axial water jet injection with high velocity and low discharge [21] (v) water jet injected along the axis with low velocity and large discharge [22] (vi) two-phase air-water jet injection along the axis [23]. Beside such methods aimed at modifying the hydrodynamics of the flow, Blommaert et al. [24] and Blommaert [25] attempted to alter hydro acoustic properties by injecting in the draft tube cone an inverse modulated jet carrying up to 1% of the overall turbine power, with the purpose of canceling out the self-induced pressure fluctuations caused by the vortex rope.

The above analyses clearly show that an effective swirling flow control technique should address the main cause of the self-induced instability rather than the effects of a well-developed precessing vortex rope. As a result, Susan-Resiga et al. [26]
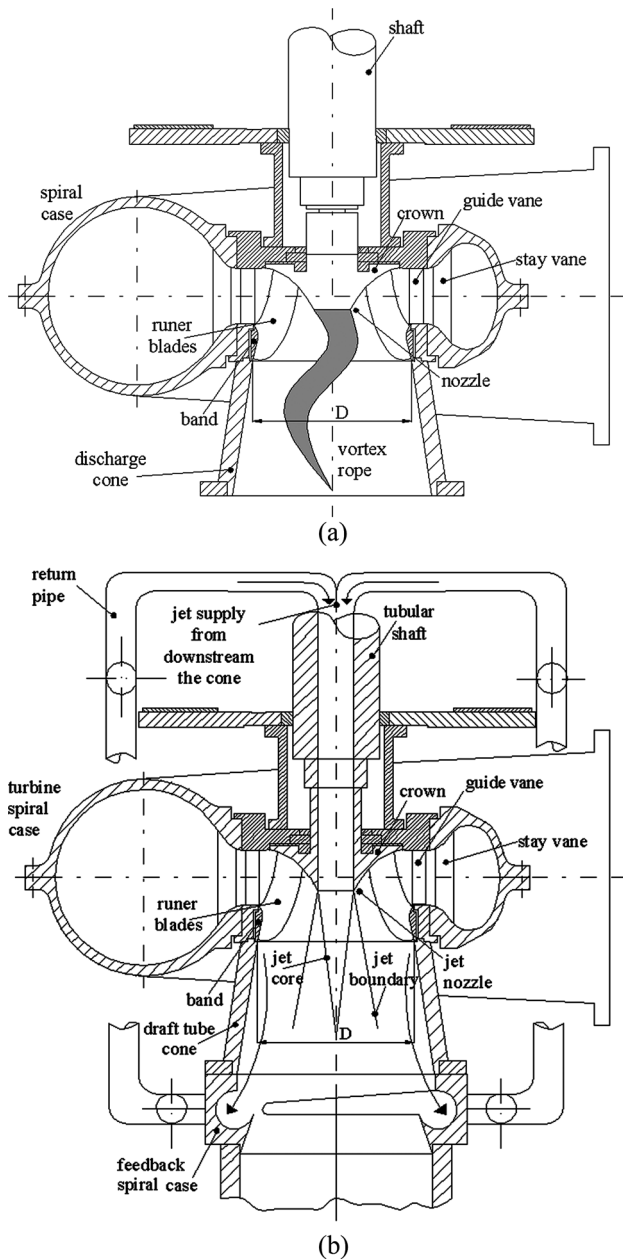
Fig. 1 Cross section through a Francis hydraulic turbine (a) vortex rope in the discharge cone and (b) flow-feedback system with jet injection into the discharge cone

introduced a novel technique for stabilizing the decelerated swirling flow in the discharge cone of hydraulic turbines operated at partial discharge, which uses a water injection from the runner crown along machine axis. The initial proof of concept was performed for a Francis turbine operated at partial discharge, with a well-developed vortex rope [4] as sketched in Fig. 1(a). It was shown, that the vortex rope can be practically removed by injecting a water jet from the runner crown, thus eliminating harmful pressure fluctuations as well. Numerical assessment of this approach was later on performed by Zhang et al. [27], who confirmed the effectiveness of vortex rope mitigation. Further extensive experimental investigations of the control jet parameters were performed by Bosioc et al. [22], who showed that a jet discharge of 10% to 12% from the turbine discharge is required to completely remove the vortex rope. From a practical viewpoint, these investigations raised a new issue regarding the supply of the control jet. A simple approach is to supply the control jet with

high pressure water from upstream the runner. As a result, a large fraction of the turbine discharge will bypass the runner, with an inacceptable increase of the so-called volumetric losses. An alternative approach is, to supply the control jet by collecting a fraction of the discharge from downstream the runner at the discharge cone outlet, Fig. 1(b), by installing a small spiral collecting case connected through return pipes to the turbine tubular shaft and the jet nozzle. It is clear that in this case no additional volumetric losses occur, and no additional energy is required to drive the control jet. The first numerical experiments for this passive flow-feedback method (FFM) were performed by Susan-Resiga and Muntean [28] who showed that the pressure excess at the discharge cone wall, mainly due to the swirl, with respect to the pressure deficit at the runner crown tip, could drive the control jet to completely mitigate the quasi-stagnant region induced by the vortex rope. Moreover, the FFM approach has the potential to actually increase the overall turbine efficiency by reducing the rather large hydraulic losses in the draft tube at off-design operating points. Qualitatively, the FFM is self-regulated, since the pressure difference that drives the control jet decreases near the best efficiency regime, thus reducing or cancelling the jet discharge when it is no longer needed. This preliminary assessment of the FFM did not fully account for the hydraulic losses on the return circuit. As a result, the experimental investigations presented in this paper also considered an active flow feedback method with additional energy (FFM+) provided by ejector pumps installed on the return pipes. Both control methods are investigated using the methodology presented by Bosioc et al. [22]. Moreover, the experimental results of the FFM are compared against the plain water injection method investigated in [22] in order to assess as clear as possible the FFM advantages and limitations.

The second section presents the experimental test rig used for the present experimental investigations of both FFM and FFM+, with a swirl generator that provides a swirling flow similar to the one encountered in hydraulic turbines operated at partial discharge, where a well-developed vortex rope is present in the discharge cone. The experimental setup for pressure measurements is also detailed in Sec. 2. An extensive analysis of both steady (pressure recovery) and unsteady (pressure fluctuations) pressure on the conical diffuser wall is presented in Sec. 3. The paper conclusions are summarized in Sec. 4.

2 Experimental Setup

2.1 Swirling Flow Apparatus and Pressure Measuring Setup. In order to investigate experimentally the flow-feedback control, we are using the test rig with a closed loop hydraulic circuit described in [22]. Instead of testing the FFM on a model hydraulic turbine, we have designed and built a special swirl apparatus, Fig. 2. The swirling flow apparatus, included in the main hydraulic circuit, contains two main parts: the swirl generator and the convergent-divergent test section. The swirl generator has an upstream annular section with stationary and rotating blades for generating a swirling flow. It has three components: the ogive, the guide vanes, and the free runner, see the detail in Fig. 2. The ogive with four leaned struts sustains the swirl generator and supplies the jet nozzle. The guide vanes and the free runner are installed in a cylindrical section with $D_s = 150$ mm. The nozzle outlet with $D_n = 30$ mm is located close to the throat section with $D_t = 100$ mm. This swirl generator provides a swirling flow configuration at the inlet of the conical diffuser quite similar to the corresponding flow downstream a Francis runner operated at partial discharge [29]. As a result, the decelerated swirling flow in the cone develops a precessing vortex rope with the same Strouhal number as the one corresponding to the Francis turbine model investigated in [4]. The flow in this swirling flow apparatus was extensively investigated numerically by Ojima and Kamemoto [30], Bergman [31], and Petit et al. [32], who clearly
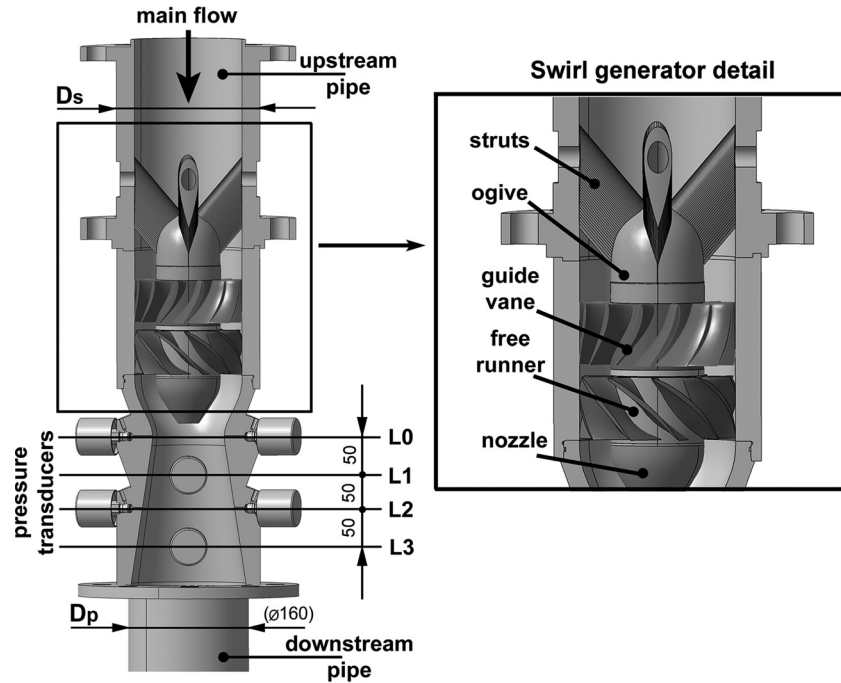
Fig. 2 Cross section through the swirling flow apparatus and detail of the swirl generator

showed the well-developed vortex rope in agreement with the experimental investigations performed on our test rig.

The present paper is focused on the wall pressure measurements on the conical diffuser, using a set of eight fast responding transducers to measure the unsteady pressure at four levels in the cone, L0, L1, L2, and L3, as shown in Fig. 2. The L0 level corresponds to the throat of the convergent-divergent test section, and the next three levels are located downstream with 50 mm spacing. Each pressure tap with a diameter of 3 mm was manufactured with misalignment in the limit of ±0.1 mm on the cone wall using a CNC machine.

The cone half-angle is 8.6 deg, similar to the compact discharge cones used in the modern draft tubes for hydraulic turbines. However, in our case the ratio between the cone length ($L = 200$ mm) and the throat diameter ($D_t = 100$ mm) is quite large ($L/D_t = 2$) in order to capture the entire vortex rope in the conical diffuser. The capacitive unsteady pressure transducers, flush-mounted on the cone wall, have an accuracy of ±0.13% within a full range of ±100 kPa. At least ten data sets have been acquired for each investigated flow regime in order to insure data reliability. Each set corresponds to an acquisition time interval of 32 s at a sampling rate of 256 samples per second. Given a fundamental frequency $f = 15$ Hz associated with the vortex rope, we have more than 17 samples per period, which ensures a good resolution for the unsteady signal. The standard deviation for measured values is less than ±1% for all pressure transducers. The uncertainty is computed taking into account the systematic and random errors [33,34], respectively.

Most of the results have been obtained for a test rig discharge of $Q = 30$ l/s, but the scaling of the results was checked with respect to the dimensionless pressure coefficients at 25 and 20 l/s. The flow meter accuracy installed on the test rig is ±0.15% of the full range of 50 l/s. The Reynolds number of 3.8×10^5 corresponds to our investigation on the test rig, taking into account the main discharge of $Q = 30$ l/s in the throat section with $D_t = 100$ mm.

The experimental investigations have been performed with a water temperature distribution from 20 to 25 °C during each campaign. In this case, no cooling system was used due to the fact that the water volume is large enough (more 4 m³) in order to have negligible uncertainties due to the temperature variations. Also,

all experimental investigations, have been done under overpressure conditions. Moreover, the hydraulic circuit is fully filled with water. As a result, only noncavitating vortex ropes were considered in our investigations, meaning no air volume trapped inside. That is the reason, why the density was taken constant and equal with the water density value ($\rho = 998$ kg/m³).

2.2 The Passive Flow Feedback Method Implementation. The flow-feedback system implemented on our swirl apparatus is sketched in Fig. 3. Essentially, we have added a twin spiral case at the cone outlet to collect a fraction of the discharge, which is directed through a pair of return pipes towards the jet nozzle. Note, that in our previous investigations [22] we have used an auxiliary pump to supply the jet, while here the jet is simply driven by the pressure difference from the cone wall and the jet nozzle exit without any external energy. For FFM implementation, the auxiliary pump was completely removed.

The main component of the FFM system is the twin spiral case shown in Fig. 4. We have considered a circular cross section, with a linear cross-section area increase versus the angular coordinate resulting in a cross-section radius variation as shown in Fig. 4(a). The corresponding design is shown in Fig. 4(b), with geometrical details given in Fig. 4(c) for several meridian cross sections. The inlet and outlet diameters are the same, $D_{inlet} = D_{outlet} = 160$ mm, the tongue diameter is $D_{tongue} = 150$ mm, and the axial extent of the twin spiral case is $H = 70$ mm. A transversal cross-section view of the twin spiral case is shown in Fig. 4(d). This particular design was chosen such that the radial extent of the spiral case is minimized, as required for the practical implementation in real power plants. Two 30 mm diameter and 600 mm length return pipes connect the spiral case outlets to the jet nozzle, see Fig. 3. Note, that in this straightforward implementation of the FFM there are no elements to regulate the jet discharge.

2.3 The Active FFM+ Implementation. During the experimental investigations we have found that the hydraulic losses through the flow return pipes are slightly larger than initially estimated. As a result, the jet discharge was found to be slightly lower than the threshold value required for effective vortex rope
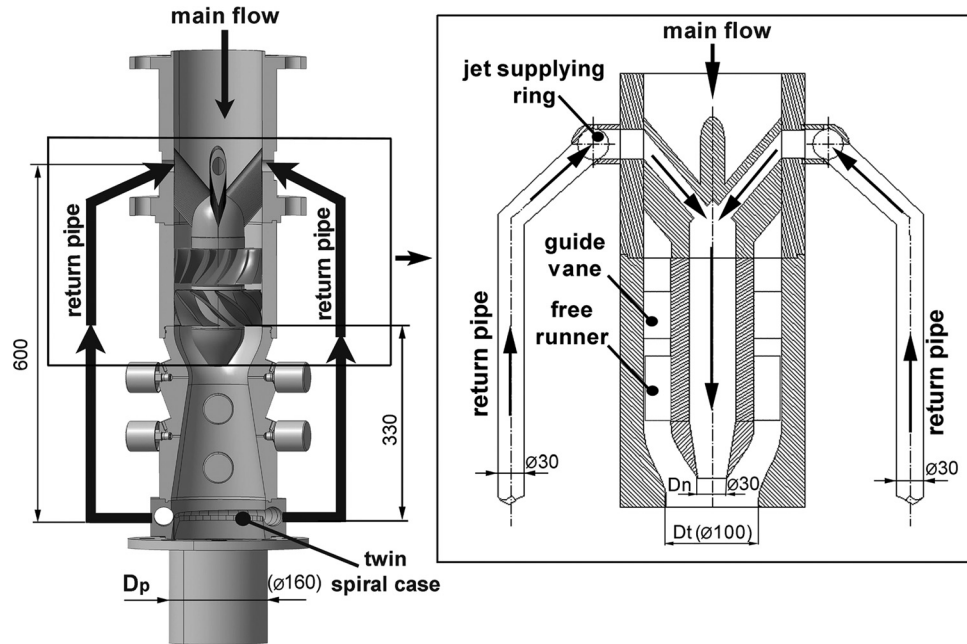
Fig. 3 Schematic representation of the flow-feedback system (FFM) implemented on the swirl apparatus and a cross section through the swirl generator
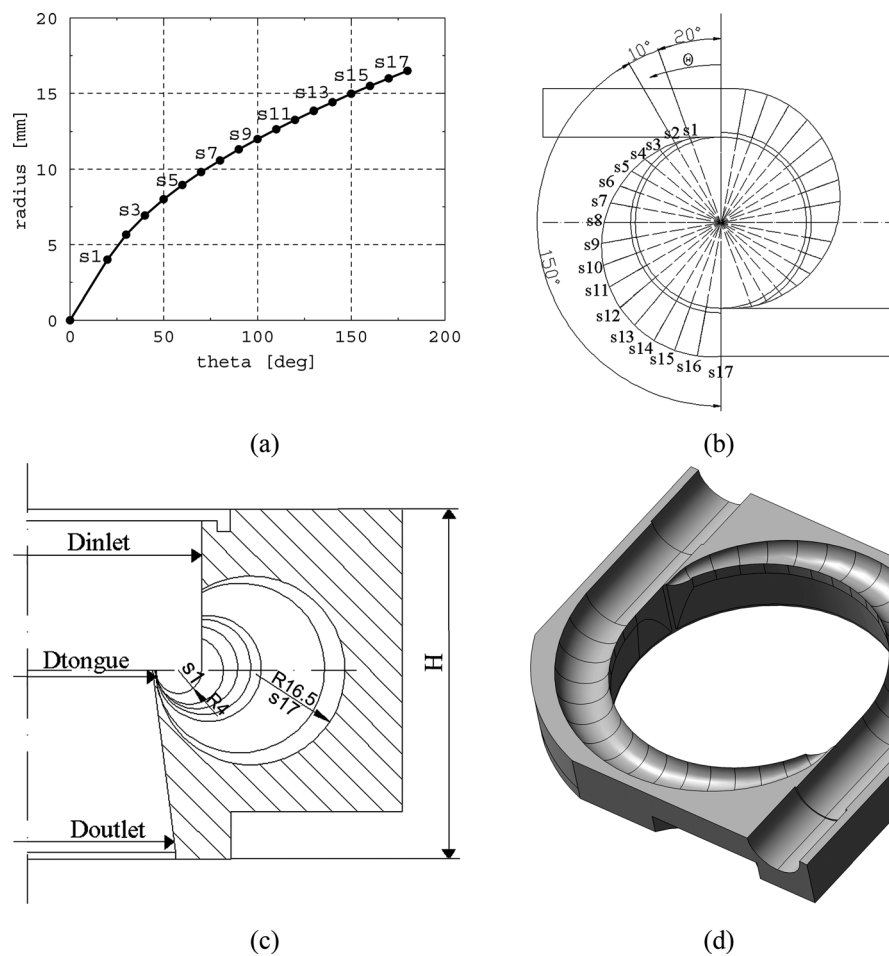

(a)

(b)

(c)

(d)

Fig. 4 Collecting spiral case (*a*) radius of the cross section, (*b*) top view of the twin spiral case, (*c*) meridian cross-section geometry, and (*d*) transversal cross-section
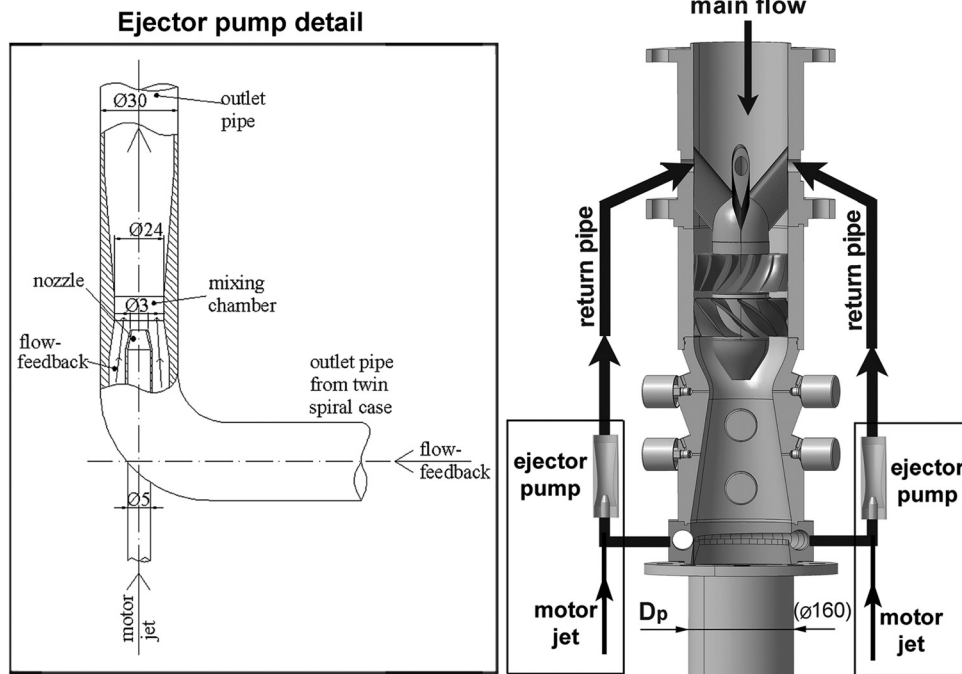
Fig. 5 Flow-feedback system with ejector pumps (FFM+) and a detail with the ejector pump
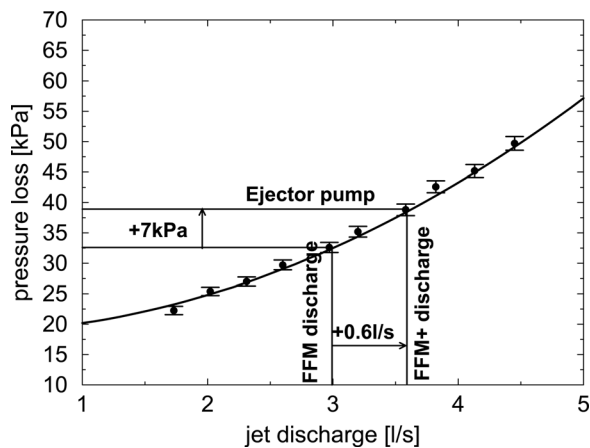

Fig. 6 Pressure loss on the return pipes versus jet discharge

mitigation [35]. In order to provide the necessary jet discharge increase, we have designed and installed two elbow ejector pumps, Fig. 5, on the return pipes. By measuring the pressure loss versus the jet discharge, Fig. 6, we have determined the pressure rise required for the ejector pumps. The actual design of the ejector pump follows the classical methodology [36], with an estimated efficiency of 36%. Although this efficiency is rather low, the simplicity and robustness of the ejector, correlated with the small amount of hydraulic energy required for the driving jet, recommends this technical solution for real practical applications as well. On our test rig, the ejector driving jets are supplied with an auxiliary pump, but, for real turbines these driving jets could be supplied with high pressure water from upstream the turbine. The required discharge, included in the overall volumetric losses, is no larger than from 1% to 2% of the turbine discharge.

3 Pressure Data Analysis

3.1 Mean Pressure Analysis. The main purpose of the discharge cone is to convert the excess of kinetic energy at the runner
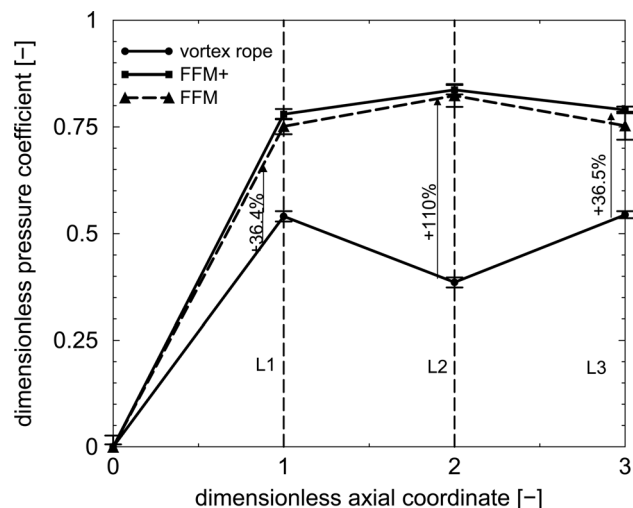

Fig. 7 Dimensionless pressure coefficient measured on the conical diffuser wall for swirling flow with vortex rope and with flow-feedback control, respectively

outlet into static pressure by decelerating the swirling flow downstream the hydraulic turbine runner. In practice, this dynamic-to-static pressure conversion is quantified by the so-called pressure recovery coefficient, usually evaluated with the wall pressure. The wall pressure evolution is expressed in dimensionless form with the pressure coefficient,

$$c_p = \frac{\overline{p} - \overline{p}_{L0}}{\rho V_t^2 / 2} \quad \text{where} \quad V_t = \frac{Q + Q_{\text{jet}}}{\pi D_t^2 / 4} \quad (1)$$

where $\overline{p}_{L0}$ is the mean pressure measured by the transducers at the L0 level, Fig. 2, $\overline{p}$ is the mean pressure measured further downstream on the cone wall, ρ is the water density, and V_t is the throat average discharge velocity with $D_t = 100$ mm the throat diameter of the swirl apparatus at level L0, respectively. The pressure coefficient defined in Eq. (1) is plotted in Fig. 7 for the levels L1, L2,
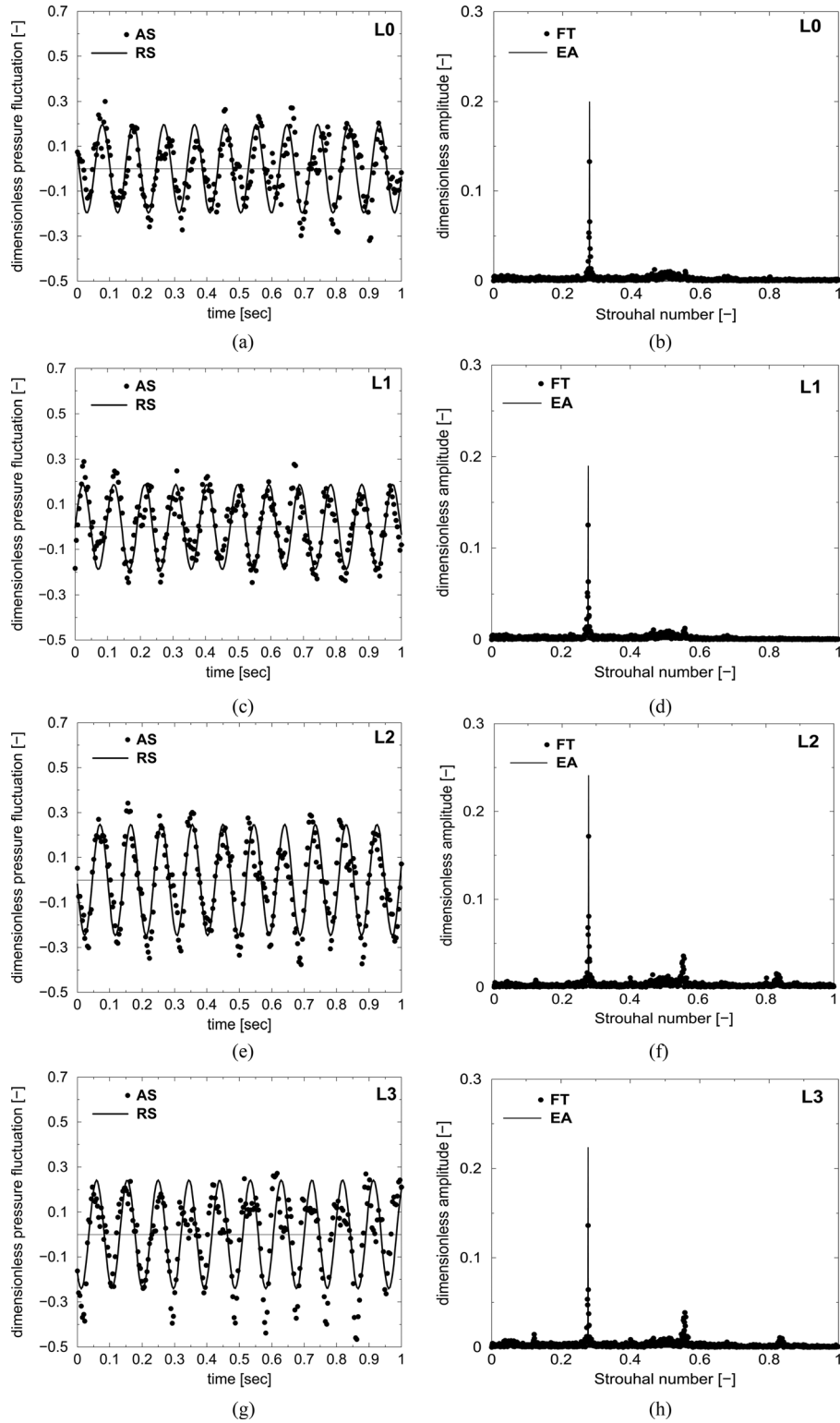
Fig. 8 Pressure fluctuation when using the FFM: original signal (left) and its Fourier spectrum (right)

and L3, where the axial coordinate is made dimensionless by the throat radius. The measurements were repeated $N > 10$ times for each operating regime, and the standard deviation for the measurement set,

$$\sigma = \sqrt{\frac{\sum (p_i - \bar{p})^2}{N - 1}} \qquad (2)$$

is shown in Fig. 7 with error bars. One can easily observe a significant increase in the pressure recovery when we inject the control jet. For example, in the middle of the conical diffuser, level L2, the wall pressure recovery coefficient is practically doubled. It is clear that by mitigating the vortex rope and the associated additional hydraulic losses, the dynamic-to-static pressure conversion is more efficient. For real turbines, this improved pressure recovery in the discharge cone is reflected in an increase of the overall
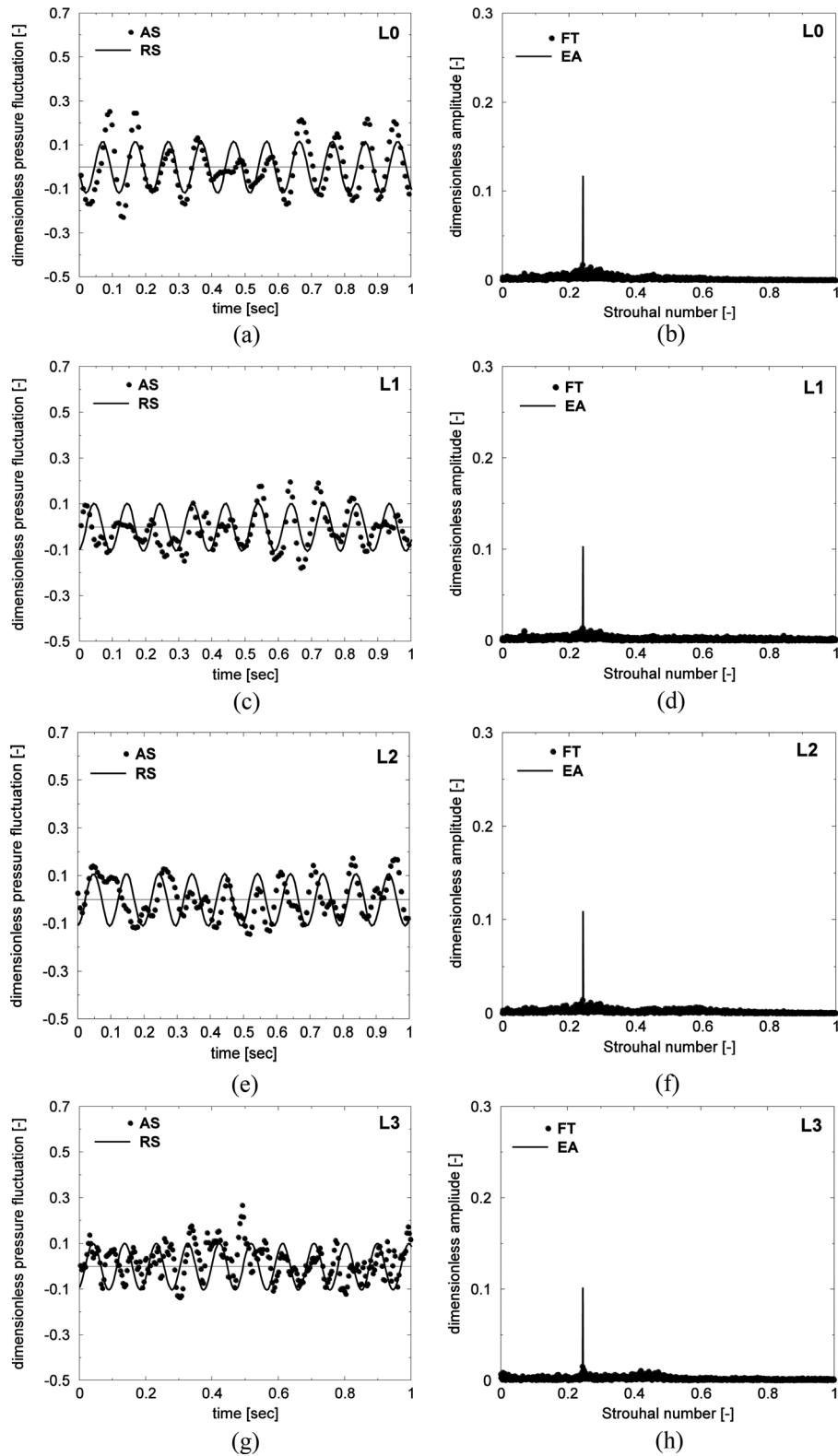
Fig. 9 Pressure fluctuation when using the FFM+: original signal (left) and its Fourier spectrum (right)

turbine efficiency far from the best efficiency point, especially for low-head hydraulic turbines, since the main fraction of the hydraulic losses at such operating points are associated with the swirl in the draft tube cone [37]. At the L1 level, the pressure recovery increases from 0.55 to 0.75 (+36.4%), and a similar increase is recorded at the L3 level.

The control jet discharge is 10% from the main flow discharge for FFM, and 12% for FFM+ when the ejector pumps are turned on. From the pressure recovery perspective, the small increase in the jet discharge leads to a corresponding small improvement in the diffuser performance. However, from a dynamic point of view, there is a significant improvement, as shown below.

The analysis of the mean pressure evolution along the cone wall shows, that the jet injection with the flow-feedback method has the potential to significantly improve the pressure recovery in compact conical diffusers (with an angle larger than 13 deg [38]) when the hydraulic turbine is operated far from the best efficiency point.

3.2 Unsteady Pressure Analysis. The self-induced flow instability of the decelerated swirl in a conical diffuser develops a precessing helical vortex with an associated pressure fluctuation which hinders the hydraulic turbine operation. This is the reason, why we focus in the present section on the unsteady part of the pressure measurements, as well as on the effect of the flow-feedback on the pressure fluctuation level.

Since the unsteady part of the pressure signal is periodic, we characterize it using the vortex rope precessing frequency, f (Hz), and the equivalent amplitude computed using Parseval's theorem [39]. In dimensionless form, the precessing frequency is expressed using the Strouhal number,

$$\text{Sh} = f \frac{D_t}{V_t} \tag{3}$$

and the pressure pulsation amplitude is

$$A \equiv \frac{\sqrt{2} p_{\text{RMS}}}{\rho V_t^2 / 2} \tag{4}$$

Note, that according to Parseval's theorem, the equivalent pressure fluctuation amplitude is $\sqrt{2} p_{\text{RMS}}$, whereas p_{RMS} is the random mean square of the fluctuating part of the pressure signal.

For Eq. (4), we practically approximate the periodic signal with a sinusoidal one, but the equivalent amplitude (EA) correctly accounts for the whole energy content of the signal. This one-harmonic approximation is labeled "reconstructed signal" (RS). One can see from Figs. 8 and 9 that the reconstructed signal captures the main characteristics of the acquired signal (AS), as shown in [22] for the pressure fluctuations generated by the vortex
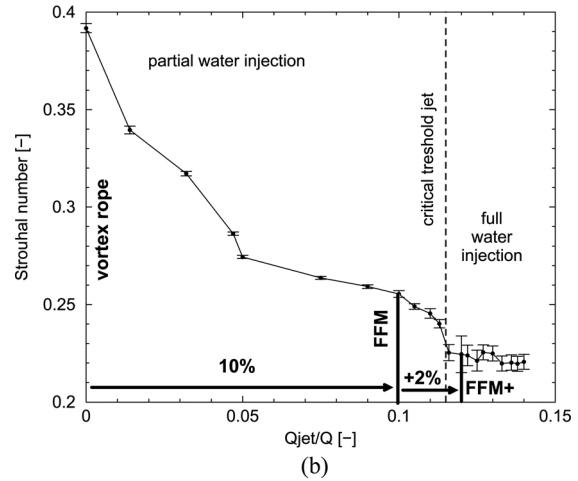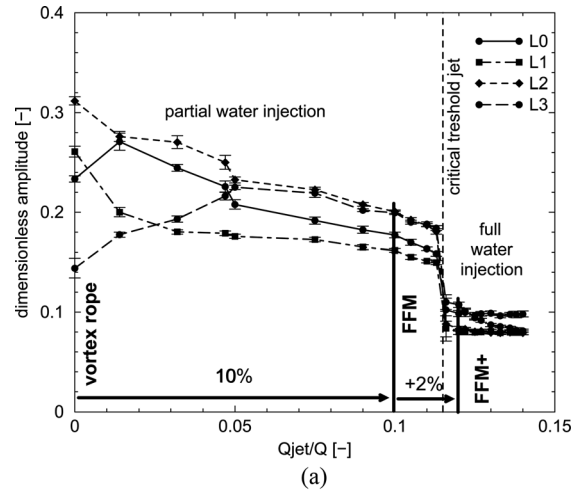

Fig. 10 Dimensionless amplitude (*a*) Strouhal number and (*b*) versus the jet discharge fraction presented by Bosioc et al. [22]. FFM and FFM+ are marked on both figures.
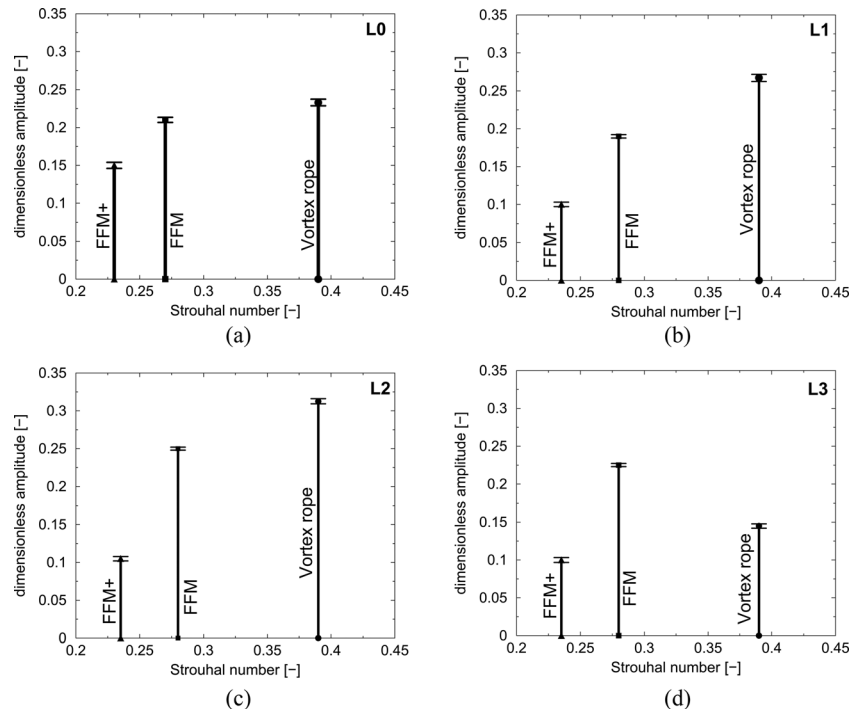

Fig. 11 Mitigation of the pressure fluctuations using FFM and FFM+ with respect to the vortex rope case at the four levels shown in Fig. 2
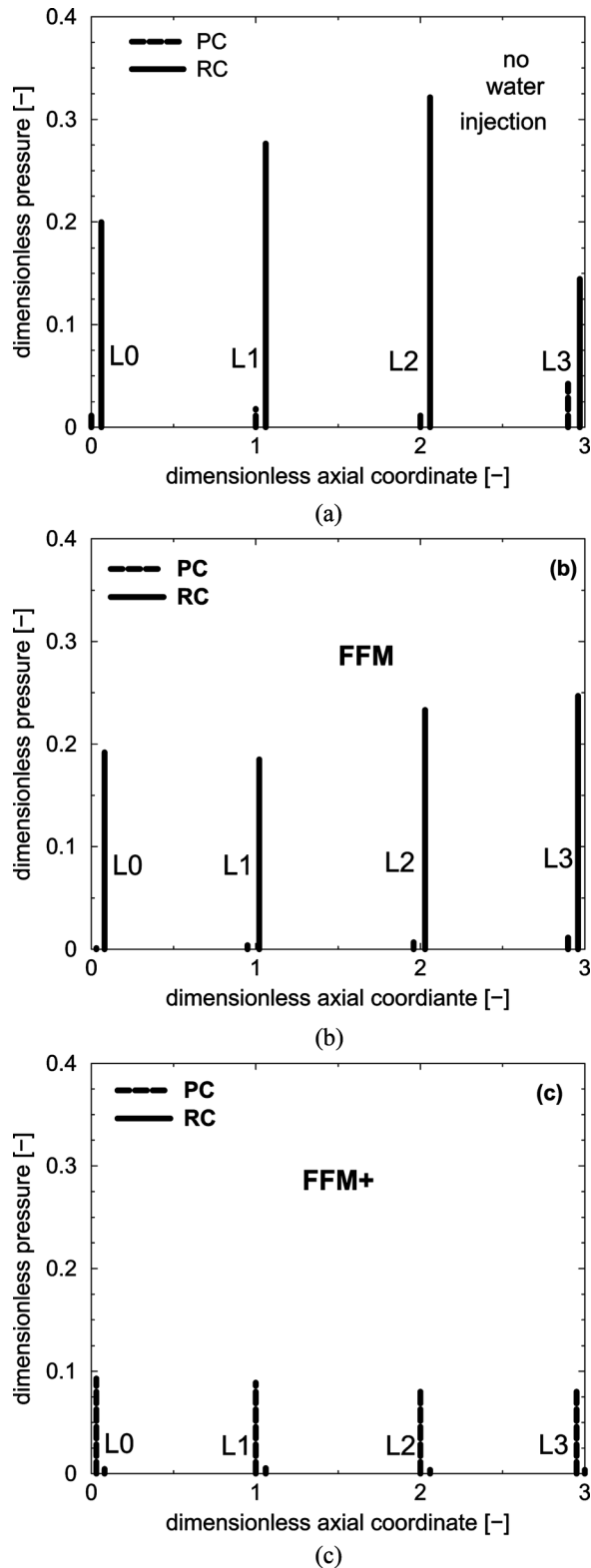
(a)

(b)

(c)

Fig. 12   Rotating and plunging pressure fluctuation decomposition for swirling flow with vortex rope (*a*), FFM (*b*), and FFM+ (*c*), respectively, at the four levels shown in Fig. 2

rope, even if higher order harmonics are present in the original signal. A more accurate and detailed analysis would involve the phase-averaging of the pressure fluctuations, but this is beyond the scope of the present investigations.

Let us now examine the cause of the significant pressure pulsation reduction displayed in Fig. 9, in comparison with Fig. 8, which in turn is significantly lower than the corresponding level measured without flow control ([22], Fig. 7). Figure 10 recalls the decrease in both amplitude and frequency of the pressure fluctuation measured by Bosioc et al. [22] at the L0–L3 levels of the conical diffuser, with the increase in the relative control jet discharge. When using the flow-feedback, either as FFM or as FFM+, there is no possibility to directly measure the jet discharge. As a result, we have estimated the jet discharge by comparing the velocity profile measured with laser Doppler velocimetry in two setups [35]: (i) the jet is supplied with an auxiliary pump, when the jet discharge is directly measured (ii) the jet is supplied through the flow-feedback return pipes. Using this approach, we found that when using the FFM the jet discharge is approximately 10% of the main flow discharge, while when the ejector pumps are turned on the FFM+ provides an additional 2% increase in the jet discharge. This rather small contribution of the ejector pumps allows the FFM+ to cross the threshold jet discharge, Fig. 10, thus providing a significant drop in both amplitude and frequency.

A synopsis of the pressure fluctuation mitigation is presented in Fig. 11. One can see that the water injection reduces the precession frequency, as well as the equivalent amplitude of the pressure fluctuations. Moreover, the flow-feedback with ejector pumps (FFM+) provides the largest amplitude reduction (up to 65%), while the Strouhal number decreases from 0.39 with vortex rope to 0.23 with FFM+. We conclude, that the flow feedback approach has the potential to effectively mitigate the pressure fluctuations in decelerated swirling flows with precessing vortex rope, while improving the pressure recovery as shown in Sec. 3.1.

3.3   Pressure Signal Decomposition. Jacob and Prenat [40] use the phase analysis of two simultaneously acquired pressure signals from transducers mounted on the discharge cone of a Francis turbine to discriminate between rotating and plunging oscillations, respectively. The rotating component (RC) of the unsteady pressure field is associated with the precessing vortex rope. As a result, the vortex rope is removed when the rotating component is negligible. On the other hand, the plunging oscillations correspond to the flow field oscillations in the whole hydraulic passage, and are generally propagated overall in the hydraulic system.

Figure 12 shows, that when the passive FFM is employed, and the jet discharge is lower than the threshold value, the pressure fluctuations correspond to the rotating unsteady pressure field, with negligible plunging components (PC). On the other hand, when using the FFM+ the jet discharge becomes larger than the threshold value, the vortex rope is practically eliminated, and the unsteady pressure field practically has only plunging oscillations. Although these plunging oscillations have amplitudes less than half the amplitude of the rotating oscillations, their potentially harmful effects must account the propagation in the whole hydraulic system. However, it is clear that the water injection practically changes the stability properties of the decelerated swirling flows, with respect to the capacity of sustaining or enhancing either asymmetric (rotating) or axisymmetric (plunging) perturbations.

4   Conclusions

The present paper introduces the novel flow-feedback approach for mitigating the instabilities of decelerated swirling flows. According to this approach, a water jet is injected along the machine axis, into the discharge cone of the hydraulic turbine, using a fraction of the discharge collected at the cone outlet. The passive flow feedback method (FFM) does not use any additional energy input, while the active version (FFM+) uses ejector pumps on the return pipes to increase the jet discharge.

We have performed extensive experimental investigations on both FFM and FFM+ implemented on a swirling flow apparatus which mimics the flow configuration encountered in a Francis

turbine operated at partial discharge. The main conclusions can be summarized as follows:

(i) Both, FFM and FFM+, significantly improve the pressure recovery in the conical diffuser by reducing the additional hydraulic losses.

(ii) Both, FFM and FFM+, decrease the pressure fluctuation amplitude and dominant frequency. However, since FFM+ provides a jet discharge larger than a threshold value, it practically removes the vortex rope. It is considered that the vortex rope is practically removed when the rotating component is negligible. The FFM+ leads to the same dynamical performance as the water injection method investigated by Bosioc et al. [22]. However, the main advantage of the FFM+ is that it requires only a 2% discharge for the ejector pumps motor jets in comparison to 12% discharge for the plain water jet injection. This aspect is important in engineering applications.

(iii) The FFM mitigates the vortex rope (decreases the pressure fluctuation amplitude and frequency) but leaves a rotating fluctuation of the flow field. On the other hand, the FFM+ completely removes the vortex rope, and leaves a residual plunging (axisymmetric) fluctuation, with much lower amplitude and frequency.

In our opinion, the above conclusions recommend the flow-feedback method to be considered for either new or refurbished hydraulic turbines to improve both efficiency and safety of the operation far from the best efficiency point.

Acknowledgment

Nomenclature

FFM = flow-feedback method
FFM+ = flow-feedback method with additional energy
AS = acquired signal
RS = reconstructed signal
FT = Fourier transform
EA = equivalent amplitude
PC = plunging component
RC = rotating component
Dt = reference diameter from the throat of the convergent-divergent test section, $D_t = 0.1(\text{m})$
f = dominant frequency (Hz)
Q = main discharge at the inlet of the test section (m^3/s)
Q_{jet} = jet discharge (m^3/s)
c_p = dimensionless pressure coefficient
n_i = value of a sample
$\bar{n}$ = mean value
N = number of measured samples
$\bar{p}$ = mean pressure (Pa)
p_{RMS} = root mean square of the pressure signal (Pa)
Sh = Strouhal number
Vt = reference velocity from the throat of convergent-divergent test section (m/s)
σ = standard deviation
ρ = density (kg/m^3)

References

[1] Wan, Y.-H., and Bucaneg, D., Jr., 2002, "Short-Term Power Fluctuations of Large Wind Power Plants," ASME J. Sol. Energy Eng., **124**(4), pp. 427–431.

[2] Dörfler, P., Sick, M., and Coutu, A., 2013, *Flow-Induced Pulsation and Vibration in Hydroelectric Machinery*, Springer, Berlin, Chap. 2.

[3] Wang, Z., and Zhou, L., 2006, "Simulations and Measurements of Pressure Oscillations Caused by Vortex Ropes," ASME J. Fluids Eng., **128**(4), pp. 649–655.

[4] Ciocan, G. D., Iliescu, M. S., Vu, T. C., Nennemann, B., and Avellan, F., 2007, "Experimental Study and Numerical Simulation of the FLINDT Draft Tube Rotating Vortex," ASME J. Fluids Eng., **129**(2), pp. 146–158.

[5] Casanova, F., 2009, "Failure Analysis of the Draft Tube Connecting Bolts of a Francis-Type Hydroelectric Power Plant," Eng. Fail. Anal., **16**(7), pp. 2202–2208,

[6] Baya, A., Muntean, S., Câmpian, V. C., Cuzmoş, A., Diaconescu, M., and Bălan, G., 2010, "Experimental Investigations of the Unsteady Flow in a Francis Turbine Draft Tube Cone," IOP Conf. Series: Earth Environ. Sci., **12**, p. 012007.

[7] Frunzaverde, D., Muntean, S., Marginean, G., Campian, V., Marsavina, L., Terzi, R., and Serban, V., 2010, "Failure Analysis of a Francis Turbine Runner," IOP Conf. Series: Earth Environ. Sci., **12**, p. 012115.

[8] International Electrotechnical Commission, 1999, *Hydraulic Turbines, Storage Pumps and Pumps-Turbines Model Acceptance*, 2nd ed., International Standard IEC No. 60193.

[9] Anton, I., 1979, *Hydraulic Turbines*, Facla Publishing House, Timisoara, Romania (in Romanian).

[10] Kral, L. D., 2000, "Active Flow Control Technology," ASME FED, Technical Brief, pp. 1–28.

[11] Thicke, R. H., 1981, "Practical Solutions for Draft Tube Instability," Water Power & Dam Construction, **33**(2), pp. 31–37.

[12] Papillon, B., Sabourin, M., Couston, M., and Deschenes, C., 2002, "Methods for Air Admission in Hydro Turbines," Proceedings of the 21st IAHR Symposium on Hydraulic Machinery and Systems, Lausanne, Switzerland, pp. 1–6.

[13] Qian, Z.-D., Yang, J.-D., and Huai, W.-X., 2007, "Numerical Simulation and Analysis of Pressure Pulsation in Francis Hydraulic Turbine With Air Admission," J. Hydrodyn., Ser. B, **19**(4), pp. 467–472.

[14] Nishi, M., Wang, X. M., Yoshida, K., Takahashi, T., and Tsukamoto, T., 1996, "An Experimental Study on Fins, Their Role in Control of the Draft Tube Surging," Proceedings of the 18th IAHR Symposium on Hydraulic Machinery and Cavitation, E. Cabrera, V. Espert, and F. Martinez, eds., Kluwer Academic Publishers, Dordrecht, The Netherlands, Vol. 2, pp. 905–914.

[15] Vevke, T., 2004, "An Experimental Investigation of Draft Tube Flow," Ph.D. thesis, Norwegian University of Science and Technology, Trondheim, Norway.

[16] Qian, Z. D., Li, W., Huai, W. X., and Wu, Y. L., 2012, "The Effect of the Runner Cone Design on Pressure Oscillation Characteristics in a Francis Hydraulic Turbine," Proc. IMechE, Part A: J. Power Energy, **226**(1), pp. 137–150.

[17] Kurokawa, J., Kajigaya, A., Matusi, J., and Imamura, H., 2000, "Suppression of Swirl in a Conical Diffuser by Use of J-Groove," Proceedings of the 20th IAHR Symposium on Hydraulic Machinery and Systems, Charlotte, NC, Paper No. DY-01, pp. 1–10.

[18] Kurokawa, J., Imamura, H., and Choi, Y.-D., 2010, "Effect of J-Groove on the Suppression of Swirl Flow in a Conical Diffuser," ASME J. Fluids Eng., **132**(7), p. 071101.

[19] Lewis, B. J., Cimbala, J. M., and Wouden, A. M., 2012, "Investigation of Distributor Vane Jets to Decrease the Unsteady Load on Hydro Turbine Runner Blades," IOP Conf. Series: Earth Environ. Sci., **15**, p. 022006.

[20] Kjeldsen, M., Olsen, K., Nielsen, T., and Dahlhaug, O., 2006, "Water Injection for the Mitigation of Draft Tube Pressure Pulsations," Proceedings of the 1st IAHR International Meeting of Working Group on Cavitation and Dynamic Problems in Hydraulic Machinery and Systems, Barcelona, Spain, pp. 1–11.

[21] Susan-Resiga, R., Muntean, S., Hasmatuchi, V., Anton, I., and Avellan, F., 2010, "Analysis and Prevention of Vortex Breakdown in the Simplified Discharge Cone of a Francis Turbine," ASME J. Fluids Eng., **132**(5), p. 051102.

[22] Bosioc, A. I., Susan-Resiga, R., Muntean, S., and Tănasă, C., 2012, "Unsteady Pressure Analysis of a Swirling Flow With Vortex Rope and Axial Water Injection in a Discharge Cone," ASME J. Fluids Eng., **134**(8), p. 081104.

[23] Kirschner, O., Schmidt, H., Ruprecht, A., Mader, R., and Meusburger, P., 2010, "Experimental Investigation of Vortex Control With an Axial Jet in the Draft Tube of a Model Pump-Turbine," IOP Conf. Series: Earth Environ. Sci., **12**, p. 012092.

[24] Blommaert, G., Prenat, J. E., Avellan, F., and Boyer, A., 1999, "Active Control of Francis Turbine Operation Stability," Proceedings of the 3rd ASME/JSME Joint Fluids Engineering Conference, San Francisco, CA, Paper No. FEDSM99-7210 3.

[25] Blommaert, G., 2000, "Étude du Comportement Dynamique des Turbines Francis: Contrôle Active de Leur Stabilité de Fonctionnement," Ph.D. thèse No. 2222, École Polytechnique Fédérale de Lausanne, Lausanne, Switzerland.

[26] Susan-Resiga, R., Vu, T. C., Muntean, S., Ciocan, G. D., and Nennemann, B., 2006, "Jet Control of the Draft Tube in Francis Turbines at Partial Discharge," Proceedings of the 23rd IAHR Symposium on Hydraulic Machinery and Systems, Yokohama, Japan, Paper No. F192, pp. 1–14.

[27] Zhang, R., Mao, F., Wu, J., Chen, S., Wu, Y., and Liu, S., 2009, "Characteristics and Control of the Draft-Tube Flow in Part-Load Francis Turbine," ASME J. Fluids Eng., **131**(2), p. 021101.

[28] Susan-Resiga, R., and Muntean, S., 2009, "Decelerated Swirling Flow Control in the Discharge Cone of Francis Turbines," Proceedings of the 4th International Symposium on Fluid Machinery and Fluid Mechanics (ISFMFE), Beijing, China, pp. 89–96.

[29] Susan-Resiga, R., Muntean, S., Tanasa, C., and Bosioc, A. I., 2008, "Hydrodynamic Design and Analysis of a Swirling Flow Generator," Proceedings of the 4th German-Romanian Workshop of Vortex Dynamics in Hydraulic Machinery, Stuttgart, Germany, pp. 1–16.

[30] Ojima, A., and Kamemoto, K., 2010, "Vortex Method Simulation of 3D and Unsteady Vortices in a Swirling Flow Apparatus Experimented in 'Politehnica' University of Timisoara," IOP Conf. Series: Earth Environ. Sci., **12**, p. 012065.

[31] Bergman, O., 2010, "Numerical Investigation of the Flow in a Swirl Generator Using OpenFOAM," M.S. thesis, Chalmers University of Technology, Goetenburg, Sweden.

[32] Petit, O., Bosioc, A. I., Nilsson, H., Muntean, S., and Susan-Resiga, R. F., 2011, "Unsteady Simulations of the Flow in a Swirl Generator Using OpenFOAM," Int. J. Fluid Mach. Syst., **4**(1), pp. 199–208.

[33] Abernethy, R. B., Benedict, R. P., and Dowdell, R. B., 1985, "ASME Measurement Uncertainty," ASME J. Fluids Eng., **107**(2), pp. 161–164.

[34] Moffat, R. J., 1982, "Contribution to the Theory of Single-Sample Uncertainty Analysis," ASME J. Fluids Eng., **104**(2), pp. 250–258.

[35] Tanasa, C., Bosioc, A. I., Susan-Resiga, R., and Muntean, S., 2012, "Experimental Investigations of the Swirling Flow in the Conical Diffuser Using Flow-Feedback Control Technique With Additional Energy Source," IOP Conf. Series: Earth Environ. Sci., **15**, p. 062043.

[36] Spiridonov, E. K., 2005, "Designing an Ejector Pump for a Hydraulic System for Discharging Water and Emptying Tanks," Chem. Petroleum Eng., **41**(1–2), pp. 66–74.

[37] Vu, T. C., and Retieb, S., 2002, "Accuracy Assessment of Current CFD Tools to Predict Hydraulic Turbine Efficiency Hill Chart," Proceedings of the 21st IAHR Symposium on Hydraulic Machinery and Systems, Lausanne, Switzerland, Vol. 1, pp. 193–198.

[38] Morel, L., 1983, "Potential for Reducing Kinetic Energy Losses in Low-Head Hydropower Installations," Technical Report No. 221, University of Minnesota, Minneapolis, MN.

[39] Riley, K. F., Hobson, M. P., and Bence, S. J., 2002, *Mathematical Methods for Physics and Engineering*, Cambridge University Press, Cambridge, UK, Chap. 12.8.

[40] Jacob, T., and Prenat, J., 1996, "Francis Turbine Surge: Discussion and Data Base," Proceedings of the 18th IAHR Symposium on Hydraulic Machinery and Cavitation, E. Cabrera, V. Espert, and F. Martinez, eds., Kluwer Academic Publishers, Dordrecht, The Netherlands, Vol. 2, pp. 855–865.

A variational model for swirling flow states with stagnant region

CrossMark

R.F. Susan-Resiga [a,b,*,1], S. Muntean [b,a,2], A. Stuparu [a,3], A.I. Bosioc [a,4], C. Tănasă [a,5], C. Ighişan [a,6]

[a] Politehnica University Timişoara, Bvd. Mihai Viteazu, No. 1, Timişoara, 300222, Romania
[b] Romanian Academy - Timişoara Branch, Bvd. Mihai Viteazu, No. 24, Timişoara, 300223, Romania

A B S T R A C T

We introduce a variational formulation for computing swirling flow states with stagnant regions in a pipe. The new extended flow force functional is maximized with respect to the location of the stagnant region boundary, leading to a swirling flow state with minimum swirl number. By allowing a jump in velocity across the vortex sheet that bounds the stagnant region, while the static pressure remains continuous, our variational principle does not require anymore additional kinematic conditions such as vanishing velocity. Solutions with or without velocity jump are naturally recovered. An assessment of the proposed model against experimental data is also presented.

© 2015 Elsevier Masson SAS. All rights reserved.

1. Introduction

The practical importance of swirling flows, and in particular the need for understanding and eventually controlling the local recirculation or extensive regions of reversed flow, periodic fluctuations in pressure and velocity, and high levels of kinetic energy dissipation, is clearly emphasized by Escudier [1]. The range of practical applications includes flame stabilization in furnaces, instabilities in the draft tube of hydraulic turbines, fluidic vortex valves, cyclones, etc.

There is a large body of literature dealing with such phenomena. However, in this paper we focus our investigations on the steady swirling flow configurations in confined axisymmetric geometries in order to identify the so-called base flows on which further stability analyses can be applied. Moreover, when focusing on the inertia-driven effects, the simplified hypothesis of an inviscid fluid is generally accepted for design, analysis and optimization methodologies.

Steady, axisymmetric swirling flow of an inviscid fluid is governed by a single second order partial differential equation, known as Bragg–Hawthorne [2], or Long [3]–Squire [4] equation, derived from the axisymmetric Euler equations.

The abrupt change which sometimes occurs in a swirling flow, known as *vortex breakdown* or *vortex bursting*, and in particular for the vortex formed at the leading edge of delta wings with large incidence, motivated Benjamin [5] to propose a theory analogous to the hydraulic jump in open channel flows as an alternative to the hypothesis that vortex breakdown is a manifestation of instability. Although Benjamin does not exclude that instability may be responsible for the disruption of many swirling flows in practice, the view he advocates for in [5] is that the explanation of the vortex breakdown phenomenon is outside the reach of conventional stability theory. This perspective was not generally accepted as Hall [6] concludes that "Benjamin's theory for finite-amplitude waves, and his analogy to hydraulic jump, are both inappropriate for describing the vortex breakdown". In this paper we propose an approach for predicting swirling flow states that hopefully meets Hall's [6] requirements to (i) have a high degree of explanatory power, (ii) deal with the interesting and relevant aspects of the problem, (iii) proceed from some simple, unifying idea, and (iv) have a high degree of refutability or testability.

Buntine and Saffman [7] study the Squire–Long equation for the case of diverging swirling flows and investigate the dependence of solutions on upstream and downstream boundary conditions, as well as on the pipe geometry, with the aim to understand how the vortex breakdown occurs. They show that the axial flow ceases to be unidirectional, so that breakdown can be inferred,

when a parameter measuring the relative magnitude of rotation and axial flow (Squire number) exceeds critical values. Moreover, for the simplified quasi-cylindrical model, they show that the axial velocity on the pipe centerline decreases as the Squire number increases, until a stagnation point occurs. Buntine and Saffman [7] state that further continuation of the solution cannot be performed due to the need for additional specifications of circulation and Bernoulli's functions on closed streamlines, or streamlines entering through downstream boundary. It is clear that this difficulty cannot be overcome as long as the flow is considered to occupy the whole pipe cross section.

This difficulty was solved by Keller et al. [8] by admitting that the flow may develop a central stagnant region, and as a result the axial velocity remains unidirectional in the remaining annular section. They consider an extension of Benjamin's variational principle by considering variable lower end points, and conclude that on the free surface bounding the stagnant region all velocity components vanish. This rather restrictive additional boundary condition is further used for solving the differential equation with a free boundary. An inverse Euler equation is developed to provide a differential equation in a fixed computational domain (with axial coordinate and streamfunction as independent variables, see also [9]) in order to incorporate the vanishing velocity condition on the free boundary. This initially one-dimensional approach has been further extended by Keller et al. [10] for the case of varying cross-sectional area. In spite of his initial work, Keller [11] later advocates for an ad-hoc extension of the circulation and Bernoulli's functions beyond the upstream interval of the streamfunction values, as vanishing circulation and constant total head. He recognizes that simple analytical extensions do not seem to lead to physical meaningful results. This approach was further employed by Elcrat et al. [12] to examine various axisymmetric vortex flows with swirl and shear. Other authors, e.g. Ortega-Casanova and Fernandez-Feria [13,14], pursue the simple choice of analytical continuation of circulation and Bernoulli's functions, thus obtaining various solutions for swirling flow in pipes with recirculation. However, they have a word of caution: "one should be cautious before drawing conclusions about the behavior (particularly breakdown) of swirling flow in pipes from the inviscid equations alone".

Goldshtik and Hussain [15] make a convincing case in favor of the stagnation zone model, without velocity jump, arguing that it excels the traditional analytic continuation method which leads to recirculation zones. Further [16], they show that an inviscid stagnation zone without a velocity jump at the boundary is stable to infinitesimal perturbations. That would imply that the stagnation zone could be replaced by a solid body because the no-slip conditions are fulfilled on its boundary without the boundary layer normally produced by such a no-slip condition.

Wang and Rusak [17] use the axisymmetric unsteady Euler equations to describe the dynamics of a swirling flow in a finite-length constant-area pipe. They conclude that the axisymmetric vortex breakdown phenomenon in inertia-driven (high-Reynolds number) flows is an evolution from an initial columnar swirling flow to another relatively stable equilibrium state which represents a flow around a separation zone. Their analysis employ the functional associated with the variational formulation introduced by Benjamin [5] and further used by Keller et al. [8], and perform an extensive global analysis of this functional in order to shed light on the development of a swirling flow in pipe. Further, Rusak et al. [18] argue that the fundamental characteristics which lead to vortex instability and breakdown in high-Reynolds-number flows may be calculated from considerations of a single, reduced order, nonlinear ordinary differential equation representing a columnar flow problem. This model is considered in the present paper in order to examine the swirling flow states in a pipe. However, our approach is different, more general, in the sense that we do not rely on rather restrictive conditions imposed on the velocity at the free boundary in order to find the free boundary location. In a recent study, Rusak et al. [19] examine equilibrium states of inviscid, axisymmetric swirling flows, and found that pipe divergence promotes the appearance of vortex breakdown to lower swirl ratios and delays wall separation, while pipe contraction delays the appearance of vortex breakdown to higher levels of swirl ratios but promotes wall-separation states. Although they employ the flow force functional for analysis purposes, the axial swirling flow states with possible stagnant regions are obtained by solving the one-dimensional Bragg–Hawthorne equation with additional velocity conditions at the free boundary. It is important to note, however, that they implicitly accept solutions with velocity jump (at least in the circumferential component) when considering stagnant regions near the wall.

Shtern et al. [20] identified a third alternative to the two main conjectures encountered in inviscid flow theories for axisymmetric swirling flow (inside the separation zone either the fluid stagnates or an analytical continuation of circulation and total head functions is considered). As summarized in [20], in the inviscid limit this alternative model reveals that: (i) both circulation and head functions have jumps at the boundary of separation zone, which contradicts the analytical continuation conjecture; (ii) there is no swirl in the separation zone, which seems to agree with the stagnation zone model; and (iii) the meridian flow in the separation zone is irrotational and it has the same magnitude as the flow outside the separation zone. However, Shtern et al. [20, §VII] advocate that their model is suitable for swirling jets while recognizing that for swirling flows in pipes both theoretical arguments [15,17] and experimental evidence are in favor of the stagnation model.

The present paper is proposing a new, more general, approach for finding swirling flow states in a pipe. We consider that, when necessary, the swirling flow naturally restrict itself within an annular region that occupies only a fraction of the whole geometrical cross-section available. The rest of the pipe section is occupied by stagnant region(s), bounded by free surfaces represented as vortex sheets. Across such a vortex sheet the velocity is allowed to have a jump, but the static pressure is continuous. The pressure continuity is required since a fluid interface in steady flow cannot support a pressure jump in normal direction. On the other hand, allowing a velocity jump does not necessary mean that the velocity components will always be discontinuous. As a matter of fact, solutions with continuous (vanishing) velocity are naturally recovered without imposing explicitly a kinematic condition on the free boundary. The present study does not include stability analysis of the vortex sheet.

Section 2 briefly revisit the Bragg–Hawthorne equation, with the boundary-value problem for the second order differential equation that governs swirling flow states (i.e. columnar flows). After recalling the flow-force functional introduced by Benjamin, we introduce the general stagnant region model with possible velocity jump at the free boundary, then we define the extended flow force functional that correctly accounts for the stagnant zone(s) contribution. Although Benjamin's flow force functional is minimized by the solution of the boundary value problem for the Bragg–Hawthorne equation, our extended flow force functional is maximized with respect to the free boundary(ies) location. This variational principle is shown to correspond, from physical point of view, to the rather intuitive minimization of the swirl number.

Section 3 is devoted to probably the simplest example of swirling flow, corresponding to constant circulation and total head. A full analytical analysis of the extended flow force behavior leads to a flow configuration with stagnant region, bounded by a vortex sheet, which minimizes the swirl number. However, in practice such axisymmetric swirling flow states may not be stable and can evolve in three-dimensional unsteady flows with precessing

helical vortex [21]. Nevertheless, we show that the singularity at the axis is naturally avoided by the presence of the stagnant region.

Section 4 deals with swirling flows where the circulation and Bernoulli's functions are considered as first order polynomials in the streamfunction. Since analytical solutions are available for the columnar Bragg–Hawthorne boundary value problems, we focus on examining solutions with stagnant region which emerge from the maximization of the flow force functional. We examine in detail swirling flows originating from a rigid body rotation with constant axial velocity, and we find solutions with stagnant region that minimize the swirl number even for angular speed values lower than the critical value. Moreover, for angular speed larger than the critical value we recover naturally the solutions with vanishing velocity at the boundary of the stagnant region, without explicitly imposing this condition.

In Section 5 we assess the rather simple model presented in Section 4 against experimental data for swirling flows downstream the runner of a hydraulic turbine model. While preserving the integral quantities corresponding to the volumetric flow rate and the circulation flux, we use a least squares method to fit the slopes of the circulation and Bernoulli's functions for best approximations of measured axial and circumferential velocity profiles. Although we have previously used these experimental data to validate a three-vortex empirical model [22], or a kinematically constrained swirling flow model [23], we show in this paper that the Bragg–Hawthorne equation augmented with a stagnant region model embedded in a novel variational formulation has the capability to consistently reproduce the main features of real swirling flows. The paper conclusions are summarized in Section 6.

2. Mathematical model for inviscid swirling flow

For high-Reynolds number flows, the steady, axisymmetric swirling flow model of inviscid and incompressible fluids is a reasonable approximation to examine inertia-driven phenomena.

Such flows are generally governed by the Euler equations (continuity and momentum) written in cylindrical coordinates (x, r, θ). The axial-symmetry hypothesis allows the use of the Stokes' streamfunction $\psi(x, r)$ to express the velocity field as,

$$v_x\hat{\boldsymbol{x}} + v_r\hat{\boldsymbol{r}} + v_\theta\hat{\boldsymbol{\theta}} = -\frac{\hat{\boldsymbol{\theta}}}{r} \times \nabla\psi + \frac{\hat{\boldsymbol{\theta}}}{r}\kappa(\psi), \tag{1}$$

where $\hat{\boldsymbol{x}}, \hat{\boldsymbol{r}},$ and $\hat{\boldsymbol{\theta}}$ are the unit vectors for the cylindrical coordinates, and $\kappa \equiv rv_\theta$ is the circulation function. Thanks to Kelvin's theorem, κ remains constant along a streamtube in steady flows, thus it depends only on the streamfunction, i.e. we have $\kappa(\psi)$.

The vorticity vector follows from (1),

$$\nabla \times \left(v_x\hat{\boldsymbol{x}} + v_r\hat{\boldsymbol{r}} + v_\theta\hat{\boldsymbol{\theta}}\right)$$

$$= \left(v_x\hat{\boldsymbol{x}} + v_r\hat{\boldsymbol{r}}\right)\frac{\mathrm{d}\kappa(\psi)}{\mathrm{d}\psi} + \left(\frac{\partial v_r}{\partial x} - \frac{\partial v_z}{\partial r}\right)\hat{\boldsymbol{\theta}}. \tag{2}$$

Since the meridian projection of the vorticity, first term in r.h.s. of (2), is aligned with the meridian velocity, it follows that the vorticity vector is tangent to the streamtube $\psi(x, r) = $ constant, [5].

In the case of steady, axisymmetric swirling flows of inviscid and incompressible fluids the Euler equations collapse into a single partial differential equation, known as the Bragg–Hawthorne equation, Bragg and Hawthorne [2], or Long–Squire equation, Long [3], Squire [4],

$$\nabla \cdot \left(\frac{\nabla\psi}{r^2}\right) + \frac{\kappa(\psi)}{r^2}\frac{\mathrm{d}\kappa(\psi)}{\mathrm{d}\psi} - \frac{\mathrm{d}h(\psi)}{\mathrm{d}\psi} = 0, \tag{3}$$

where $h \equiv p + v^2/2$ is the Bernoulli function, with $v^2 = v_x^2 + v_r^2 + v_\theta^2$. Thanks to Bernoulli's theorem, h remains constant along

a streamtube, thus it depends only on the streamfunction, i.e. we have $h(\psi)$. Note that all quantities in Eq. (3) are to be understood as dimensionless,

$$\kappa = \frac{RV_\theta}{R_{\mathrm{ref}}V_{\mathrm{ref}}}, \qquad h = \frac{P + \rho V^2/2}{\rho V_{\mathrm{ref}}^2}, \qquad \psi = \frac{\Psi}{R_{\mathrm{ref}}^2 V_{\mathrm{ref}}},$$

where ρ is the constant density, R_{ref} and V_{ref} are arbitrary reference radius and velocity, respectively. The partial differential equation (3) is solved for ψ within a domain in the meridian half plane (x, r), with essential or natural conditions on the domain boundary, given the generating functions $\kappa(\psi)$ and $h(\psi)$. Frewer et al. [24] argue that, under a local Lie point symmetry analysis, the Bragg–Hawthorne equation (3) is not fully equivalent to the original Euler equations since it possesses additional symmetries not being admitted by its counterpart.

We further restrict our discussion to columnar swirling flows, i.e. flows independent of the axial coordinate, in constant radius pipes. In this case, the partial differential equation (3) reduces to a nonlinear second-order differential equation,

$$\frac{\mathrm{d}^2\psi}{\mathrm{d}y^2} + \frac{\kappa(\psi)}{2y}\frac{\mathrm{d}\kappa(\psi)}{\mathrm{d}\psi} - \frac{\mathrm{d}h(\psi)}{\mathrm{d}\psi} = 0, \tag{4}$$

where $y \equiv r^2/2$ is the transformed radial coordinate. The solution of Eq. (4) is called a swirling flow state.

Eq. (4) is to be solved for $\psi(y)$ for given generating functions $\kappa(\psi)$ and $h(\psi)$, with boundary conditions,

$$\psi(a) = 0 \quad \text{and} \quad \psi(b) = \frac{q}{2}, \quad \text{with } 0 \le a \le y \le b, \tag{5}$$

where $a \equiv \dfrac{r_{\mathrm{hub}}^2}{2}$ and $b \equiv \dfrac{r_{\mathrm{shr}}^2}{2}$.

The inner boundary coordinate, a, corresponds to the hub radius r_{hub} in the turbomachinery terminology, but we can also call it central body radius. When there is no hub, a vanishes and the flow occupies the whole pipe cross-section. The outer boundary coordinate, $b > a$, corresponds to the shroud radius, r_{shr}, or the pipe wall radius. In (5), q denotes the dimensionless volumetric flow rate, further called discharge coefficient, defined as

$$q \equiv \int_a^b v_x\, 2r\mathrm{d}r = 2\left(\psi(b) - \psi(a)\right). \tag{6}$$

Although apparently simple, the boundary-value problem (4) (5) raises a series of difficulties with respect to the physical relevance of the solutions. For example, the generating functions are implicitly considered to be defined in the interval $0 \le \psi \le q/2$. Whenever $\psi < 0$ or $\psi > q/2$, a simple approach is to consider the analytical continuation of both $\kappa(\psi)$ and $h(\psi)$. However, this approach leads to reverse flow regions, where either the circulation or the total pressure should be provided from downstream. Elcrat et al. [12] consider, for example, a truncation approach to obtain physically plausible axisymmetric vortex flows with swirl and shear.

Another approach is to modify the problem definition, with the aim of keeping the solution $\psi(y)$ within the interval $[0, q/2]$. Moreover, if the streamfunction is monotonically increasing then the axial velocity is only positive, thus having a unidirectional flow. Such solutions are sought by the model proposed in this paper.

2.1. Variational formulation

Benjamin [5] introduced the equivalent variational formulation for the boundary-value problem defined by (4) and (5). A function

$\psi(y)$ that satisfies the boundary conditions (5) will be a solution of Eq. (4) if it minimizes the functional

$$\mathcal{F}(\psi; a, b) = \int_a^b \left[\frac{1}{2} \left(\frac{d\psi}{dy} \right)^2 - \frac{\kappa^2(\psi)}{4y} + h(\psi) \right] dy. \tag{7}$$

Also, Benjamin [5] coined the name "flow force" for the functional (7) since the integrand corresponds to the axial momentum, $v_x^2 + p$, once a solution is found.

2.2. The stagnant region model

Let us consider now that the cross-section available for the swirling flow extends from $y = a$ at the hub up to $y = b$ at the shroud, and the flow may occupy a smaller annular section such as

$$0 \le a \le \alpha < \beta \le b. \tag{8}$$

In the regions $a \le y \le \alpha$ and $\beta \le y \le b$ the velocity vanishes, thus we have stagnant regions. This stagnant region model is advocated for by Goldshtik and Hussain [16], as a more physical alternative to the simple analytical continuation when recirculation regions occur as solutions of the boundary-value problem (4) and (5). The examples examined in literature, e.g. [5,8,18] usually have vanishing velocity at the interface separating the stagnant region from the swirling flow. Only recently, Rusak et al. [19] consider at least a circumferentially velocity jump at the stagnant region boundary when examining possible stagnant regions in the neighborhood of the pipe wall.

In this paper, we consider that the boundary between a stagnant region and the swirling flow is generally represented by a vortex sheet with possible jumps in both velocity components. However, since this is a fluid interface, the pressure across the vortex sheet must remain continuous. Since the velocity vanishes inside the stagnant region(s), the pressure is constant, with the corresponding values at the hub and shroud, respectively,

$$p_a = h(0) - \frac{1}{2} \left(\frac{d\psi}{dy} \right)_{y=\alpha}^2 - \frac{\kappa^2(0)}{4\alpha}, \tag{9a}$$

$$p_b = h(q/2) - \frac{1}{2} \left(\frac{d\psi}{dy} \right)_{y=\beta}^2 - \frac{\kappa^2(q/2)}{4\beta}. \tag{9b}$$

The expressions (9a) for the inner stagnant region, and (9b) for the outer one, follow from Bernoulli's theorem. The expression corresponding to the static pressure (9a) has been recovered by Keller et al. [8, §2] while extending Benjamin's variational principle to variable lower end-points. Note that the expressions in Eqs. (9) do not coincide with the integrand in the functional (7) evaluated at the end-points.

2.3. Extended variational formulation

When stagnant regions are present, the functional (7) must be extended to account for the possible contributions of the stagnant pressure (9). The swirling flow is confined to the annular section $\alpha \le y \le \beta$, and in order to satisfy the differential equation (4) it must minimize the functional $\mathcal{F}(\psi; \alpha, \beta)$ with respect to the streamfunction ψ subject to the boundary conditions $\psi(\alpha) = 0$ and $\psi(\beta) = q/2$. As a result, the extended flow force functional $\mathcal{F}^\star$ will depend on the inner/outer swirling flow free boundaries α and β, respectively,

$$\mathcal{F}^\star(\alpha, \beta) = \min_\psi \mathcal{F}(\psi; \alpha, \beta) + (\alpha - a) p_a + (b - \beta) p_b. \tag{10}$$

We will further show that $\mathcal{F}^\star$ is maximized with respect to the free boundaries locations. This novel variational principle benefits from an intuitive (although heuristic) physical interpretation, as follows.

A global quantitative description of the swirling flow is provided by the swirl number, Sw, defined as the ratio between the flux of swirl momentum and the flux of axial momentum, [25, p. 2],

$$\text{Sw} \equiv \frac{\int_{r_{\text{hub}}}^{r_{\text{shr}}} v_x (r v_\theta) 2r \, dr}{r_{\text{shr}} \int_{r_{\text{hub}}}^{r_{\text{shr}}} (v_x^2 + p) 2r \, dr}. \tag{11}$$

In the above definition the pressure p is defined up to an arbitrary additive constant, and in practice it is taken as $p - p_{\text{shr}}$. However, for the present discussion this aspect is not relevant.

The numerator in (11),

$$m \equiv \int_{r_{\text{hub}}}^{r_{\text{shr}}} v_x (r v_\theta) 2r \, dr = 2 \int_0^{q/2} \kappa(\psi) \, d\psi, \tag{12}$$

is an integral constant for the swirling flow in bladeless regions, once $\kappa(\psi)$ is given. As a result, no matter the shape of the axial velocity profile, the numerator in the swirl number definition remains constant for inviscid flows.

The denominator on the other hand depends on the particular swirling flow state. As we will further show, the physically relevant swirling flow states may develop stagnant regions in order to maximize the extended flow force, $\mathcal{F}^\star$, resulting in a *minimum swirl number*,

$$\min \text{Sw} = \frac{m}{r_{\text{shr}} \max \mathcal{F}^\star}. \tag{13}$$

In conclusion, the variational principle we advocate for in this paper states that *the swirling flow state minimizes the swirl number, by maximizing the extended flow force functional.*

The examples presented and analyzed in the next sections support and validate this variational principle. However, in order to simplify the discussion, we consider in this paper only swirling flows with analytical solutions that correspond to $\min_\psi \mathcal{F}(\psi; \alpha, \beta)$. These examples correspond to zero order or first order polynomials for the generating functions $\kappa(\psi)$ and $h(\psi)$, respectively.

3. Swirling flow with constant generating functions

The simplest example of swirling flow corresponds to constant generating functions,

$$\kappa(\psi) = \kappa_0 \quad \text{and} \quad h(\psi) = h_0. \tag{14}$$

When inserting these functions in Eq. (4) the second and third terms in the left-hand side vanish. As a result, the general solution $\psi(y)$ will be a first order polynomial in y. The velocity components immediately follow as a constant axial velocity and a circumferential velocity inverse proportional with the radius,

$$v_x \equiv \frac{d\psi}{dy} = \frac{q}{2(\beta - \alpha)} \quad \text{and} \quad v_\theta = \frac{\kappa_0}{\sqrt{2y}}. \tag{15}$$

Note that the value of the constant h_0 is irrelevant. The static pressure in the possible inner/outer stagnant regions will be according to Eqs. (9),

$$p_a = h_0 - \frac{q^2}{8(\beta - \alpha)^2} - \frac{\kappa_0^2}{4\alpha}, \tag{16a}$$

$$p_b = h_0 - \frac{q^2}{8(\beta - \alpha)^2} - \frac{\kappa_0^2}{4\beta}, \tag{16b}$$

and the functional $\mathcal{F}^\star$ from (10) becomes

$$\mathcal{F}^\star(\alpha, \beta) = \frac{q^2}{8(\beta - \alpha)} \left(2 - \frac{b - a}{\beta - \alpha} \right)$$
$$- \frac{\kappa_0^2}{4} \left(\frac{b}{\beta} - \frac{a}{\alpha} + \ln \frac{\beta}{\alpha} \right). \tag{17}$$

The functional (17) has a logarithmic singularity as $\alpha \to 0$.

We can re-write the functional (17) by factoring out $q^2/(8b)$,

$$
\mathcal{F}^{\star}(\alpha, \beta; \sigma, a, b) = \frac{b}{\beta - \alpha}\left(2 - \frac{b - a}{\beta - \alpha}\right)
$$
$$
- \sigma^2\left(\frac{b}{\beta} - \frac{a}{\alpha} - \ln\frac{\alpha}{\beta}\right),
\qquad (18)
$$

where $\sigma \equiv \dfrac{\sqrt{2b}\,\kappa_0}{q} = \dfrac{\text{circumferential velocity at the wall}}{\text{pipe discharge velocity}}$.

The parameter σ quantify the swirl intensity, but it is not a swirl number.

We further examine the behavior of the functional (18) with respect to the variables α and β, with given parameters for the swirl intensity σ, and hub/shroud positions, a and b, respectively.

The partial derivative with respect to the outer swirling flow boundary β,

$$
\frac{\partial \mathcal{F}^{\star}(\alpha, \beta; \sigma, a, b)}{\partial \beta} = \frac{2b}{(\beta - \alpha)^3}[(b - a) - (\beta - \alpha)]
$$
$$
+ \frac{\sigma^2}{\beta^2}(b - \beta)
\qquad (19)
$$

is always positive thanks to the inequalities (8). As a result, the functional $\mathcal{F}^{\star}$ monotonically increases with respect to β, until it reaches its *maximum* at $\beta = b$, i.e. the flow occupies the cross-section up to the pipe wall. Consequently, in this case there is no possibility for a stagnant region to develop adjacent to the pipe wall.

Since β is clearly fixed, $\mathcal{F}^{\star}$ becomes a function of α only. In order to examine the variation with respect to α we compute

$$
\frac{\partial \mathcal{F}^{\star}(\alpha, b; \sigma, a, b)}{\partial \alpha} = (\alpha - a)\left(\frac{\sigma^2}{\alpha^2} - \frac{2b}{(b - \alpha)^3}\right).
\qquad (20)
$$

The trivial possibility for $\mathcal{F}^{\star}$ to reach an extremum with respect to α is when $\alpha = a$ and the derivative in (20) vanishes. In this case, the swirling flow occupies the whole cross-section from hub to shroud, $a \le y \le b$. The nature of this extremum can be determined by examining the second derivative with respect to α evaluated at $\alpha = a$,

$$
\left.\frac{\partial^2 \mathcal{F}^{\star}(\alpha, b; \sigma, a, b)}{\partial \alpha^2}\right|_{\alpha = a} = \frac{\sigma^2}{a^2} - \frac{2b}{(b - a)^3}.
\qquad (21)
$$

When a is smaller than the root of the algebraic equation $\sigma^2/x^2 - 2b/(b - x)^3 = 0$, then the second derivative in (21) is positive, and we have a local minimum when $\alpha = a$. However, when the hub size a is larger than the root of the above equation, the expression in (21) becomes negative, and we have a local *maximum*.

The non-trivial possibility for the first derivative in (20) to vanish is that α be the root of the algebraic equation

$$
\frac{\sigma^2}{\alpha^2} - \frac{2b}{(b - \alpha)^3} = 0.
\qquad (22)
$$

If we evaluate the second derivative with respect to α at the root of Eq. (22), say $\alpha = \alpha_0$, we get

$$
\left.\frac{\partial^2 \mathcal{F}^{\star}(\alpha, b; \sigma, a, b)}{\partial \alpha^2}\right|_{\alpha = \alpha_0} = -(\alpha_0 - a)\frac{2b(2b + \alpha_0)}{\alpha_0(b - \alpha_0)^4}.
\qquad (23)
$$

It is clear that the second derivative (23) is negative when $\alpha_0 > a$, thus $\mathcal{F}^{\star}$ reaches a *maximum* at $\alpha = \alpha_0$, with a stagnant region $a \le y \le \alpha_0$. When $a > \alpha_0$, $\mathcal{F}^{\star}$ has a maximum at $\alpha = a$, according to the previous case, and there is no stagnant region in the neighborhood of the hub.

In the particular case when $a = 0$, i.e. there is no hub, a central stagnant region is always present as long as $\sigma \ne 0$, with the radial extent given by the root of Eq. (22).
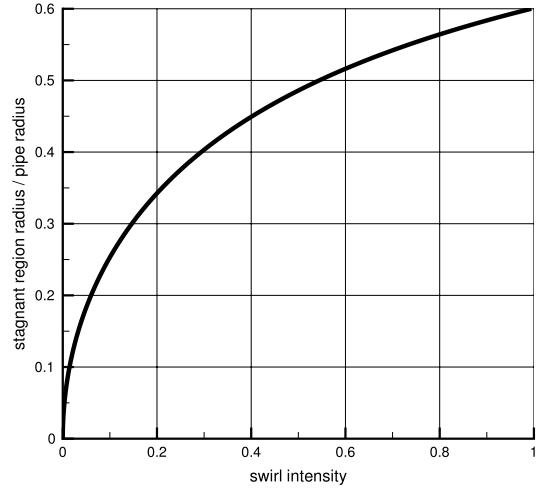

Fig. 1. The stagnant region radius, $\sqrt{2\alpha}$, Eq. (22), within a pipe of unit radius ($b = 1/2$), versus the swirl intensity parameter σ.

To summarize the above analysis, we present in Fig. 1 the ratio between the stagnant region radius $r_{\text{stag}} = \sqrt{2\alpha}$, relative to the pipe wall radius, $r_{\text{wall}} = \sqrt{2b}$, versus the swirl intensity σ, as the solution of Eq. (22).

If the hub radius, $r_{\text{hub}} = \sqrt{2a}$ is *smaller* than r_{stag} shown in Fig. 1, then a stagnant region is developed from $r_{\text{hub}} \le r \le r_{\text{stag}}$, and the flow occupies the annular section $r_{\text{stag}} \le r \le r_{\text{wall}}$. However, if the hub radius, r_{hub} is *larger* than r_{stag}, then there is no stagnant region and the flow occupies the annular section $r_{\text{hub}} \le r \le r_{\text{wall}}$. All solutions *maximize* the functional $\mathcal{F}^{\star}$ in (18).

3.1. A numerical example

Let us exemplify the above model for a swirling flow with discharge coefficient $q = 1.0$ in a pipe with radius $r_{\text{shr}} = 1.0$, i.e. $b \equiv r_{\text{shr}}^2/2 = 1/2$. The circulation value is chosen as $\kappa_0 = 0.4$. The corresponding discharge velocity, $q/(2b) = 1$ and the circumferential velocity $v_\theta = \kappa_0/r$ are shown with dashed lines in Fig. 2(a). The swirling flow configuration with stagnant region is shown with solid lines in Fig. 2(a). We notice the jump in both axial and circumferential velocity components at $r_{\text{stag}} = 0.4491433$, corresponding to the vortex sheets that separates the stagnant region from the swirling flow. However, according to the present model the static pressure remains continuous. Obviously, in order to preserve the discharge, the axial velocity in the presence of the stagnant region increases to $v_x = 1.25271$.

The stagnant region radius r_{stag} value corresponds to the maximum of the extended flow force functional, as shown in Fig. 2(b). Although the functional variation with respect to r_{stag} changes with the hub radius, the vortex sheet location remains unchanged as long as the hub radius is smaller than the corresponding stagnant region radius. We also note that the line corresponding to a hub radius $r_{\text{hub}} = 0.2$ has a local minimum at $r_{\text{stag}} = r_{\text{hub}}$.

From practical point of view, the main outcome of the present swirling flow model is the minimum hub radius for an axial turbomachine in order to prevent a stagnant region development in the annular section from hub to shroud, as shown in Fig. 1.

4. Swirling flow with first order polynomial generating functions

Let us consider a more general class of swirling flows, corresponding to generating functions as first order polynomials in the streamfunction,

$$
\kappa(\psi) = \tilde{\kappa}\psi + \kappa_0 \quad \text{and} \quad h(\psi) = \tilde{h}\psi + h_0.
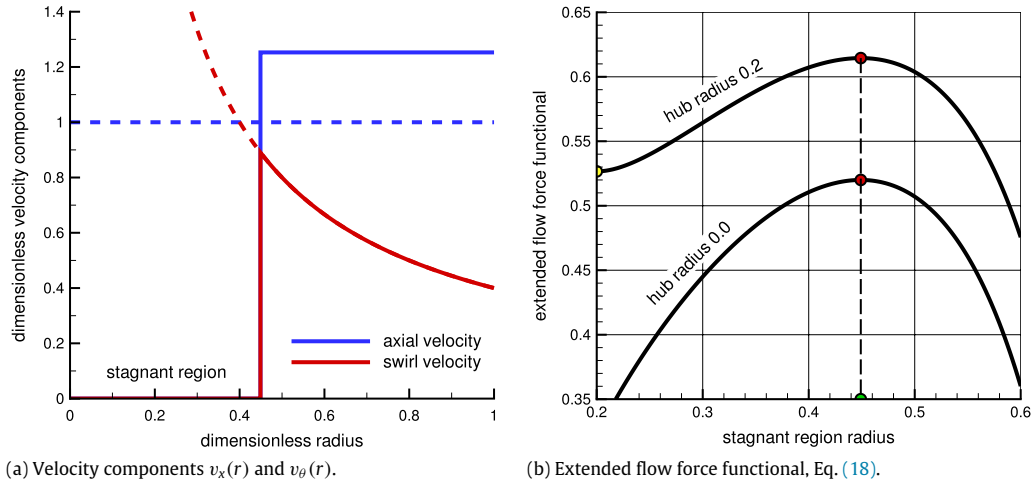\qquad (24)
$$

(a) Velocity components $v_x(r)$ and $v_\theta(r)$.

(b) Extended flow force functional, Eq. (18).

Fig. 2. Swirling flow with constant circulation $\kappa_0 = 0.4$, discharge coefficient $q = 1$ and pipe radius $r_{\text{wall}} = 1$.

The coefficients $\tilde{\kappa}$ and $\tilde{h}$ correspond to the slope of circulation and Bernoulli's functions, respectively.

When inserting the generating functions (24) into the one-dimensional Bragg–Hawthorne equation (4) we end up with a linear second order differential equation,

$$\frac{\mathrm{d}^2\psi}{\mathrm{d}y^2} + \frac{\tilde{\kappa}\,(\tilde{\kappa}\psi + \kappa_0)}{2y} - \tilde{h} = 0. \tag{25}$$

The general solution of the differential equation (25) is

$$\psi(y) = \frac{2\tilde{h}y - \tilde{\kappa}\kappa_0}{\tilde{\kappa}^2} + C_1\sqrt{2y}J_1(\tilde{\kappa}\sqrt{2y}) + C_2\sqrt{2y}Y_1(\tilde{\kappa}\sqrt{2y}). \tag{26}$$

The axial velocity profile follows immediately by differentiating (26),

$$v_x(y) \equiv \frac{\mathrm{d}\psi}{\mathrm{d}y} = \frac{2\tilde{h}}{\tilde{\kappa}^2} + C_1\tilde{\kappa}J_0(\tilde{\kappa}\sqrt{2y}) + C_2\tilde{\kappa}Y_0(\tilde{\kappa}\sqrt{2y}). \tag{27}$$

In (26) and (27), J_0 and J_1 denote the Bessel functions of the first kind, Y_0 and Y_1 are the Bessel functions of the second kind, having order zero and one, respectively.

The integration constants C_1 and C_2 are found by enforcing boundary conditions $\psi(\alpha) = 0$ and $\psi(\beta) = q/2$, resulting in a linear system of two equations,

$$C_1\sqrt{2\alpha}J_1(\tilde{\kappa}\sqrt{2\alpha}) + C_2\sqrt{2\alpha}Y_1(\tilde{\kappa}\sqrt{2\alpha}) = \frac{\kappa_0}{\tilde{\kappa}} - \frac{2\tilde{h}}{\tilde{\kappa}^2}\alpha, \tag{28a}$$

$$C_1\sqrt{2\beta}J_1(\tilde{\kappa}\sqrt{2\beta}) + C_2\sqrt{2\beta}Y_1(\tilde{\kappa}\sqrt{2\beta}) = \frac{q}{2} + \frac{\kappa_0}{\tilde{\kappa}} - \frac{2\tilde{h}}{\tilde{\kappa}^2}\beta. \tag{28b}$$

We can now insert the above analytical solution into Benjamin's flow force functional (7) and add the contributions of the stagnant regions to obtain the extended flow force functional to be maximized with respect to the inner/outer free boundaries location, α and β, respectively,

$$\mathcal{F}^\star(\alpha, \beta; a, b) = \int_\alpha^\beta \left[\frac{v_x^2}{2} - \frac{(\tilde{\kappa}\psi + \kappa_0)^2}{2y} + \tilde{h}\psi + h_0 \right] \mathrm{d}y$$
$$+ (\alpha - a)p_a + (b - \beta)p_b, \tag{29}$$

where the pressure values in the inner/outer stagnant regions are, according to Eqs. (9),

$$p_a = h_0 - \frac{v_x^2(\alpha)}{2} - \frac{\kappa_0^2}{4\alpha}, \tag{30a}$$

$$p_b = \tilde{h}\frac{q}{2} + h_0 - \frac{v_x^2(\beta)}{2} - \frac{(\tilde{\kappa}q/2 + \kappa_0)^2}{4\beta}. \tag{30b}$$

Note that by summing up the contributions of the h_0 contribution from all three terms in the right-hand side of (29) we end up with the constant $(b - a)h_0$ which is independent of either α or β values. This remark is important since if one attempts to find the extremum of Benjamin's functional (7) with respect to variable integral limits, without adding the contribution of the stagnant regions, the value of h_0 would influence the results although it should not.

4.1. Rigid-body-rotation swirling flow

A particular case within the swirling flow class defined by the generating functions of the form (24) corresponds to the flow originating from a circumferential velocity proportional to the radius, $v_\theta = \omega r$, and a constant axial velocity $v_x = q/(2b)$. The circulation function is by definition $\kappa = 2\omega y$, and Bernoulli's function follows from the radial equilibrium equation as $h = 2\omega^2 y + \text{constant}$. The constant value is irrelevant, thus without loss of generality we can take it equal to zero. The streamfunction is $\psi = (q/2)(y/b)$. Since we can arbitrarily choose the reference velocity and length, we simplify the problem definition without any loss of generality by choosing $q = 1$ and $b = 1/2$ (unit pipe radius). As a result, the generating functions for this particular swirling flow are

$$\kappa(\psi) = 2\omega\psi \quad \text{and} \quad h(\psi) = 2\omega^2\psi. \tag{31}$$

The analytical solution follows immediately by replacing $\tilde{\kappa} = 2\omega$, $\tilde{h} = 2\omega^2$, and $\kappa_0 = h_0 = 0$ in Eqs. (26)...(28), see also Batchelor [26, §7.5]

$$\psi(y) = y + C_1\sqrt{2y}J_1(2\omega\sqrt{2y}) + C_2\sqrt{2y}Y_1(2\omega\sqrt{2y}) \tag{32a}$$

$$v_x(y) = 1 + C_1 2\omega J_0(2\omega\sqrt{2y}) + C_2 2\omega Y_0(2\omega\sqrt{2y}) \tag{32b}$$

$$\begin{cases} C_1\sqrt{2\alpha}J_1(2\omega\sqrt{2\alpha}) + C_2\sqrt{2\alpha}Y_1(2\omega\sqrt{2\alpha}) = -\alpha, \\ C_1\sqrt{2\beta}J_1(2\omega\sqrt{2\beta}) + C_2\sqrt{2\beta}Y_1(2\omega\sqrt{2\beta}) = 1/2 - \beta \end{cases} \tag{32c}$$
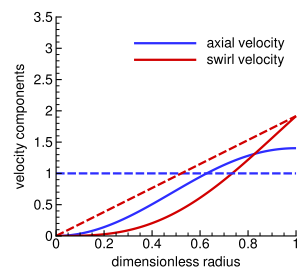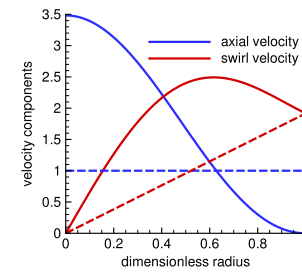$$0 \le \alpha < \beta \le 1/2.$$

A special case corresponds to the critical value of the angular velocity, $\omega_{\text{cr}} = j_{1,1}/2$, where $j_{1,1} = 3.83170597\ldots$ is the first positive zero of the Bessel function $J_1(x)$, i.e. $J_1(j_{1,1}) = 0$. There are two scenarios for obtaining non-trivial swirling flow configurations.

The first one assumes that the flow reaches the pipe wall, i.e. $\beta = 1/2$, while $\alpha \to 0$. In this case, from the boundary condition for the streamfunction at the pipe wall we have $C_2 = 0$,

Table 1
Swirling flows originating from a rigid-body rotation, for critical angular velocity $\omega = j_{1,1}/2$.

	Wake-like axial velocity	Jet-like axial velocity
Axial velocity	$v_x(r) = 1 - J_0(j_{1,1}r)$	$v_x(r) = 1 - \dfrac{J_0(j_{1,1}r)}{J_0(j_{1,1})}$
Swirl velocity	$v_\theta(r) = \dfrac{j_{1,1}}{2}r - J_1(j_{1,1}r)$	$v_\theta(r) = \dfrac{j_{1,1}}{2}r - \dfrac{J_1(j_{1,1}r)}{J_0(j_{1,1})}$
Flow force $\mathcal{F}^\star$	2.4647…	2.0328…

and the C_1 constant follows from the boundary condition at $y = \alpha > 0$,

$$C_1(\alpha) = -\frac{\alpha}{\sqrt{2\alpha}J_1(j_{1,1}\sqrt{2\alpha})} \quad \text{with} \quad \lim_{\alpha \to 0} C_1(\alpha) = -\frac{1}{j_{1,1}}. \qquad (33)$$

The axial and circumferential velocity profiles are shown in Table 1, the column for *wake-like* axial velocity. We remark that the flow occupies the whole pipe cross-section, and the axial velocity vanishes at the axis, where the circumferential velocity vanishes as well.

The second scenario considers that the flow reaches the axis, i.e. $\alpha = 0$, while $\beta \to 1/2$. In this case, from the boundary condition at the axis we have again $C_2 = 0$, and the C_1 constant follows from the boundary condition at $y = \beta < 1/2$,

$$C_1(\beta) = \frac{1/2 - \beta}{\sqrt{2\beta}J_1(j_{1,1}\sqrt{2\beta})} \quad \text{with} \quad \lim_{\beta \to 1/2} C_1(\beta) = -\frac{1}{j_{1,1}J_0(j_{1,1})}. \qquad (34)$$

The axial and circumferential velocity profiles are shown in Table 1, the column for *jet-like* axial velocity. The flow occupies the whole pipe cross-section, with vanishing axial velocity at the wall.

Let us look at the flow-force functional values for the swirling flows shown in Table 1. The original swirl with rigid-body rotation, $v_x = 1$ and $v_\theta = (j_{1,1}/2)r$, shown with dashed lines, has a value $\mathcal{F} = \mathcal{F}^\star = 2.3352\ldots$. The corresponding value for the *jet-like* swirling flow is $2.0328\ldots$, while the *wake-like* configuration has the maximum value of $2.4647\ldots$. According to the maximum flow force / minimum swirl principle advocated for in this paper, the swirling flow with wake-like axial velocity profile is the most favored one.

The swirling flow states in a pipe, originating from a rigid-body rotation swirl with constant axial velocity, i.e. with generating functions from Eq. (31), with variable angular speed ω, can be examined with respect to the stagnant region radius and the axial velocity at the boundary of the stagnant region, as shown in Fig. 3. First, one can immediately identify the particular swirling flow configuration corresponding to $\omega_{cr} = j_{1,1}/2$, where both the stagnant region radius and the corresponding axial velocity at the axis vanish, resulting in the wake-like swirling flow shown in Table 1. Second, when $\omega < \omega_{cr}$ the stagnant region radius increases with ω, from zero to a maximum value then falls to zero for $\omega = \omega_{cr}$. On the other hand, the axial velocity at the stagnant region boundary monotonically decreases as ω increases, until it vanishes at ω_{cr}. Third, when $\omega > \omega_{cr}$ the stagnant region radius increases monotonically with ω, while the axial velocity (as well as the circumferential velocity) vanishes at the boundary of the stagnant region.

Let us examine two swirling flow examples, corresponding to ω smaller and larger than ω_{cr}. Fig. 4 shows the swirling flow state
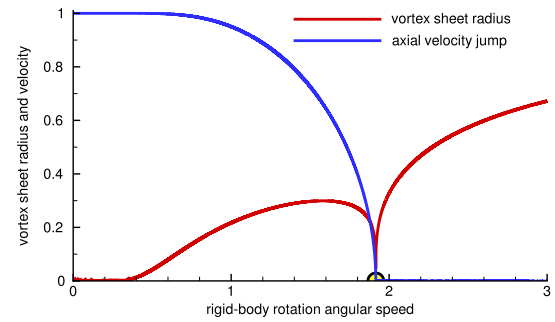

Fig. 3. The stagnant region radius and the jump in axial velocity for swirling flows originating from rigid-body rotation swirl with variable angular speed ω in Eq. (31).

for $\omega = 1.8 < \omega_{cr}$. The stagnant region radius corresponds to the maximum of the extended flow force functional, as shown in Fig. 4(b). The axial velocity, Fig. 4(a), has a jump across the vortex sheet that bounds the stagnant region, while the circumferential velocity remains continuous. The dashed lines show the velocity components for the corresponding rigid-body rotation swirl.

Fig. 5 shows the swirling flow state for $\omega = 2.0 > \omega_{cr}$. The axial and circumferential velocity profiles, Fig. 5(a), are both continuous since the velocity vanishes at the stagnant region boundary. On the other hand, the extended flow force functional versus the stagnant region radius, Fig. 5(b), displays two branches separated by the stagnant radius value where the determinant of the system (32c) vanishes, $r^\star_{stag} = 0.12556\ldots$. The left branch has a maximum at vanishing stagnation, corresponding to the basic swirling flow with rigid-body rotation shown with dashed lines in Fig. 5(a). The right branch has a maximum at the stagnant region radius that corresponds to the swirling flow state shown with solid lines in Fig. 5(a).

5. Assessment against experimental data

We further examine the ability of the simple swirling flow model presented in Section 4 to reproduce the main features of real swirling flows measured downstream the runner of a Francis turbine model at several operating regimes, [22,23].

For completeness we present the experimental setup in Fig. 6, where the cross-section through a model Francis turbine shows the survey section downstream the runner, in the discharge cone, on which both axial and circumferential velocity profiles are measured using a two-component probe Laser Doppler Anemometer. The main characteristics of the LDA system are given in [22, §2], and uncertainties of the velocity measurements are estimated to be 2% of the measured value. The dimensionless
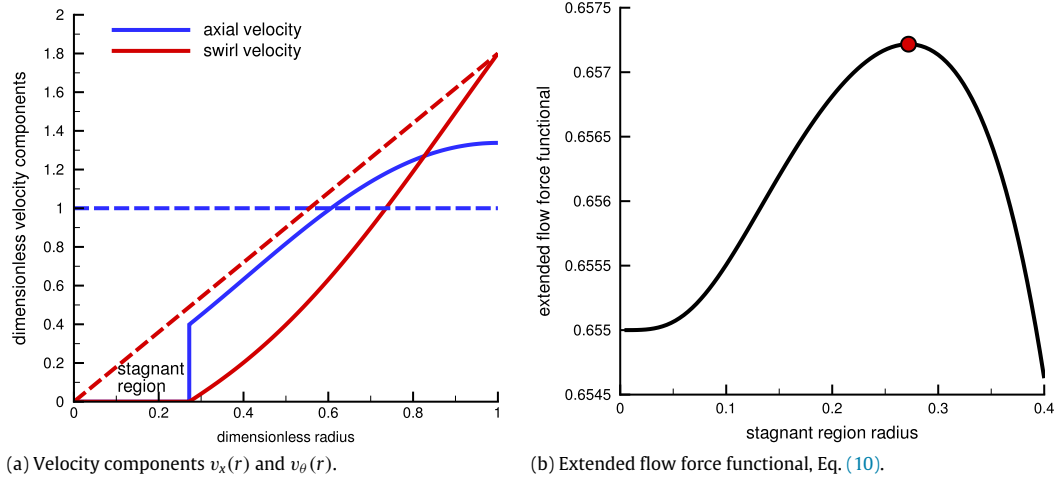
(a) Velocity components $v_x(r)$ and $v_\theta(r)$.

(b) Extended flow force functional, Eq. (10).

Fig. 4. Swirling flow originating from a rigid-body rotation swirl, $\omega = 1.8$, with constant axial velocity.

(a) Velocity components $v_x(r)$ and $v_\theta(r)$.
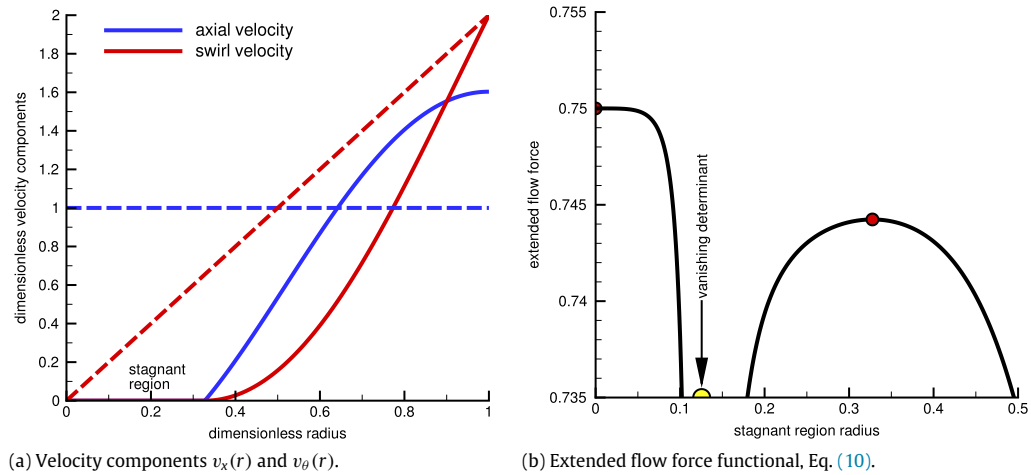
(b) Extended flow force functional, Eq. (10).

Fig. 5. Swirling flow originating from a rigid-body rotation swirl, $\omega = 2.0$, with constant axial velocity.

radius in the survey section runs up to the wall value of $R_w/R_{ref} = 1.063$. The velocity components are made dimensionless with respect to the runner outlet transport velocity (runner angular speed × runner outlet radius), as customary for turbomachines.

The discharge coefficient, q, and flux of circulation function m, are shown in Table 2 for seven operating points where experimental data are available for axial and circumferential velocity profiles, [23, Tab. 1]. The operating points are labeled by indicating the fraction of the best efficiency discharge Q_{BEP}, i.e. the turbine volumetric flow rate where the overall efficiency reaches a maximum. Such labeling practice gives a clear correlation between the range of q − values and the turbine operating regimes.

The discharge coefficient q is accounted for through the boundary conditions for the streamfunction. On the other hand, m can be incorporated into the model via the generating function $\kappa(\psi)$,

$$m = 2 \int_0^{q/2} (\tilde{\kappa}\psi + \kappa_0) \, d\psi \Rightarrow \kappa_0 = \frac{m}{q} - \tilde{\kappa}\frac{q}{4}. \quad (35)$$

As a result, the generating functions (24) can be rewritten as

$$\kappa(\psi) = \tilde{\kappa}\left(\psi - \frac{q}{4}\right) + \frac{m}{q}, \quad (36a)$$

$$h(\psi) = \tilde{h}\psi. \quad (36b)$$

The constant h_0 has been considered zero, without any loss of generality. The two slope coefficients in Eqs. (36), $\tilde{\kappa}$ and $\tilde{h}$,

Table 2
Integral quantities for swirling flows downstream a Francis turbine runner.

Operating point	q, Eq. (6)	m, Eq. (12)
$0.714\,Q_{BEP}$	0.26428	0.048341
$0.919\,Q_{BEP}$	0.34015	0.036829
$0.974\,Q_{BEP}$	0.36066	0.030264
Q_{BEP}	0.37014	0.028227
$1.025\,Q_{BEP}$	0.37950	0.025154
$1.050\,Q_{BEP}$	0.38881	0.021944
$1.107\,Q_{BEP}$	0.40976	0.013239

respectively, are found through a least squares fit of experimental data. More precisely, using the `RNLIN` subroutine from the IMSL library, we simultaneously fit the data for axial and circumferential velocity components using the analytical expression (27) for v_x and $v_\theta = \kappa(\psi)/r$, with ψ from (26).

As shown in Table 3, both $\tilde{\kappa}$ and $\tilde{h}$ decrease as the turbine discharge increases. Moreover, $\tilde{h}$ is positive at part load, i.e. there is a deficit of specific energy near the runner hub, and $\tilde{h}$ is negative at full load, i.e. there is an excess of specific energy at the hub. This is consistent with the turbine operation. As expected, near the best efficiency point the specific energy is practically constant from hub-to-shroud (vanishing slope), as it is intended in the runner design methodology.

Figures 7...13 show the comparison of quasi-analytical model against the experimental data. The stagnant region radius is obtained by maximizing $\mathcal{F}^\star$, thus it is not a fit parameter.
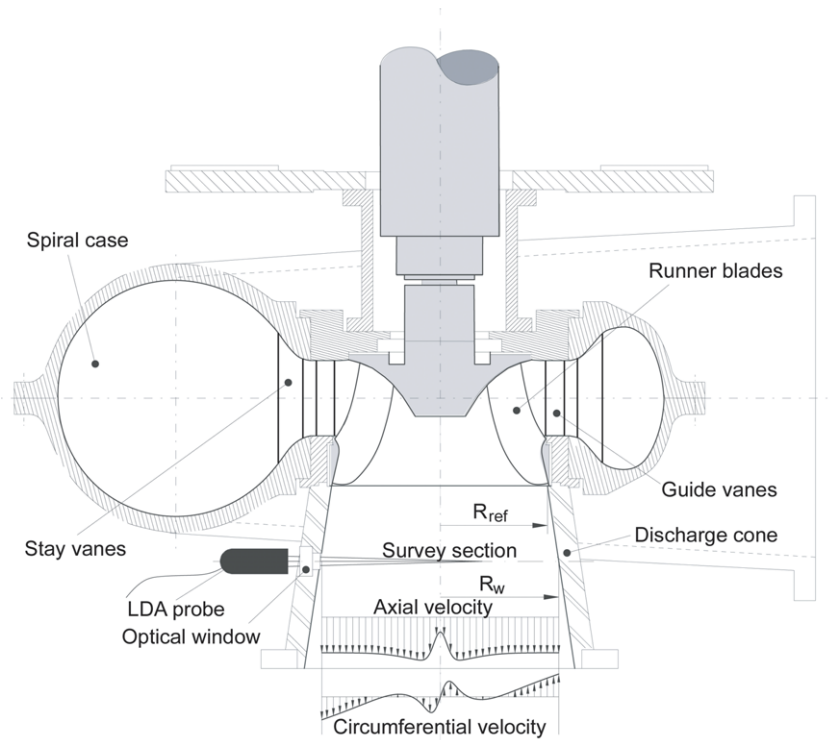
Fig. 6. Experimental setup for a model Francis turbine for swirling flow measurements downstream the runner, in the discharge cone.
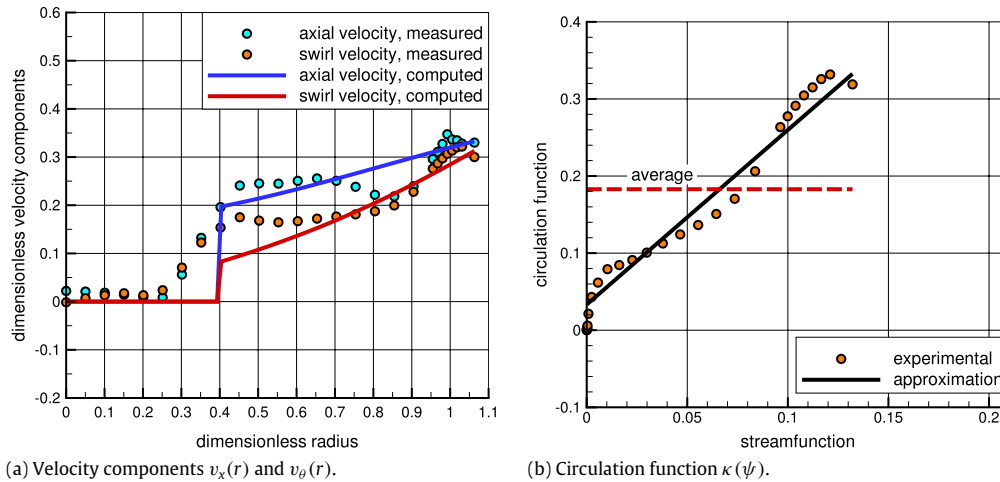

(a) Velocity components $v_x(r)$ and $v_\theta(r)$.

(b) Circulation function $\kappa(\psi)$.

Fig. 7. Swirling flow at the operating point with discharge 71.4% the best efficiency value.

Table 3

Fit parameters $\tilde{\kappa}$ and $\tilde{h}$.

Operating point	$\tilde{\kappa}$, Eq. (36a)	$\tilde{h}$, Eq. (36b)
$0.714\,Q_{BEP}$	2.265376	0.8529927
$0.919\,Q_{BEP}$	1.248654	0.2669378
$0.974\,Q_{BEP}$	0.9127730	0.1045096
Q_{BEP}	0.8212194	0.02599025
$1.025\,Q_{BEP}$	0.8046825	−0.04884591
$1.050\,Q_{BEP}$	0.7035756	−0.1229106
$1.107\,Q_{BEP}$	0.5387202	−0.2272735

Fig. 7 corresponds to a part load operating point, quite far from the best efficiency regime. In this case, there is a large quasi-stagnant central region, Fig. 7, bounded by a vortex sheet [27]. However, this vortex sheet is unstable and it evolves into a precessing helical vortex, Ciocan et al. [28]. As a result, the velocity profiles from Fig. 7(a) correspond to the circumferentially averaged flow field. Within our model the flow is considered inviscid and axisymmetrical, thus the vortex sheet is represented by a jump in both axial and circumferential velocity components. Fig. 7(b) shows the comparison between the circulation function $\kappa = rv_\theta$ computed from experimental data and the first order polynomial approximation Eq. (36a). The flux-weighted average m/q value is also shown with a dashed line. Note that the solid line in Fig. 7(b) is not a least squares fit of data for κ, as the slope coefficient $\tilde{\kappa}$ is obtained by fitting the original velocity data from Fig. 7(a).

The remaining operating points are clustered within ±10% the best efficiency discharge. Although the analytical model from Section 4 is a rather crude approximation of the real swirling flow downstream a hydraulic turbine runner, one can see that it captures correctly the main flow features. For example, the stagnant radius decreases as the operating point approaches the best efficiency regime, either by increasing or by decreasing the
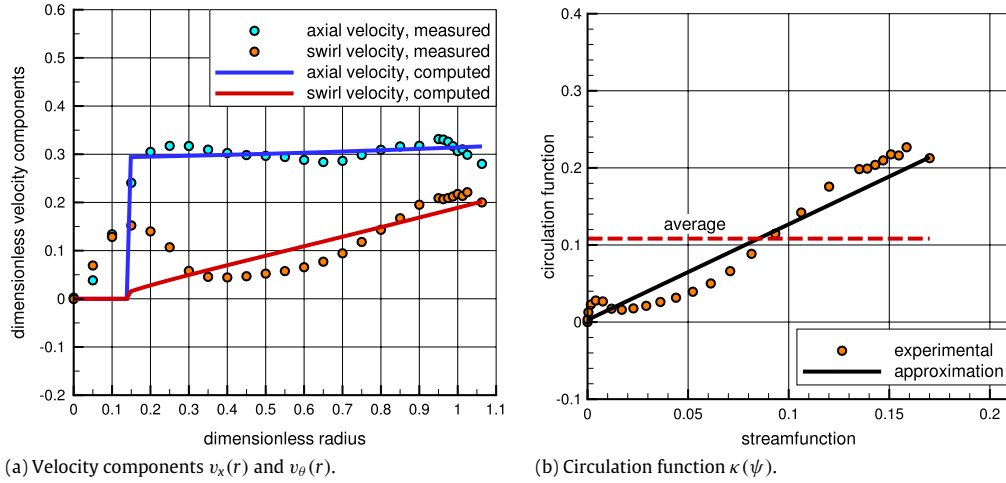
(a) Velocity components $v_x(r)$ and $v_\theta(r)$.

(b) Circulation function $\kappa(\psi)$.

Fig. 8. Swirling flow at the operating point with discharge 91.9% the best efficiency value.

(a) Velocity components $v_x(r)$ and $v_\theta(r)$.

(b) Circulation function $\kappa(\psi)$.
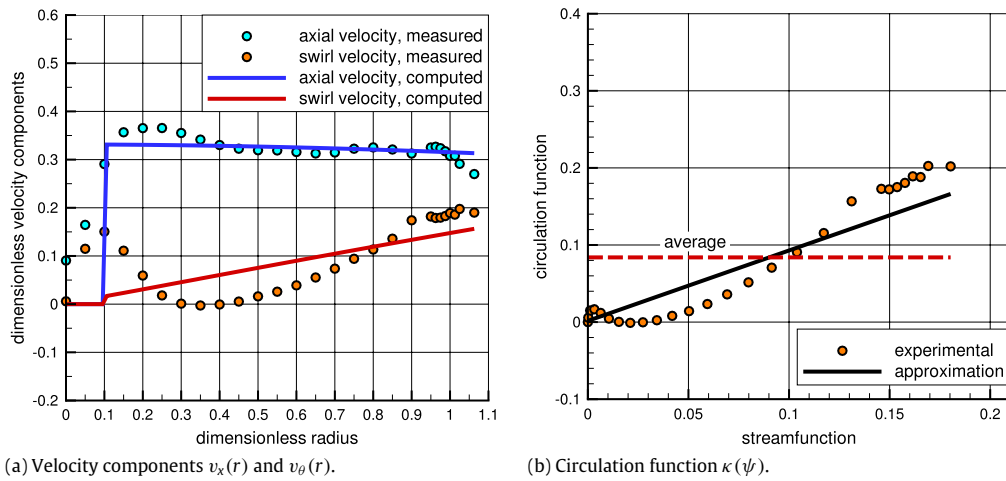
Fig. 9. Swirling flow at the operating point with discharge 97.4% the best efficiency value.

(a) Velocity components $v_x(r)$ and $v_\theta(r)$.

(b) Circulation function $\kappa(\psi)$.
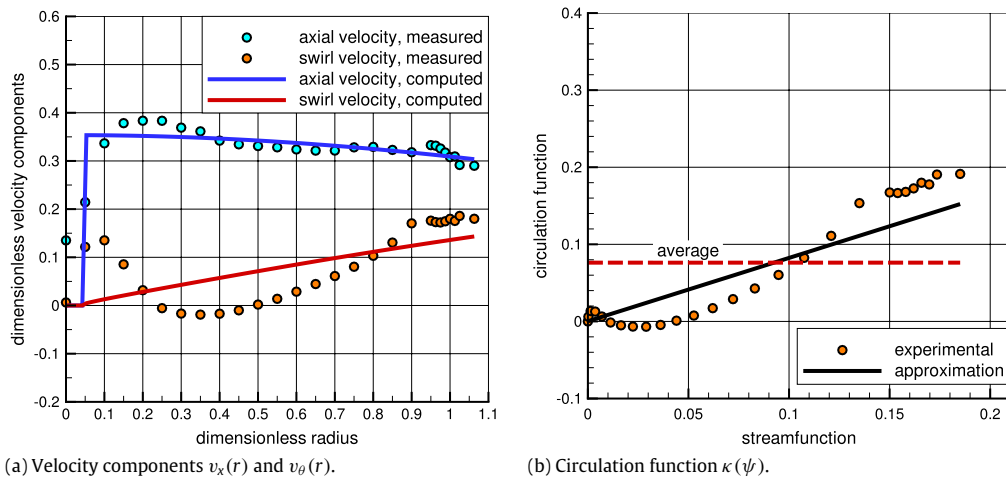
Fig. 10. Swirling flow at the best efficiency operating point.

discharge. In these cases the central stagnant region can be seen as the equivalent of the displacement thickness in the boundary layer theory, but here it can be associated with the runner hub wake.

At full load operating points, e.g. Fig. 13, the first order polynomial for $\kappa(\psi)$ becomes a rather poor approximation of the experimental data, Fig. 13(b), thus we cannot expect a good approximation of the circumferential velocity profile in Fig. 13(a).

6. Conclusions

The paper introduces a variational principle for computing swirling flow states in a pipe. Benjamin's flow force functional is extended to account for possible stagnant regions developed either in the neighborhood of the axis (or central body) or near the pipe wall.
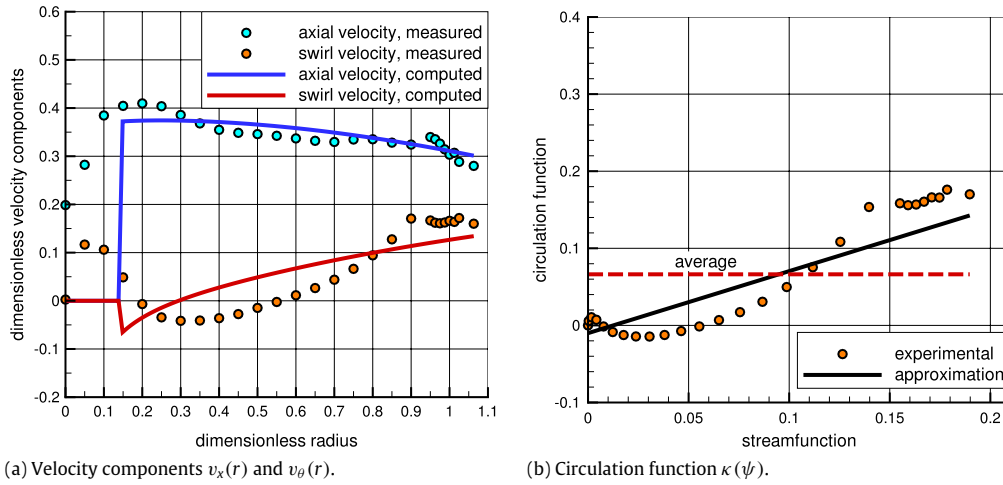
(a) Velocity components $v_x(r)$ and $v_\theta(r)$.

(b) Circulation function $\kappa(\psi)$.

Fig. 11. Swirling flow at the operating point with discharge 102.5% the best efficiency value.

(a) Velocity components $v_x(r)$ and $v_\theta(r)$.

(b) Circulation function $\kappa(\psi)$.
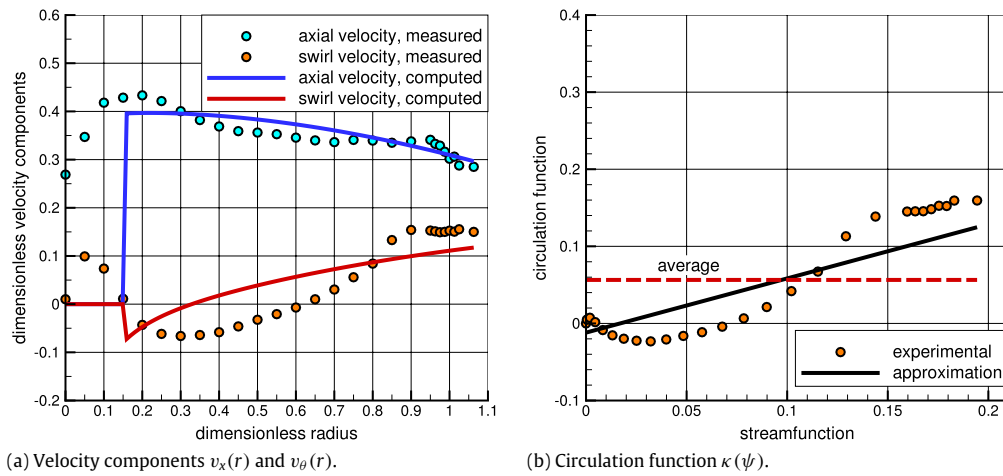
Fig. 12. Swirling flow at the operating point with discharge 105.0% the best efficiency value.

(a) Velocity components $v_x(r)$ and $v_\theta(r)$.

(b) Circulation function $\kappa(\psi)$.
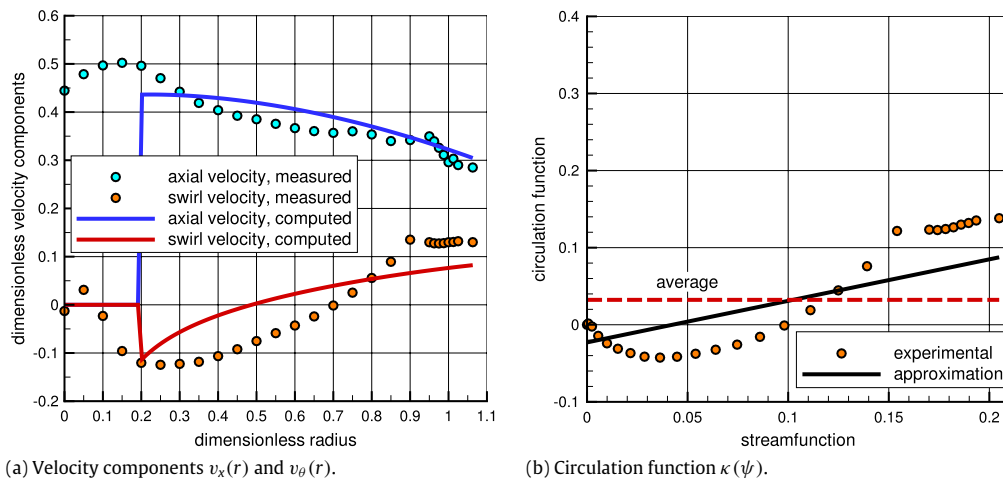
Fig. 13. Swirling flow at the operating point with discharge 110.7% the best efficiency value.

The stagnant regions are bounded by vortex sheets with possible jumps in axial and/or circumferential velocity components, while the pressure remains continuous across the vortex sheet. These vortex sheets are free boundaries, and their location is found by maximizing the extended flow force functional. From physical point of view, this variational principle corresponds to the minimum swirl number value.

The main advantage of using this variational principle for computing swirling flow states is that there is no need for specifying additional conditions, such as vanishing velocity, in order to determine the stagnant region boundary location.

Through a set of numerical examples we show that the variational principle introduced in this paper can automatically captures a variety of swirling flow configurations, such as:

- flows without stagnant regions, that occupy the whole available cross section;
- flows with stagnant region, without jump in velocity components;
- flows with stagnant region with jump in one velocity component;
- flows with stagnant region bounded by a vortex sheet with jumps in both axial and circumferential velocity components.

The examples included in the paper correspond to either zero order or first order polynomials for the circulation and Bernoulli's functions, where analytical solutions are available. It is shown that by maximizing the extended flow force functional (minimizing the swirl number), one obtains physically relevant swirling flow configurations. Moreover, it is shown that the proposed model can successfully capture the main features of real swirling flows, by a two-parameter fit of experimental data available for axial and circumferential velocity components.

Acknowledgments

References

[1] M. Escudier, Confined vortices in flow machinery, Annu. Rev. Fluid Mech. 19 (1987) 27–52. http://dx.doi.org/10.1146/annurev.fl.19.010187.000331.

[2] S.L. Bragg, W.R. Hawthorne, Some exact solutions of the flow through annular cascade actuator discs, J. Aeronaut. Sci. 17 (4) (1950) 243–249. http://dx.doi.org/10.2514/8.1597.

[3] R.R. Long, Steady motion around a symmetrical obstacle moving along the axis a rotating liquid, J. Meteorol. 10 (3) (1953) 197–203. http://dx.doi.org/10.1175/1520-0469(1953)010<0197:SMAASO>2.0.CO;2.

[4] H.B. Squire, Rotating fluids, in: G.K. Batchelor, R.M. Davies (Eds.), Surveys in Mechanics, Cambridge University Press, 1956, p. 139. http://dx.doi.org/10.1002/zamm.19570370314.

[5] T.B. Benjamin, Theory of the vortex breakdown phenomenon, J. Fluid Mech. 14 (4) (1962) 593–629. http://dx.doi.org/10.1017/S0022112062001482.

[6] M.G. Hall, Vortex breakdown, Annu. Rev. Fluid Mech. 4 (1972) 195–218. http://dx.doi.org/10.1146/annurev.fl.04.010172.001211.

[7] J.D. Buntine, P.G. Saffman, Inviscid swirling flows and vortex breakdown, Proc. R. Soc. A 449 (1935) (1995) 139–153. http://dx.doi.org/10.1098/rspa.1995.0036.

[8] J.J. Keller, W. Egli, J. Exley, Force- and loss-free transitions between flow states, Z. Angew. Math. Phys. (ZAMP) 36 (6) (1985) 854–889. http://dx.doi.org/10.1007/BF00944899.

[9] C.Y. Huang, G.S. Dulikravich, Stream function and stream-function-coordinate (SFC) formulation for inviscid flow field calculations, Comput. Methods Appl. Mech. Engrg. 59 (2) (1986) 155–177. http://dx.doi.org/10.1016/0045-7825(86)90100-3.

[10] J.J. Keller, W. Egli, R. Althaus, Vortex breakdown as a fundamental element of vortex dynamics, Z. Angew. Math. Phys. (ZAMP) 39 (3) (1988) 404–440. http://dx.doi.org/10.1007/BF00945061.

[11] J.J. Keller, On the interpretation of vortex breakdown, Phys. Fluids 7 (7) (1995) 1695–1702. http://dx.doi.org/10.1063/1.868757.

[12] A.R. Elcrat, B. Fornberg, K.G. Miller, Steady axisymmetric vortex flows with swirl and shear, J. Fluid Mech. 613 (2008) 395–410. http://dx.doi.org/10.1017/S002211200800342X.

[13] R. Fernandez-Feria, J. Ortega-Casanova, Inviscid vortex breakdown models in pipes, Z. Angew. Math. Phys. (ZAMP) 50 (5) (1999) 698–730. http://dx.doi.org/10.1007/s000330050175.

[14] J. Ortega-Casanova, R. Fernandez-Feria, Inviscid evolution of incompressible swirling flow in pipes: The dependence of the flow structure upon the inlet velocity field, Eur. J. Mech. B Fluids 18 (6) (1999) 1067–1084. http://dx.doi.org/10.1016/S0997-7546(99)00141-7.

[15] M. Goldshtik, F. Hussain, The nature of inviscid vortex breakdown, Phys. Fluids 9 (1997) 263–265. http://dx.doi.org/10.1063/1.869146.

[16] M. Goldshtik, F. Hussain, Analysis of inviscid vortex breakdown in a semi-infinite pipe, Fluid Dynam. Res. 23 (1998) 189–234. http://dx.doi.org/10.1016/S0169-5983(98)00016-1.

[17] S. Wang, Z. Rusak, The dynamics of a swirling flow in a pipe and transition to axisymmetric vortex breakdown, J. Fluid Mech. 340 (1997) 177–223. http://dx.doi.org/10.1017/S0022112097005272.

[18] Z. Rusak, S. Wang, C.H. Whiting, The evolution of a perturbed vortex in a pipe to axisymmetric vortex breakdown, J. Fluid Mech. 366 (1998) 211–237. http://dx.doi.org/10.1017/S0022112098001396.

[19] Z. Rusak, N.R. Bourquard, S. Wang, Vortex breakdown in swirling flows in diverging or contracting pipes. AIAA Paper No. 2013-1010; 2013. http://dx.doi.org/10.2514/6.2013-1010.

[20] V. Shtern, F. Hussain, M. Herrada, New features of swirling jets, Phys. Fluids 12 (11) (2000) 2868–2877. http://dx.doi.org/10.1063/1.1313547.

[21] S.V. Alekseenko, P.A. Kuibin, V.L. Okulov, S.I. Shtork, Helical vortices in swirl flow, J. Fluid Mech. 382 (1999) 195–243. http://dx.doi.org/10.1017/S0022112098003772.

[22] R. Susan-Resiga, G.D. Ciocan, I. Anton, F. Avellan, Analysis of the swirling flow downstream a francis turbine runner, J. Fluids Eng.-Trans. ASME 128 (1) (2006) 177–189. http://dx.doi.org/10.1115/1.2137341.

[23] R.F. Susan-Resiga, S. Muntean, F. Avellan, I. Anton, Mathematical modelling of swirling flow in hydraulic turbines for the full operating range, Appl. Math. Model. 35 (10) (2011) 4759–4773. http://dx.doi.org/10.1016/j.apm.2011.03.052.

[24] M. Frewer, M. Oberlack, S. Guenter, Symmetry investigations of the incompressible stationary axisymmetric Euler equations with swirl, Fluid Dynam. Res. 39 (8) (2007) 647–664. http://dx.doi.org/10.1016/j.fluiddyn.2007.02.004.

[25] A.K. Gupta, D.G. Lilley, N. Syred, Swirl Flows. Tunbridge Wells, Abacus Press, England, 1984.

[26] G. Batchelor, An Introduction to Fluid Dynamics, Cambridge University Press, ISBN: 0521663962, 1967.

[27] R. Susan-Resiga, S. Muntean, P. Stein, F. Avellan, Axisymmetric swirling flow simulation of the draft tube vortex in francis turbines at partial discharge, Int. J. Fluid Mach. Syst. 2 (4) (2009) 295–302. URL: http://jlc.jst.go.jp/JST.JSTAGE/ijfms/2.295.

[28] G.D. Ciocan, M.S. Iliescu, T.C. Vu, B. Nennemann, F. Avellan, Experimental study and numerical simulation of the FLINDT draft tube rotating vortex, J. Fluids Eng.-Trans. ASME 129 (2) (2007) 146–158. http://dx.doi.org/10.1115/1.2409332.